ALMA MATER STUDIORUM
UNIVERSITÀ DI BOLOGNA

DEPARTMENT OF INDUSTRIAL CHEMISTRY "TOSO MONTANARI"

SECOND CYCLE DEGREE IN

LOW CARBON TECHNOLOGIES AND SUSTAINABLE CHEMISTRY

CLASSE LM-71 – INDUSTRIAL CHEMISTRY

DEVELOPMENT AND EVALUATION OF PGM-FREE ANODIC ELECTRODES FOR THE OXYGEN EVOLUTION REACTION IN AEM ELECTROLYZERS

Supervisor

Dr. Andrea Fasolini

Co-Supervisor

Dr. Nicholas Loi

Candidate

Micaela Calzone

III Session January 2025

Academic Year 2023/2024

Abstract

The transition to renewable energy must address its intermittency. Green hydrogen, produced CO_2-free through renewable-powered water electrolysis, offers a solution as an energy carrier.

This thesis investigated the emerging technology of Anion Exchange Membrane Water Electrolyzer (AEMWE), with a focus on PGM-free anodic electrocatalysts for the Oxygen Evolution Reaction (OER) based on different catalytic compositions: $NiFe_2O_4$, NiO, Co_3O_4. The research included the formulation and optimization of anodic catalytic inks, the deposition of the catalytic layer onto nickel felts using the Catalyst Coated Substrate (CCS) methodology, the execution of preliminary thermal treatments on all the electrodes at 120°C, as well as additional treatments at 350°C on $NiFe_2O_4$ to evaluate their effects on catalytic properties. Morphological and structural properties were investigated through SEM/EDS and XRD analyses to establish correlations with performance and stability, which were evaluated through electrochemical tests.

The thermally treated $NiFe_2O_4$ samples were analysed in terms of morphology, structure, performance and durability and the results were compared with those of untreated samples. It appeared that although the higher-temperature treatment effectively reduced the average particle size and eliminated impurities, it also led to a decline in mechanical integrity, being unsuitable for applications requiring long-term durability, such as electrolyzers. In contrast, the lower-temperature treatment preserved the structural integrity while moderately decreasing the average particle size, offering a compromise between catalytic activity and durability.

Finally, from a comparative evaluation, among the analysed catalysts, $NiFe_2O_4$ emerges as the most suitable candidate for long-term industrial applications, combining good catalytic activity and excellent stability. While NiO and Co_3O_4 demonstrated superior initial performance, their stability is limited compared to $NiFe_2O_4$.

Table of contents

1. Thesis Objective

This thesis investigates the emerging technology of Anion Exchange Membrane Water Electrolyzer (AEMWE), focusing on the optimization of formulation and performance in terms of catalytic activity and durability of non-noble metal-based anodic catalysts for the Oxygen Evolution Reaction (OER).

A key aspect of this research addresses the significant kinetic challenges associated with OER, by examining and comparing commercially available anodic electrocatalysts, specifically nickel oxide (NiO), cobalt oxide (Co_3O_4), nickel iron oxide ($NiFe_2O_4$).

The choice to focus on noble-metal-free catalysts is driven by the goal of enhancing the sustainability and cost-effectiveness of water electrolyzers, reducing reliance on noble metals and facilitating the large-scale production of green hydrogen.

A concise overview of Alkaline Water Electrolyzers (AWE) and Proton Exchange Membrane Water Electrolyzers (PEMWE) is included to provide context and highlight characteristics and advantages of AEMWE.

This research was conducted in collaboration with Arco Technologies S.r.l. and mainly involved:

- Formulation and optimization of anodic catalytic inks,
- Deposition of the catalytic layer onto electrodes, following Catalyst Coated Substrate (CCS) methodology,
- Execution of preliminary thermal treatments on electrodes and pretreatments on the membrane,
- Performing electrochemical tests on NiO, Co_3O_4, $NiFe_2O_4$ electrocatalysts to evaluate their performances and stability,
- Conducting morphological analyses, including Scanning Electron Microscopy (SEM) and X-ray Diffraction (XRD), to correlate structural characteristics with catalysts performances.

2. Introduction

2.1. Climate Change and Renewable Energy Forms

One of the main challenges the world is facing in recent years is climate change, specifically global warming, that has harmful effects on ecosystems and human society. [1] The main cause of climate change is the emission of Greenhouse Gasses (GHGs) in the atmosphere: they generate a rise in global temperatures. Most human activities contribute to raise the level of greenhouse gases and among all areas of human impact, the primary GHG emitted is carbon dioxide (CO_2), accounting for approximately 80% of the total emissions, however it is not the most dangerous in terms of global warming potential. [2]

In figure 1 GHGs emissions by substance are showed, while in figure 2, emissions are categorized by sectors, providing an overview of how different areas of industry contribute to overall emissions. [2]

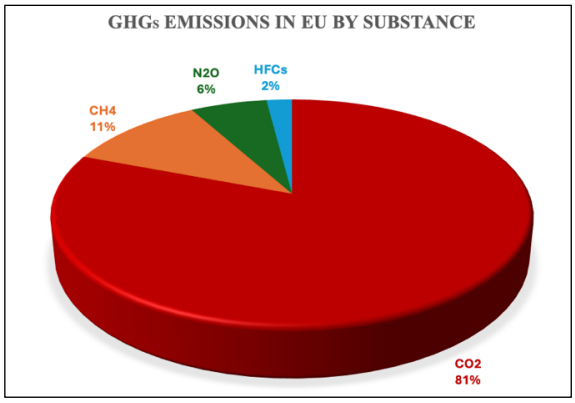

Figure 1: *GHGs emissions distribution in European Union by pollutant in 2019. Percentages are rounded and emissions related to soil usage and silviculture are excluded. Data are provided by the European Environment Agency (EEA). [2]*

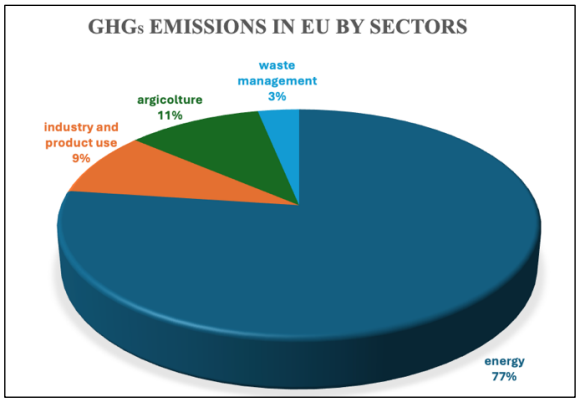

Figure 2: *Distribution of greenhouse gas (GHG) emissions in the European Union by sectors in 2019. Data are provided by the European Environment Agency (EEA). [2]*

As shown in graph 2, the energy sector accounts for most of the total emissions, specifically the 77%, one third of which is related to the transport sector. Other relevant emissions sources are industrial processes and product use, responsible for a 9.10%; and agriculture, contributing to a 10.55%. Finally, a 3.32% of emissions is related to waste management. [2] These data indicate the critical impact of energy production, distribution and utilization on global emissions levels. Indeed, the rising energy demand is largely met by burning fossil fuels: their

combustion generates energy, but also leads to massive GHGs emissions, specifically CO_2. [2,3]

A decarbonization of the energy sector is crucial to address climate challenges, transitioning to renewable energy sources, such as solar, wind, hydroelectric power, becomes crucial to promote a sustainable energy system and mitigate anthropogenic GHGs emissions. [3]

However, one of the key issues related to renewable energy sources is their intermittent nature. Differently from conventional energy sources, such as fossil fuels, alternative energies do not provide a constant supply during the day and across different seasons. This variability generates a mismatch between energy demand and availability, creating a need for effective energy storage strategies. To ensure a constant energy supply, it is essential to store large quantities of energy, and it can be done exploiting chemical compounds such as hydrogen, methane, methanol, dimethyl ether (DME), that acts as energy carriers that can store excess energy during peak production periods and release it when sustainable energy sources are not available. [3]

Among the chemical energy carriers, hydrogen holds important potential as energy vector, its valuable properties are analysed in paragraph 2.2, together with applications and production methods.

2.2. Hydrogen: Properties, Applications, Production

Hydrogen (H_2), gaseous under atmospheric conditions, is the lightest and smallest element existing. Moreover, it is colourless, odourless, non-toxic, and non-corrosive; despite this, it could make more fragile some materials, e.g. some metals. [4]

The auto-ignition temperature of hydrogen is comparable to that of natural gas and significantly higher respect to that of gasoline vapor, making both hydrogen and natural gas safer respect to spontaneous ignition. However, safety concerns arise due to the flammability range of H_2, wider respect to other fuels, ranging from 4 % and 75% in air. In particular, the optimal combustion condition is when hydrogen constitutes the 29% of the air mixture, the energy required to initiate the reaction is lower respect to other fuels and even a small spark starts the flame. At lower concentrations of hydrogen, the energy requirement is similar to that of other fuels. [4]

H_2 is a molecule of extreme importance across several sectors, the reason why its demand has increased over years. Specifically, it is widely used in the chemical industry, to serve as a

feedstock for several processes, including methanol and ammonia production, the latter exploited in the agricultural field to produce fertilizers. Moreover, hydrogen is employed in the metal industry, and in the energetic field, since it holds a great potential as an alternative fuel to replace fossil-based ones. [5]

Its high demand depends also on its physical characteristics. Compared to other fuels, hydrogen presents the highest gravimetric standard heat of formation, meaning that its energy content by weight is the highest, providing more energy per unit weight. For example, H_2 supplies 118 MJ per kilogram at 298 K, compared to the 44 MJ for gasoline. [6] However, the high energy content by weight does not correspond to a high energy content by volume, posing a challenge for the storage. Indeed, the volumetric energy density of hydrogen is 8 MJ per litre, four times lower that the 32 MJ per litre of gasoline. [5]

Despite its abundance, H_2 is not present in a free form on the Earth, but it is found in form of hydrocarbons and water. [6] This implies that it must be extracted, which can be achieved through different methods, and direct and indirect emissions generated during the processes vary a lot depending on the production method used. The variability depends on factors such as the technology, the efficiency of carbon capture and storage, the types of input fuels and the energy source. [7] Predictably, the techniques to extract hydrogen from organic compounds, mainly represented by fossil fuels, are greenhouse gasses emitting and rely on a finite, non-renewable resource. [6] Instead, producing hydrogen from water electrolysis can provide a widely abundant and sustainable alternative source. [6] However, to avoid GHG emissions, a sustainable energy sources should be harnessed to obtain the energy needed to split water molecules. [8]

Based on previous considerations, H_2 can be classified with different "colours", to indicate its carbon emissions, depending on the source of energy and material used in the production: [9]

- Black hydrogen is obtained by coal gasification, it is considered the most environmental damaging and emitting technology.

- Grey hydrogen is produced from fossil fuels refinement, mainly by methane steam reforming, a catalytic reaction that uses high pressure to decompose methane into H_2, CO, CO_2. Since this process does not foresee any technology of carbon capture and storage, it results in CO_2 emitted in the atmosphere.

- Blue hydrogen is still produced by methane steam reforming, but with systems that capture and store the CO_2 underground, resulting in a cleaner version of the previous process. However, despite the improvement, the process still rely on a finite fossil source and some CO_2 cannot be captured and will still be released.
- Turquoise hydrogen foresees the generation of hydrogen by methane pyrolysis, that will produce solid carbon, instead of volatile CO_2.
- Green hydrogen: this hydrogen is produced without any emission of CO_2, due to the absence of carbonaceous compounds in the process, resulting in the cleanest H_2 form. It is derived from water electrolysis, with renewable source of energy used to power the electrolyzers.

The graph below shows hydrogen production in 2020, 2021, 2022, measured in million tons (Mt) of H_2 and categorized by different production routes.

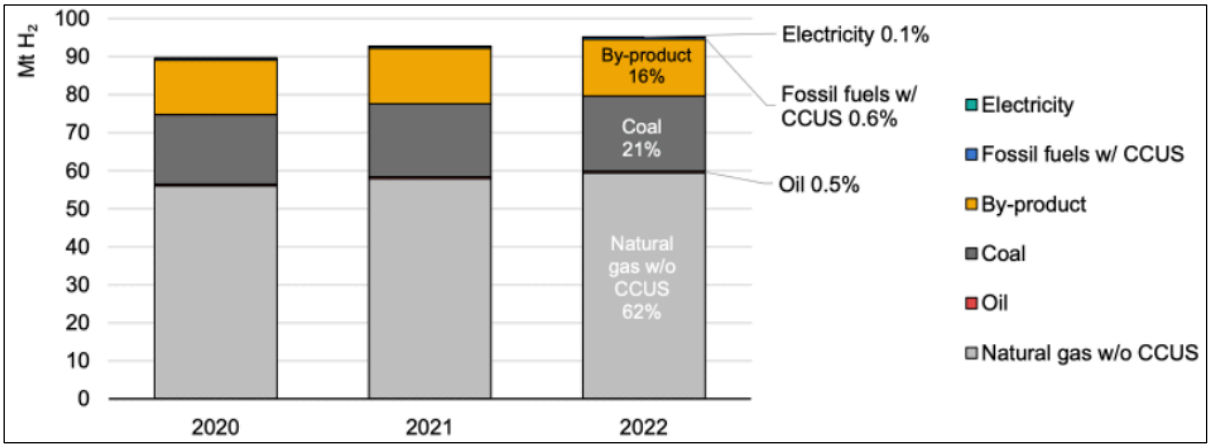

***Figure 3**: Hydrogen production, measured in million tons, by source in years 2021, 2021, 2022. [7]*

The production of hydrogen increased slightly over the three years, reaching 95Mt in 2022 and fossil fuels use prevailed. Natural gas without carbon capture, utilization, and storage (indicated as "CCUS") was the predominant source for all the three years, accounting for 62% in 2022. As the CO_2 generated in these processes was emitted in the atmosphere, this value can be addressed as grey hydrogen production. This was followed by black hydrogen: coal gasification accounted for 21%. Another 16% was associated to by-product of other processes in refineries and petrochemical industry. Minor contributions were oil, that represented a 0.5%, and fossil fuels with CCUS, responsible for 0.6% of production. Notably, only the 0.7% of the hydrogen produced in 2022, less than 1Mt, was obtained from low-emitting technologies, consistent with data of previous years. Up to now, despite a 35% increase in 2022 respect to the previous year,

the H_2 production from water electrolysis still amounted to only to 100,000 tons, accounting only for 0.1% of today's hydrogen production. [7]

The current aim is to increase the annual 0.7% of hydrogen produced by renewable and low-emitting resources. According to announced projects, this number could increase up to 20Mt in 2030, relying on fossil fuels-based production with CCUS and water electrolysis. [7]

The chart below illustrates the current state and the future potentials of projects for hydrogen production through low emitting production routes. The production methods included are water electrolysis and fossil fuel usage with CCUS and hydrogen production capacity is measured in million tons. [7]

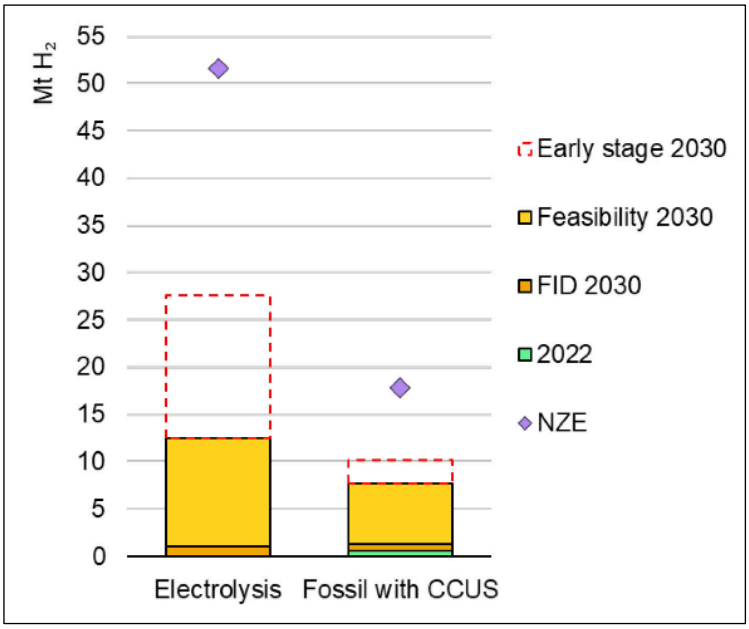

***Figure 4**: Current state and the future potentials of projects for hydrogen production through low emitting production routes. [7]*

The very small green bar represents the production level for both methods in 2022, indicating the current minimal contribution of these low-emitting technologies respect to global hydrogen production. The orange bar represents the expected H_2 production levels in 2030 after the final investment decision (addressed as "FID") is made. Additionally, a yellow bar and a red dashed line represent respectively projects that can potentially be feasibly and be at early stages in 2030. Moreover, the purple diamonds indicate the net zero emissions (NZE) targets, highlighting the importance of hydrogen in the context of meeting global climate goals and transitioning to a more sustainable energy system. To sum up, most of the projects are currently under investigation, while others are at very early stages, the projects that have reached the final investment decision or are under construction, represent only the 4%. [7]

2.3. Water Electrolysis and Reactions' Thermodynamics

As the demand for hydrogen and sustainable energy source continues to rise, water electrolysis emerges as a promising method to yield green hydrogen and it is expected that, in the future, more than 70% of low-emissions hydrogen will be produced with this technology. [7]

Water electrolysis is a chemical process that breaks down water (H_2O) into oxygen (O_2) and hydrogen (H_2). The endothermic, non-spontaneous reaction is driven by electrical energy: [5]

$$H_2O + \text{energy} + \text{heat} \leftrightharpoons H_2 + \frac{1}{2}O_2$$

When the electricity supplied to the electrolyzer derives from renewable sources, green hydrogen is generated, avoiding greenhouse gasses emissions. [5]

Water electrolysis can be implemented to store excess energy during periods of low demand, mitigating the intermittent nature of renewable energy sources. Electrolyzers and fuel cells play a complementary role in this context: electrolyzers are suitable for large scale and medium-long term storage by converting surplus energy into hydrogen, while fuel cells convert hydrogen back into electricity. Differently from batteries that are not a good storage option for wind energy, for example, electrolyzers can handle high current inputs per unit surface. [5]

In the figure below there is a representation of a system of water electrolysis, from renewable sources that can be supplied to the electrolyzer, to potential hydrogen application.

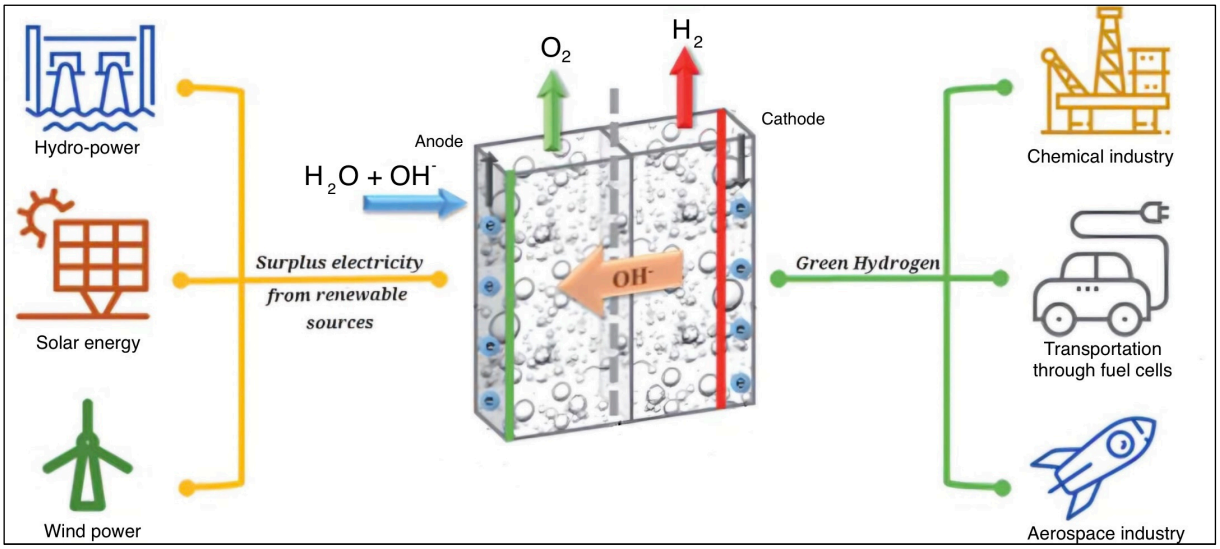

***Figure 5**: Representation of anion exchange membrane electrolysis with applications. Adapted from reference [10]*

The overall water splitting reaction consists of two half-cell reactions: the Oxygen Evolution Reaction (OER) is the formation of oxygen occurring at anode; while the Hydrogen Evolution Reaction (HER) generates hydrogen and takes place at cathode. [3,6]

For the reaction to proceed, it is essential the passage of ions between the two electrodes, where the oxidation and reduction reactions occur. To enhance the low conductivity of water, electrolytes are added, which can be acidic or alkaline, depending on the type of water electrolysis. Sulfuric acid (H_2SO_4) is commonly used in PEMWE, while potassium hydroxide (KOH) or sodium hydroxide (NaOH) solutions are chosen for AWE and AEMWE. The semi-reactions and the electrolyte depend also on the membrane used in the process. [1]

Under alkaline conditions, the reaction proceeds as follows: [6]

Anode	$4\ OH^- \rightarrow O_2 + 2\ H_2O + 4\ e^-$	$E^o = 0.401V$ [6]
Cathode	$4\ H_2O + 4\ e^- \rightarrow 2\ H_2 + 4\ OH^-$	$E^o = -0.828V$ [6]
Net reaction	$2\ H_2O \rightarrow 2\ H_2 + O_2$	$\Delta E° = -1.23$ [1,6]

In alkaline environments, water undergoes reduction at cathode, resulting in the production of hydrogen (H_2) and hydroxide ions (OH^-). Due to the positive attraction of the anode, OH^- anions spontaneously diffuse toward it through the Anion Exchange Membrane (AEM) of AEMWE or the porous diaphragm of traditional alkaline electrolyzers. At anode, OH^- are oxidized, releasing water, oxygen and electrons. Electrons flow from anode to cathode through the external circuit. [6]

In acidic media, the process consists in the following reactions: [1]

Anode	$2\ H_2O \rightarrow O_2 + 4\ H^+ + 4\ e^-$	$E^o = +1.23V$ [1]
Cathode	$4\ H^+ + 4\ e^- \rightarrow 2\ H_2$	$E^o = 0.0\ V$ [1]
Net reaction	$2\ H_2O \rightarrow 2\ H_2 + O_2$	$\Delta E° = -1.23V$ [1,6]

When an acidic electrolyte is used, water is oxidized at anode, producing oxygen and protons (H^+). The protons cross the Proton Exchange Membrane (PEM) and spontaneously diffuse towards the cathode due to its negative charge. At the cathode, protons are reduced to form oxygen. Electrons flow from anode to cathode, through the external circuit. [6]

The electrochemical process of water electrolysis is governed by thermodynamic and kinetic factors, both playing a crucial role in determining the feasibility and the efficiency of hydrogen

production. Thermodynamics defines the minimum energy requirement for the reaction, whereas kinetics determines the rate at which the reaction proceeds.

Thermodynamic parameters of water electrolysis change depending on the temperature. In particular, below 100°C water is in liquid state, whereas the products oxygen and hydrogen are gaseous: additional energy is required to convert water into vapor before it can be decomposed. At temperature higher than 100°C, water is already in vapor phase and there is no need to consider the energy needed for the phase change. [5,11]

Table of values of enthalpy change, Gibbs free energy change and entropy change for both conditions are provided.

In standard conditions of temperature and pressure (temperature = 298K, pressure = 1 bar), when water is in liquid form, whereas oxygen and hydrogen are gaseous, thermodynamic parameters are as follows:

Parameter		Value	Reference
$\Delta H°_{(l)}$	Enthalpy change	285.84 kJ/mol	[5]
$\Delta S°_{(l)}$	Entropy change	163.6 J/mol·K	[5]
$\Delta G°_{(l)}$	Gibbs Free energy change	237.2 kJ/mol	[1]

Table 1: *Thermodynamics parameters for water electrolysis, assuming the process to be in standard conditions (298 K, 1 bar) [1,12]*

Thermodynamic parameters of water vapor at 373 K (100°C) are listed in the table below:

Parameter		Value	Reference
$\Delta H°_{(vap)}$	Enthalpy change	241.80 kJ/mol	[5]
$\Delta S°_{(vap)}$	Entropy change	44.10 J/mol·K	[5]
$\Delta G°_{(vap)}$	Gibbs Free energy change	228.66 kJ/mol	[1]

Table 2*: Thermodynamics parameters for water electrolysis, assuming the process to be at 373 K (100°C), 1bar. [1,12]*

In an isobaric system, the energy required for a reaction to occur is given by the enthalpy change associated with the reaction, ΔH°. [11] The ΔH° of water electrolysis is the total energy required to break the bonds of water molecules to form hydrogen and oxygen. It has a positive value,

indicating that the reaction is endothermic. [5] This energy can be supplied in form of electrical energy, represented by Gibbs free energy change (ΔG°), and thermal energy (Q). [11]

The following relationship holds: [11]

$$\Delta H^\circ = \Delta G^\circ + Q = \Delta G^\circ + T \cdot \Delta S^\circ$$

Where:

- ΔH° (kJ/mol) is the enthalpy change,
- ΔG° (kJ/mol) is the Gibbs free energy change,
- ΔS° (J/mol·K) is the entropy change,
- T (K) is the absolute temperature of the system,
- Q (kJ/mol) is the heat adsorbed in the reaction.

The Gibbs free energy represents the minimum energy required to drive a non-spontaneous reaction. [12] The ΔG° of water electrolysis has a positive value, this indicates that the reaction is endergonic, non-spontaneous without an external energy source. [11]

The Gibbs free energy change for liquid water, $\Delta G^\circ_{(l)}$, can be calculated using the equation: [12]

$$\Delta G^\circ(l) = \Delta H^\circ(l) - T(l) \cdot \Delta S^\circ(l)$$

Where:

- $\Delta G^\circ_{(l)}$ (kJ/mol) is the Gibbs free energy change of liquid water,
- $\Delta H^\circ_{(l)}$ (kJ/mol) is the enthalpy change of liquid water,
- T (K) is the absolute temperature of the system,
- ΔS° (J/mol·K) is the entropy change.

The entropy change is a measure of the disorder in the system. Considering water electrolysis below 100°C, ΔS° has a so high value due to the phase transition of liquid water into the two gaseous products. The increase in entropy should favour the reaction by promoting disorder, however the highly positive enthalpy counteracts this effect, keeping the Gibbs free energy positive and the reaction nonspontaneous. [12]

For an electrochemical reaction, ΔG° can be related to the cell potential applied across the cell and the total charge transferred in the reaction. It is expressed by the following equation: [12]

$$\Delta G^\circ = -nF\Delta E^\circ_{\text{cell}}$$

Where:

- ΔG° (kJ/mol) is the Gibbs free energy change,
- n is the number of electrons transferred in the reaction,
- F (C/mol) is the Faraday constant (approximately 96,485 C/mol),
- ΔE°_{cell} (V) cell is the cell potential in standard conditions.

In a nonspontaneous reaction, such as water electrolysis, ΔG > 0, and due to the negative sign in the equation, $\Delta E^\circ_{cell} < 0$, meaning that an external voltage is needed for the reaction to occur. [12]

In electrolyzers, two different thermodynamic voltages are identified: the free energy electrolysis voltage "E", also called reversible potential; and the thermoneutral voltage "V", often referred to as enthalpy potential.

The free energy electrolysis voltage "E" represents the minimum voltage in terms of electrical energy required to drive the nonspontaneous electrolytic reaction, it does not consider any heat required for the reaction. For water electrolysis, in standard conditions of temperature and pressure (temperature = 298K, pressure = 1 bar), it is calculated through the equation: [12]

$$E(T,P) = \frac{\Delta G(T,P)}{nF} = 1.23V$$

Where:

- $E_{(T,P)}$ (V) is the free energy electrolysis voltage at a given temperature T and pressure P,
- $\Delta G_{(T,P)}$ (kJ/mol) is the Gibbs free energy change reaction at a given temperature T and pressure P,
- n is the number of electrons transferred in the reaction,
- F (C/mol) is the Faraday constant (approximately 96,485 C/mol).

At voltages below 1.23V, the reaction will not proceed. [1,5,6] This value represents the thermodynamic minimum potential required for the reaction to occur under ideal conditions. [5,13]

However, in addition to the electrical energy represented by Gibbs free energy and the reversible potential E, the system also requires heat to satisfy the enthalpy change of the

reaction. In practical applications, the system must operate at a potential equal or greater than the thermoneutral voltage V, to account for the heat required by the reaction. The thermoneutral voltage allows the reaction to proceed without any net heat absorption or release ensures a balanced, isothermal electrolysis process. It is calculated as: [12]

$$V(T,P) = \frac{\Delta H(T,P)}{nF} = 1.48V$$

Where:

- $V_{(T,P)}$ (V) is the thermoneutral voltage at temperature T and pressure P,
- $\Delta H_{(T,P)}$ (kJ/mol)is the enthalpy change of the reaction at a given temperature T and pressure P,
- n is the number of electrons transferred in the reaction,
- F (C/mol) is the Faraday constant (approximately 96,485 C/mol).

When the applied voltage equals thermoneutral potential, the electrical energy covers also the heat requirements. [12]

Given the endothermic nature of the reaction, if the necessary heat is not supplied, either through an external heating source or by maintaining the thermoneutral voltage, the system will draw this energy from its surroundings, resulting in a decrease in the temperature of the system or its immediate surroundings. This cooling effect can negatively impact the reaction's efficiency, affecting both the equilibrium and the reaction kinetics.

Increasing the operating temperature of the electrolyzer reduces the necessary voltage input. However, high-temperature electrolysis raises concerns, such as potential damage to the components of the electrolyzer stack. Also, the cost of heat supply must be considered, although it could potentially be mitigated whether the electrolytic system is integrated with an exothermic process. [5,11]

2.4. Reactions Kinetics: Overpotentials

In real systems, when current is applied, a voltage higher than the thermoneutral voltage V is required to drive the electro splitting of water molecules, due to several energy losses. [5,13] This additional voltage, known as “overpotential”, represents the excess energy required beyond the theoretical potential ΔE° to overcome intrinsic barriers in the reaction system, including all the resistances that impede the reaction progress. [1,6]

The actual operative voltage of electrolyzers ranges from 1.6V to 2.0V, with this variability depending on the pH of the electrolyte and the effectiveness of the electrocatalysts involved in the oxygen and hydrogen evolution reaction. [1]

The actual operating voltage E_{cell} includes the theoretical voltage ΔE°, plus all the overpotentials and can be calculated with the following equation: [14]

$$E_{\text{cell}} = \Delta E^{\circ} + \eta_{\text{act}} + \eta_{\text{ohmic}} + \eta_{\text{conc}}$$

Where:

- E_{cell} (V) is the final operating voltage,
- ΔE°(V) is the theoretical voltage,
- η_{act} (V) is the activation overpotential,
- η_{ohmic} (V) is the ohmic overpotential,
- η_{conc} (V)is the concentration overpotential.

A crucial aspect to take into consideration is that hydrogen production rate of water electrolysis is directly proportional to the current supplied to the electrolyzer, as with current rise, the number of reactions occurring per unit time increases. However, as the current is raised to enhance hydrogen production, the operative voltage also increases, because all the overpotentials increase. In particular, ohmic overpotential rises linearly with the current, while activation and concentration overpotential follow more complex, non-linear dependencies, as described in following sections.

Since this will lead to higher power consumption at elevated current densities, a balance between hydrogen production and energy efficiency is needed.

2.4.1. Activation Overpotential

The activation overpotential (η_{act}) is also known as charge transfer overpotential and represents the energy needed to break the chemical bonds before the reaction can proceed. This overpotential depends on electrochemical kinetics, electron and proton migration. Activation overpotential increases as the current rises, since the number of reactions per unit time also increases, resulting in more energy needed to compensate the kinetics. [1,14]

The relationship between current density and both anodic and cathodic activation overpotentials is described by Butler-Volmer equation: [1]

$$j = j_0 \left[e^{\frac{\alpha n F \eta}{RT}} - e^{\frac{-(1-\alpha) n F \eta}{RT}} \right]$$

Where:

- j (A/m^2) is the current density;
- j_0 is the exchanged current density;
- α is the charge transfer coefficient;
- n is the number of electrons involved in the reaction;
- F is the Faraday constant;
- η is the overpotential: the first term is the anodic contribution, while the second the cathodic one.
- R is gas ideal constant;
- T(K) is the temperature.

When the equilibrium potential (E_{eq}) is applied to the electrodes, the oxidation and reduction reactions occur at identical rates. At microscopic level, there is a continuous flux of electrons between electrodes and electrolyte, but for every electron that enters the electrode for reduction, another electron exits the electrode through oxidation. As a result, the anodic and cathodic currents are equal in magnitude but opposite in direction, neutralizing each other and producing no net current in the external circuit.
The exchange current density (j_o) is the current density that flows equally in both forward and backward direction at equilibrium. This parameter represents the intrinsic rate of the oxidation and reduction reactions under equilibrium conditions and is a key indicator of catalyst efficiency: a higher value indicates faster reaction kinetics and lower overpotential values.

The value of the exchange current density is calculated by extrapolating the linear fit of a logarithmic graph that relates the current to the overpotential, up to the point where the overpotential is ideally zero, estimating the theoretical current under equilibrium conditions. This value depends on the catalyst material, the electrolyte, and the operating temperature. [1]

The charge transfer coefficient α describes how the electrical potential at the electrode-electrolyte interface is effective in reducing the activation energy for an electrochemical reaction. This parameter, with a value ranging from 0 to 1, provides insights on the symmetry of the reaction, specificity how the applied potential influences the rate of oxidation versus reduction. When it is equal to 0.5, both the anodic (oxidation) and cathodic (reduction) activation energy barriers are equally affected by changes in electrode potential.

When the activation overpotential is very small, around 10mV, the exponents in the Butler-Volmer equation can be approximated to linear behaviour, as follows:

$$j \approx \frac{nj_0F}{RT}\eta$$

Instead, Tafel equation is a simplification of Butler Volmer equation appliable only at high overpotentials: [1,14]

$$\eta_{\text{act}} = a + b \ln j$$

Where:

- η_{act} (V) is the activation overpotential;
- a is a constant specific to the Tafel equation, depending on the reaction and catalyst material, with separate values tabulated for the cathode and anode;
- ln is natural logarithm;
- j (A/m^2) is the current density;
- b is the Tafel slope, also distinct for the anode and cathode.

Specifically, to apply the Tafel equation to determine the Tafel slope, the overpotential must be higher than RT/F, typically the minimum value is around 45−50 mV, in order to neglect contributions from the back reaction. [5]

Indeed, when the absolute value of overpotential (|η|) is high, one of the two exponential terms of the equation dominates the process. For example, when it is very positive, around 100 mV, the anodic reaction dominates the process, and between the current density and the overpotential there is a measurable logarithmic correlation. On the other hand, when the overpotential is very negative, e.g. -100 mV, the cathodic reaction dominates, and a similar logarithmic relationship is observed for the reduction process. [1,14]

The Tafel plot is a graph that describes the correlation between the overpotential and the natural logarithm of the current density. The slope of the resulting straight line is the Tafel slope, a parameter which quantifies how quickly the overpotential increases as the current density rises. A smaller value indicates that a higher increase in current density results in a small increase in overpotential, indicating more efficient reaction kinetics. [1]

The Tafel plot is experimentally obtained by recording polarization data (recording current while varying the potential), converting the current density values to their natural logarithm, and plotting the results against the overpotential. The linear region of the plot, where the overpotential and the natural logarithm of the current density exhibit a linear relationship, is identified and the Tafel slope (b) and the intercept (a) are determined by performing a linear fit of the data in this region. To ensure accuracy, the Tafel slope must be measured under steady-state conditions. It is important to note that values higher than 120 mV/dec indicate the presence of other phenomena, that cannot be attributed to the kinetics of the reaction, e.g. structural changes in the catalyst or the formation of resistive surface layers. [5]

An electrocatalyst is required for both OER and HER to overcome the kinetics of the reactions: it will reduce the activation overpotential, improving the efficiency of the system. [6,13] Tafel slope is used to compare the performance of different electrocatalysts: an effective catalyst presents a small Tafel slope, because it minimizes the increase in overpotential required to achieve higher current densities. Moreover, the morphology of the catalyst plays a crucial role in reducing the activation overpotential by enhancing the reaction kinetics: porous structures and nanostructures provide a larger surface area, exposing more active sites for the reactions.

The operating temperature has also an effect on reaction kinetics, with higher temperatures resulting in faster electrochemical reactions and lower activation overpotentials. However, the temperature must be carefully controlled to avoid damages on stacks materials, particularly on the anion exchange membrane.

2.4.2. Ohmic Overpotential

Ohmic overpotential results from electrical resistances at surfaces and interfaces in the system, it increases linearly with the current following Ohm's law:

$$\eta_{\text{ohmic}} = I \cdot R_{\text{ohm}}$$

Where:

- η_{ohmic} (V) is the ohmic overpotential;
- I is the current;
- R_{ohm} is the total ohmic resistance.

The total ohmic resistance is given by the sum of the resistances caused by the electrolyte, the electrodes, the membrane and the bipolar plates. Therefore, the product of the resistances and the current gives the value of ohmic overpotential, described by the formula: [1,14]

$$\eta_{\text{ohmic}} = I \cdot (R_{\text{ele}} + R_{\text{ey}} + R_{\text{mem}} + R_{\text{bp}})$$

Where:

- η_{ohmic} (V) is the ohmic overpotential,
- I (A) is the applied current,
- R_{ele} (Ω) is the resistance due to electrodes,
- R_{ely} (Ω) is the resistance due to electrolyte,
- R_{mem} (Ω) is the resistance due to the membrane,
- R_{bp} (Ω) is the resistance due to the bipolar plates.

The electrode resistance is the sum of electrical resistance of both anode and cathode and depends on factors such as the length and the area of the electrode, together with the resistivity of electrode materials. The resistance of the electrolyte depends on its composition and on the eventual presence of bubbles formed during the reaction, which can increase this value reducing the contact area between electrode and electrolyte. [14]

However, the membrane typically represents the highest resistance source. [1,5] This value depends on several chemical-physical characteristics of the membrane, such as tortuosity, thickness, wettability, porosity and area. [14] Lower tortuosity, a thinner, larger membrane

simplifies the ionic transport path. Good wettability improves ionic conductivity, while optimal porosity facilitates ion mobility by providing adequate volume for electrolyte transport. However, these parameters must be balanced to avoid compromising the mechanical stability of the polymeric membrane, this aspect will be discussed in paragraph 2.9.1.

2.4.3. Concentration Overpotential

Mass transfer, or concentration overpotential, results from mass transport limitations that determine a non-stoichiometric supply of reactants to the catalytic centre. This value is affected by the thickness and porosity of electrode that determines the ease of diffusion through it. [5] Applying Nernst equation, it is possible to calculate the mass transfer overpotential: [1]

$$\eta_{\text{conc}} = \frac{RT}{nF} \ln \frac{C}{C_0}$$

Where:

- η_{conc} (V) is the concentration overpotential,
- R (J/mol K) is the gas constant (approximately 8,3145 J/mol K),
- n is the number of electrons transferred in the reaction,
- F (C/mol) is the Faraday constant (approximately 96,485 C/mol),
- C is hydrogen or oxygen concentration at electrode-membrane interface,
- C_o is the reference concentration, often bulk electrolyte concentration.

As the current density increases, the number of reactions occurring at the electrode surface also increases, resulting in a higher concentration of product species at the reaction interface. Consequently, overpotential caused by mass transport limitation increases too. [1]

However, concentration losses occur at very high current densities, higher than current density operating range of electrolyzers, for this reason its effect can be neglected. [1,14]

The relationship between voltage and current density is described by polarization curves, with the three types of overpotentials contributing to the characteristic shape of the current-voltage curve. A typical polarization curve for an electrolyzers is showed below.

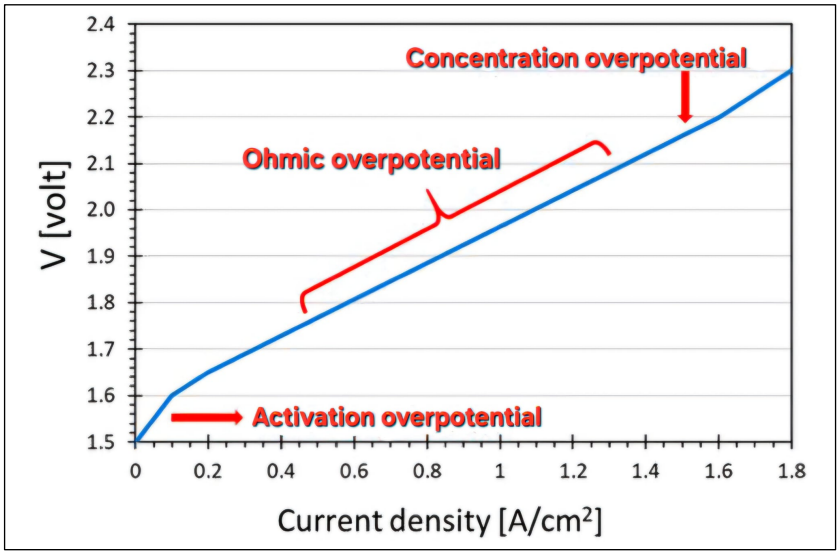

Figure 6: *Typical polarization curve of an electrolyzer. Adapted from reference [15]*

The activation overpotential impacts the initial portion of the curve, where electron transfer reactions occur, called “activation overpotential region”. In this region, the voltage increases rapidly with current density, with an exponential relationship. At increased current densities, there is the “ohmic overpotential region”, where the voltage rises linearly with the current. In this current region, the current is limited by the internal resistance to ion flow, including material's resistance, with the anion exchange membrane being the most significant contributor. As the current density increases further, the curve reaches the "concentration overpotential region”, where the reaction rate is strongly limited by the mass transfer, specifically the ability of water to reach electrode's surface and produced gasses to be removed. [15]

To reduce overpotentials, the following strategies can be employed:

- Activation overpotential: increase the operating temperature (with the drawback of damages on components of the stack), employ effective catalysts, decrease catalyst’s particle size and enhance its porosity.
- Ohmic overpotential: use materials with good electrical conductivity, reduce the thickness of components, use high-conductivity membranes (considering issues with mechanical strength, described in paragraph. 2.9.1.).
- Concentration overpotential: optimize flow management to improve mass transport.

2.5. Electrolysis Classification

Electrolytic cells are primary composed by the electrodes and the electrolyte, the latter carries and conducts ions from one electrode to the other during the reactions. [3]

Several types of water electrolyzers have been developed and can be classified based on the electrolyte type or the operative temperature.

The electrolyte can be either liquid or solid. Moreover, electrolysis can occur in both alkaline and acidic media, the two reactions are comparable, the main difference is that in the alkaline environment, the conducting species is the hydroxide anion (OH^-); while in acidic conditions, this role is assumed by the hydrogen cation (H^+). [3,5]

Electrolytic cells can also be designed to operate at different temperatures, which influences both the reactions, and the materials used. In general, they can be categorized into two types: low-temperature electrolyzers and high-temperature electrolyzers. Low-temperature cells, operating up to 100°C, include Alkaline Water Electrolyzers (AWE), Proton Exchange Membrane Water Electrolyzer (PEMWE) and Anion Exchange Water Electrolyzers (AEMWE). In contrast, high-temperature ones, operating above 500°C, include Solid Oxide Electrolysis Cells (SOEC) and Molten Carbonate Electrolytic Cells (MCEC). [3,11]

Water electrolyzers can be further classified, based on their design, in “finite” or “zero-gap” configuration. In both systems, a separator or a membrane is always placed between anode and cathode, serving to keep the two compartments distinct and to prevent the mixing of produced gasses. This material also ensures ion mobility: it selectively conducts ions (OH^- or H^+, based on the electrolyte) and water, but not O_2 and H_2. The design, whether finite-gap or zero-gap, depends on the thickness and chemical nature of the separator. [5]

In a finite-gap design, there is a measurable distance between the anode and the cathode, determined by the thickness of the porous separator, that can reach 2mm. In contrast, in a zero-gap configuration, the two electrodes are separated without a visible distance between them, utilizing thin polymeric membrane with low permeability to O_2 and H_2. [5]

While the finite-gap configuration decreases the crossover of the gasses, also results in an increase of ohmic resistance, consequently, the current density can reach maximum 0,25A/cm^2, which makes this design not suitable for the integration with renewable forms of energy.

On the other hand, zero-gap design reduces ohmic resistance, lowering the voltage required for a given current density; however, it may introduce issue relative to crossover of gasses. [5]

The figure below illustrates the finite gap (a) and zero gap (b, c) configurations.

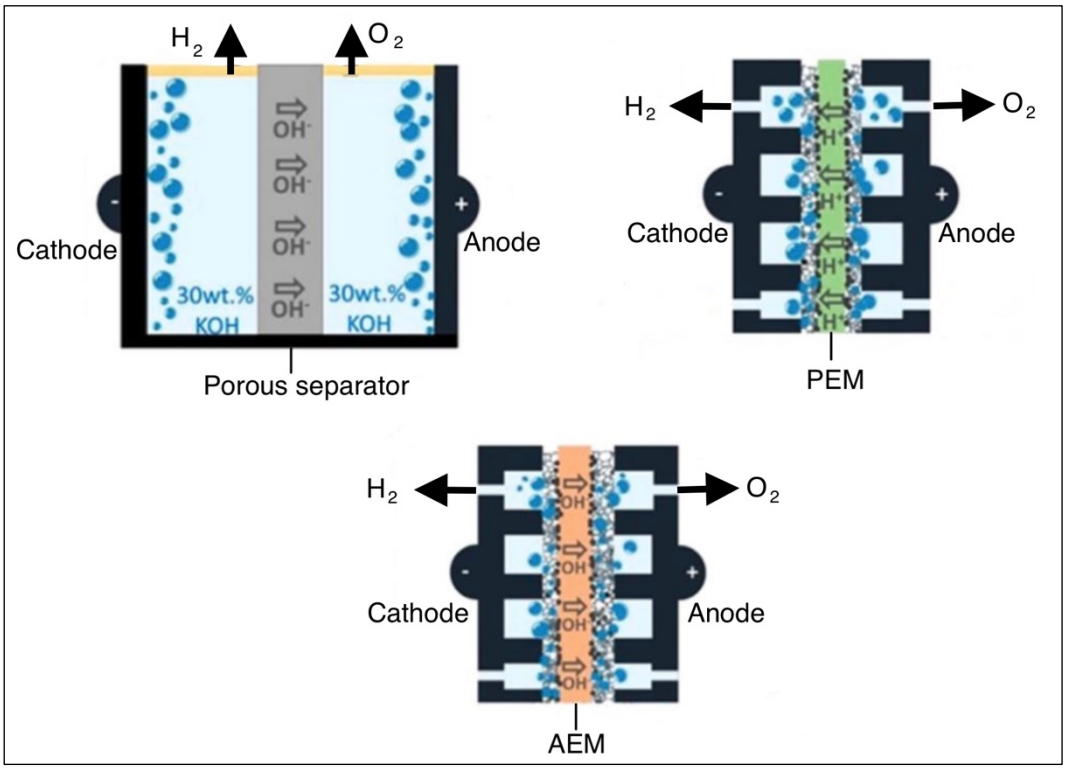

Figure 7: *Schematic representation of three types of electrolyzers: a) AWE finite gap system, b) zero-gap PEMWE, c) zero gap AEMWE. Adapted from reference [5].*

2.5.1. AWE: Alkaline Water Electrolyzers

Traditional Alkaline Water Electrolyzers (AWE) represent one of the most established and most widely used electrolytic technology for hydrogen production. [16] Typically, AWE operates at a current density ranging between 0.2 A/cm^2 and 0.4 A/cm^2, with a cell voltage in the range 1.85–2.2 V and at moderate temperatures of 70–90°C. [6,13]

The main advantage of this technology is that it does not rely on noble metal catalyst, resulting in lower costs respect to Proton Exchange Membrane Water Electrolyzers (PEMWE). [6] Indeed, anode and cathode are usually composed by, respectively, Nickel and Cobalt oxides. [13]

The electrolyte typically consists of an aqueous solution of concentrated (20/30%) sodium hydroxide (NaOH), or potassium hydroxide (KOH), both creating an alkaline environment. [6] However, concentrated electrolyte can lead to corrosion problems on components of the system, affecting durability and reliability of the whole electrolyzer. [17] Another issue related to the electrolyte is that both KOH and NaOH are sensitive to atmospheric CO_2, resulting in formation of carbonates, that have an impact on the performance of electrolysis. The reaction consumes KOH or NaOH, in this way it reduces the number of OH^- available, thus decreasing the ionic conductivity of the electrolyte. Furthermore, the salt can precipitate in the pores of the electrode and porous transport layer, obstructing ion transfer and physically blocking the access of water to the active sites and the release of H_2 and O_2 from the active sites. [6,18]

Alkaline electrolyzers can be designed either in finite or zero-gap configuration. In the figure below, both types of configurations are showed.

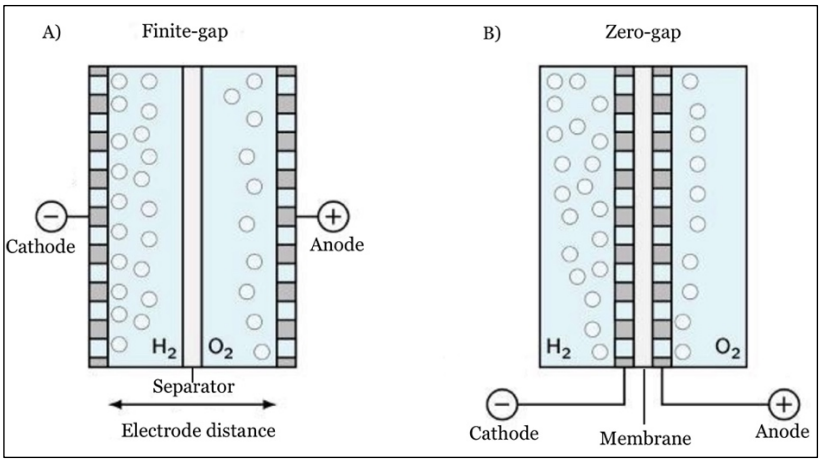

Figure 8: *Different cell designs for traditional alkaline water electrolysis: (a) finite gap configuration; (b) zero gap configuration. Adapted from reference [19]*

In finite gap alkaline electrolyzers, a porous separator of a thickness up to 2mm, such as Zircon and Perl UTP 500, is placed between the electrodes. [5]

In zero-gap configuration, separators are made by ceramic oxides (asbestos or potassium titanate), or polymers (polypropylene or polyphenylene sulphide). [6]. Despite reducing the ohmic resistance, the diaphragm of alkaline electrolyzers cannot completely prevent the crossover of gas from the two compartments, causing O_2 diffusion from anode into the cathode side, where it reacts with H_2 forming H_2O and reducing the purity of H_2 and the efficiency of the electrolyzer. Moreover, safety concerns arise when the mixing of these two gases occurs. [16]

To overcome the crossover problem, AWE systems should operate at high current density, which increase electrochemical reactions by reducing the residence time of gasses within the system. However, this solution leads to a high overpotential due to increased resistance of the diaphragm, requiring extra voltage to drive the electrochemical reaction beyond its equilibrium voltage. [17]

After AWE, Proton Exchange Membrane Water Electrolyzers (PEMWE) and recently Anion Exchange Membrane Water Electrolyzers (AEMWE) technologies have been developed. Both types are used in zero gap configuration, with PEMWE in acidic environments and AEMWE in basic conditions. [5]

2.5.2. PEMWE: Proton Exchange Membrane Water Electrolyzers

Proton Exchange Membrane Water Electrolyzers (PEMWE) represent a relatively young technology, developed in 1960s, showing good stability, good performance and the potential to address some of the limitations of alkaline electrolyzers, such as their limited achievable current density. [6,16,17] Indeed, PEMWE can operate at a current density of 2 A/cm^2 at 90 °C, at about 2.1 V. [6,13,17]

PEMWE foresees the presence of a polymeric membrane as solid electrolyte, typically a perfluorosulfonic acid (PFSA) membrane, such as Nafion. The membrane conducts hydrogen cations (H^+) from anode to cathode and separates H_2 and O_2 that are produced. [6] Nafion membranes are composed of a polytetrafluoroethylene (PTFE) backbone, a polymer consisting of carbon and fluorine atoms, which provides chemical stability. Attached to the PTFE skeleton there are double ether perfluoro side chains, that terminate in sulfonic acid groups ($-SO_3H$), the ionically active part of the membrane. [20]

The acidic nature of the electrolyte allows a faster water electrolysis reaction's kinetic compared to alkaline systems [6]. In acidic environments, many protons are available for immediate charge-discharge and H_2 is produced directly from protons, enhancing the efficiency of the reaction; while in alkaline conditions, before H_2 can be formed, the strong H-O bond in water molecules has to be broken. [1]

In addition, Nafion membrane provides high conductivity, due to the high mobility of H^+. Moreover, it is more effective at reducing crossover respect to the diaphragm of AWE, resulting in a higher purity of the hydrogen produced and a more efficient system. [17] Moreover, the absence of the corrosive caustic electrolyte used in alkaline electrolyzers, makes the technology safer. [6]

However, the acidic environment requires the use of specialized and expensive materials, along with noble metal-based catalyst. [16] Specifically, oxygen evolution reaction can only be effectively catalysed by expensive and precious metal oxides, such as Iridium or Ruthenium alloys, which offer a minimal overpotential. [1] Usually, in PEMWE systems, anode and cathode are respectively made of IrO_2 and Pt. [13]

PEMWE can operate under high pressure, meaning that hydrogen can be supplied to the end-user in a high-pressure state. This hydrogen is ready for usage or storage, eliminating the need

for additional compression steps, representing a significant economic advantage. Moreover, high pressure increases mass transport efficiency by reducing the volume of gas near the electrode. A differential pressure mode is typically used: anode and cathode are maintained under different pressure conditions, creating a pressure gradient. This system mitigates the dangers associated with handling pressurized oxygen and the risk of titanium self-ignition in oxygen. The pressure gradient acts as an additional driving force for the permeation of hydrogen cations through the membrane, moreover it partially returns the oxygen blocked inside the membrane back to the anode, minimizing oxygen crossover. [21]

However, highly pressurized systems raise safety concerns and considerations about stack durability in high pressure conditions. In particular, to maintain the critical concentration of H_2 in O_2 below the safety threshold of 4% by volume at pressures higher than 100bars, thick membranes are necessary. These membranes possess higher resistance, reducing the efficiency of the system. Moreover, the components of the stack can be degraded under such critical pressure conditions: membranes are more prone to rupture, and the degradation and corrosion of the metallic components, such as bipolar plates, electrodes, current collectors, is faster. For these reasons, although some commercial PEMWE have achieved an output pressure of 700 bar, the average pressure is kept in the range between 30-50bar. [21]

The figure below presents the typical configuration for PEMWE.

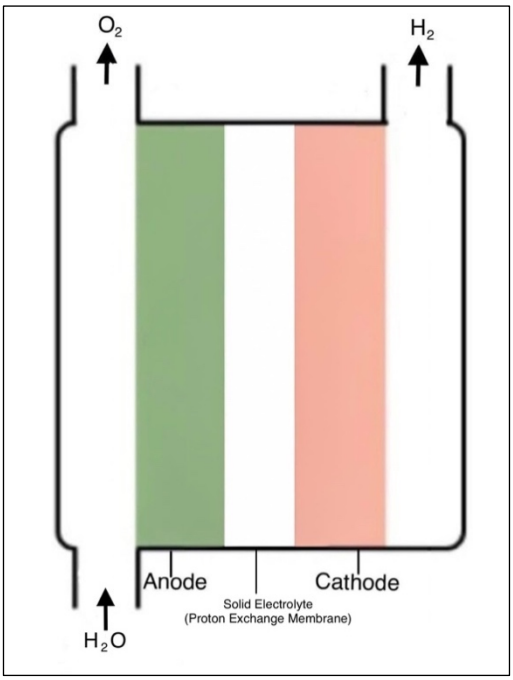

***Figure 9**: Typical configuration of PEMWE. Adapted from reference [22].*

2.5.3. AEMWE: Anion Exchange Membrane Water Electrolyzers

Anion Exchange Membrane Water Electrolyzers (AEMWE) represent an emerging technology that combine some of the best features of AWE and PEMWE, resulting in an inexpensive and high-performance solution, which can reach high operation current density of 2 A/cm^2 at 2.1 V. [17,23]

The table below compares the properties of AEMWE with those of AWE and PEMWE, highlighting the differences in operating conditions, costs, and technological readiness. [6]

	AWE	**PEMWE**	**AEMWE**
Electrolyte	20-30% KOH	PFSA	3-10% KOH
Charge carrier	OH^-	H^+	OH^-
Separator	Porous diaphragm	Nafion membrane	Anion Exchange Membrane
Temperature range (T°)	65-100 °C	70-90 °C	50-70 °C
Typical discharge H_2 pressure (bar)	25-30 bars	30-80 bars	30 bars
OER catalyst	Ni_2CoO_4 La-Sr-CoO_3 Co_3O_4	Ir oxides Ru oxides	NiO $NiFe_2O_4$ Co_3O_4 $CoFe_2O_4$ $CoNiO_2$ $CoFeNiO_4$
HER catalyst	Ni	Pt/C	Pt/C CeO_2-La_2O_3
Conventional current density (A)	0,2-0,5 A	0,8-2,5 A	Up to 2 A
Typical voltage range (V)	1,85-2,2 V	Around 2,1 V	Around 2,1 V
Hydrogen purity (vol%)	99.3-99.9	99.9999	99.99
System costs (€/kg)	800-1300 €/kg	1200-2000 €/kg	NA
Technology status	Mature	Mature	R&D

Table 3: *Comparation of main features of AWE, PEM and AEM electrolyzers [6].*

Similarly to AWE, in AEMWE the environment is kept alkaline to reduce the electrocatalysts' price: non platinum group catalysts are used. Moreover, the alkaline environment makes possible the usage of inexpensive bipolar plates and porous transport layer. [23] Electrolytes are usually liquid aqueous solution of KOH or NaOH, the latter is more affordable but exhibits lover conductivity values. [16] AEMWE typically operate at electrolytes concentration ranging from 3 to 10% by mass [16] to bypass corrosion issues associated with traditional alkaline systems, which foresees the use of 20-30% concentrated electrolyte. [17] In traditional alkaline electrolyzers, OH^- conduction occurs only through the liquid electrolyte, since the porous diaphragm is merely a separator that allows OH^- ions passage without being conductive by itself. For this reason, the performance of traditional alkaline water electrolysis reaction is directly proportional to the electrolyte concentration: a higher concentration of anions reduces the polarization resistance of electrodes and overall cell resistance. [16] In contrast, in AEMWE less concentrated electrolytes can be used because the Anion Exchange Membrane (AEM) contains cationic groups that coordinates with OH- ions, making the membrane itself conductive.

The key similarity with PEMWE is the use of membrane separation, more effective at reducing crossover compared to the diaphragm used in alkaline systems. In AEMWE, this is achieved through a dense polymeric Anion Exchange Membrane (AEM), which conducts OH^- anions. However, the long-term stability of AEM electrolyzers is still under investigation, as it is limited by the stability of the polymeric backbone and pendant cationic group. This topic will be discussed in detail in paragraph 2.7.1. [17]

In the figure below there is an operational scheme of an anion exchange membrane electrolyzer.

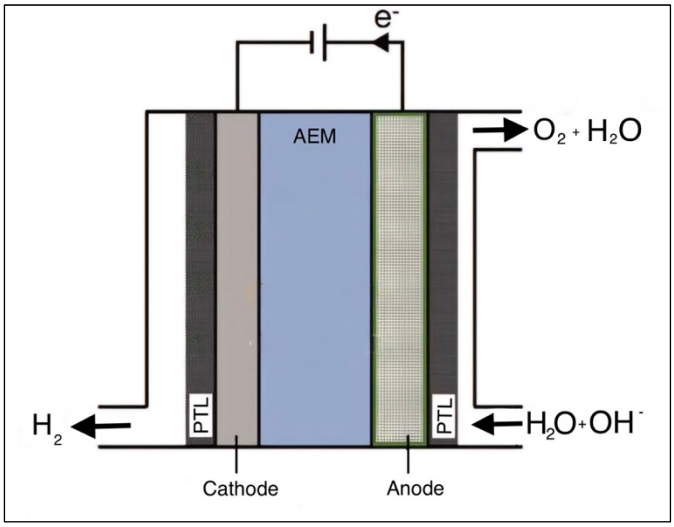

Figure 10: *Operational scheme of anion exchange membrane electrolyzer. Adapted from reference [13].*

2.6. Hydrogen Evolution Reaction in Alkaline Conditions

To analyse Anion Exchange Membrane electrolysis, it is crucial to examine Hydrogen and Oxygen Evolution Reactions in alkaline conditions, as both can be divided into different steps.

In alkaline conditions, the first step in Hydrogen Evolution Reaction is Volmer reaction: water molecule dissociation and hydrogen adsorption on the surface of the electrode. [1,5] Since water dissociation is a slow reaction, it is the rate-determining step that controls the overall speed of the hydrogen evolution reaction.[1,16]

The * in the equations indicates the catalyst surface, a chemical species shown next to this symbol represents a species adsorbed on the catalyst surface.

Volmer reaction can be represented by the following equation: [1]

$$H_2O + e^- \rightarrow H^* + OH^- \qquad \text{Volmer}$$

It follows the desorption of H_2 from cathode, that can proceed either through Heyrovsky step, an electrochemical route; or via Tafel step, a chemical pathway, which is typically the preferred mechanism. [1] The mechanism by which the H_2 desorption proceeds depends on the H* surface coverage. Heyrovsky route occurs when the H* surface coverage is low: H* interacts with a proton and an electron simultaneously, generating H_2, according to the following reaction: [1,5]

$$H_2O + e^- + H^* \rightarrow H_2 + OH^- \qquad \text{Heyrovsky}$$

On the other hand, when the H* surface coverage is high, Tafel route proceed and two adjacent H* combine, releasing H_2, as indicated in the reaction below: [1,5]

$$2\,H^* \rightarrow H_2 \qquad \text{Tafel}$$

The activity of HER decreases with pH increase: alkaline electrolytes demonstrate lower activity toward HER respect to acidic ones. Indeed, the reaction kinetics is two or three order of magnitude slower in AEMWE, compared to PEMWE. In acidic conditions, HER consists in hydrogen gas direct formation starting from protons. In contrast, in alkaline media, before H_2 can be formed, the strong covalent H-O bond in water must be broken and this requires significant energy. Additionally, OH^- can also adsorb on the catalyst, reducing the active sites available for H^+ adsorption. [5,16,24]

2.7. Oxygen Evolution Reaction in Alkaline Conditions

The kinetic of Oxygen Evolution Reaction is intrinsically slower with respect to the evolution of hydrogen, since the OER necessitates the transfer of four electrons per oxygen molecule, whereas the HER only requires two electrons for the formation of one hydrogen molecule. [16]

The reaction presents high overpotentials, due to kinetic barriers at each of the four charge-transfer steps of the reaction mechanism. [1,5] Due to its particularly sluggish kinetics, the OER will be examined in this research, with a focus on catalysts derived from non-noble metals. Initially, the possible reaction mechanisms will be briefly described to provide context.

Below are described the possible mechanisms for OER in alkaline environment. The * in the equations indicates the catalyst surface, a chemical species shown next to this symbol represents a species adsorbed on the catalyst surface. [1]

The Adsorbate Evolution Mechanism (AEM) describes the electrochemical behaviour of OER electrocatalysts based on metallic oxides or hydroxides in alkaline environments. [1,24]

The first step involves the adsorption of an OH^- anion onto the active site on catalyst's surface, forming the intermediate ∗OH and releasing one electron:

1. $* + OH^-_{(aq)} \rightarrow *OH + e^-$

Subsequently *O forms through deprotonation:

2. $*OH + OH^-_{(aq)} \rightarrow *O + H_2O + e^-$

Then the mechanism can proceed through two different ways:

3°. $*O + OH^-_{(aq)} \rightarrow *OOH + e^-$ 4°. $*OOH + OH^-_{(aq)} \rightarrow O_{2(g)} + H_2O + e^- + *$	3b. $2\,O* \rightarrow 2* + O_{2(g)} + e^-$

The Adsorbate Evolution Mechanism includes several variants, each following distinct pathways that involve the formation of intermediates such as ∗O, ∗OH, and ∗OOH, until the oxygen molecule is produced. The formation of these intermediates on catalyst's surface is crucial and represents the rate-determining step. [1,24] The variants of the AEM mechanism are listed below. [1]

1. Electrochemical oxide path:

$$* + OH^- \rightarrow *OH + e^-$$

$$*OH + OH^-_{(aq)} \rightarrow *O + H_2O + e^-$$

$$2*O \rightarrow 2* + O_{2(g)}$$

2. Oxide path:

$$* + OH^-_{(aq)} \rightarrow *OH + e^-$$

$$2*OH^- \rightarrow *O + * + H_2O$$

$$2*O \rightarrow 2* + O_{2(g)}$$

3. Krasil’ shchkov path:

$$* + OH^-_{(aq)} \rightarrow *OH + e^-$$

$$*OH + OH^-_{(aq)} \rightarrow *O^- + H_2O$$

$$*O^- \rightarrow *O + e^-$$

$$*O + *O \rightarrow 2* + O_{2(g)}$$

4. Yeager’s path:

$$* + OH^-_{(aq)} \rightarrow *OH + e^-$$

$$*^{z+1}OH \rightarrow *^{z+1}OH + * + e^-$$

$$2*^{z+1}OH + 2OH^-_{(aq)} \rightarrow 2* + 2H_2O + O_{2(g)}$$

5. Bockris path:

$$* + OH^-_{(aq)} \rightarrow *OH + e^-$$

$$*OH + OH^-_{(aq)} \rightarrow *H_2O_2 + e^-$$

$$*H_2O_2 + OH^-_{(aq)} \rightarrow *OOH^- + H_2O$$

$$*H_2O_2 + *OOH^- \rightarrow 2* + OH^-_{(aq)} + O_{2(g)}$$

For perovskites catalysts, the accepted mechanism is the Lattice Oxygen Participation Mechanism (LOM), showed below: [1]

$$OOH^* \rightarrow (V_o + OO^*) + H^* + e^-$$

$$(V_o + OO^*) + H_2O_{(l)} \rightarrow O_{2(g)} + (V_o + OH^*) + H^+ + e^-$$

$$(V_o + OH^*) + H_2O_{(l)} \rightarrow (H^*_{O\text{-site}} + OH^*) + H^+ + e^-$$

$$(H^*_{O\text{-site}} + OH^*) \rightarrow OH^* + H^+ + e^-$$

Here, V_o indicates an oxygen vacancy caused by the participation of lattice oxygen atoms in the OER.

While in the AEM mechanism, the evolved oxygen derives from water or hydroxyl ions of the electrolyte, in the LOM mechanism, the oxygen released comes directly from the catalyst's lattice, which is replaced by OH^- ions from the electrolyte.

2.8. OER Electrocatalysts

In all the proposed OER mechanisms, the catalyst's active site undergoes reactions of oxidation and reduction, reason why metals with stable and variable oxidation states can potentially be electrocatalyst for oxygen evolution reaction. Since the evolution of oxygen occurs from the oxide's surface, the mechanism by which the reactions proceed vary based on the different catalysts' structural morphology and oxide layer thickness. [1]

There are two main typology of oxygen evolution reaction electrocatalysts:

- Electrocatalysts based on noble metals: ruthenium (Ru) and iridium (Ir) based catalyst, particularly RuO_2 and IrO_2, are considered the state-of-art catalysts for OER in acidic conditions, however they lack long-term stability in alkaline pHs, so are not a feasible candidate in AEMWE. [5,24,25] Other noble metal-based catalysts comprise ruthenium (Ru), gold (Au), lead (Pb), platinum (Pt), also developed as bi-functional or tri-functional electrocatalysts. [24]

- Electrocatalysts not based on noble metals: the alkaline environment of AEMWE enables the use of a wide range of non-noble metal-based electrocatalysts, which are being developed due to their abundance and cost-effectiveness. Many non-platinum group catalysts are thermodynamically stable in solid oxide or hydroxide form at high pH and high potential and are well suited to catalyse oxygen evolution reaction. [5,6,24,25]

This thesis will investigate non-noble metal-based OER electrocatalysts for AEMWE. In particular, transition metal-based oxides are widely exploited as electrocatalyst for OER in AEMWE, for their availability, affordable costs, high activity and stable performance. They can be used as single transition metal oxides, perovskite or spinel structures. [13]

In literature, several transition metal-based electrocatalysts have been explored as potential OER catalysts, including both monometallic (e.g., Mn_2O_3, Fe_2O_3, Co_3O_4, NiO) and bimetallic compounds (e.g., $NiFe_2O_4$, $CoNiO_2$). [25]

Understanding the binding strength of the electrocatalyst's active site and the reaction intermediates is crucial to enhance the efficiency of OER. [24] Indeed, according to Sabatier principle, an efficient catalyst should have a moderate bonding strength with the adsorbed

intermediates. The bonding must not be too weak to impede intermediate bonding; nor too strong, which would hinder the desorption of intermediates once the reaction occurred. [1] To assess whether a catalyst is suitable to catalyse the reaction, volcano plots are commonly used as they provide valuable insights into the relationship between catalytic activity and the enthalpy of adsorption of reaction intermediates, that is the quantity of energy released when the intermediates of the reaction bond to the catalyst surface. [1]

The figure below presents a volcano plot. The Y-axis represents the overpotential value (mV), which is an indicator of the rate of oxygen production, while the X-axis shows the enthalpy change (kg/mol) in acidic (black square) and alkaline (white square) solutions. [1]

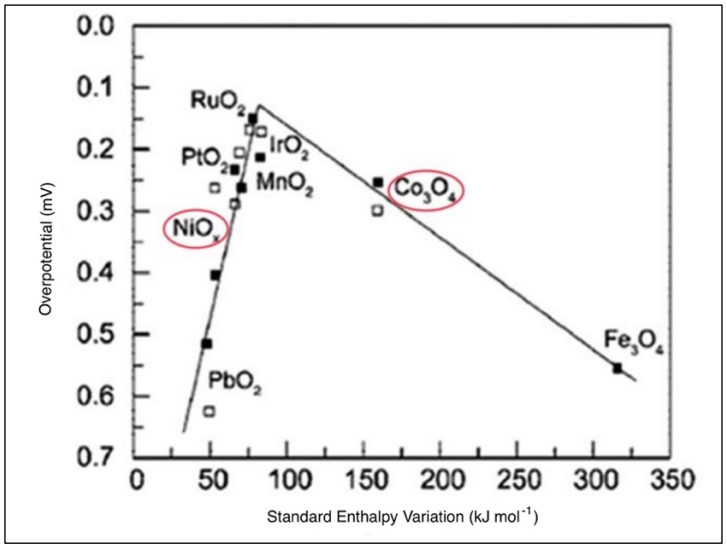

***Figure 11**: Volcano plot that relates overpotential values with enthalpy change for transition metal oxides. Adapted from reference [1].*

The plot highlights a "volcano relationship": compounds with intermediate values of -ΔH° shows lower overpotential values, which in turn implies a higher catalytic activity. [1]

Metal oxides of ruthenium and iridium are on the top of the plot, with an intermediate -ΔH°, that allows an efficient OER catalytic activity, due to their excellent electrical conductivity and low redox potential. Despite RuO_2 and IrO_2 are the best electrocatalysts in terms of overpotential, Ir and Ru are noble metals, implying high costs and rarity. For this reason, researchers are focusing on developing catalysts using more available and affordable materials. As shown by the plot, compounds like manganese, nickel or cobalt oxides are less efficient than ruthenium or iridium-based catalyst, but could offer a compromise between catalytic activity, costs and availability. In contrast, Fe_3O_4 has an excessively high -ΔH°, which prevents the

release of reaction intermediates, while PbO_2 has an excessively low -ΔH°, which impedes its ability to bind them. [1]

The limited OER catalytic activity of manganese-based compounds has previously been documented. Particularly, Mian Li et al. (2015) reported that an increase in manganese content within ferrous oxides results in higher overpotentials for OER compared to the incorporation of metals such as cobalt, nickel, or copper. This is likely due to the low electrical conductivity and the presence of different structural phases that can reduce the exposure of catalytic sites. [25,26]

Similarly, Fe_2O_3 has been associated with poor OER activity, due to its low electronic conductivity, which limits the electrons transfer during the reaction; and non-optimal binding strength with reaction intermediates, as shown in volcano plot in figure 11. [1,25] Despite this, Naiying Du et al. (2022) reported that iron-based (oxy)hydroxides, FeO_xH_y, demonstrated the highest turnover frequency (TOF) compared to other monometallic (oxy)hydroxides, following the order FeO_xH_y > CoO_xH_y > NiO_xH_y > MnO_xH_y, as shown from graph below (figure 12), representing OER activity of different (oxy)hydroxide electrocatalysts. On Y axis, it is represented the overpotential value in mV, while the X axis shows the turnover frequency (TOF) in s^{-1}, the latter is the number of molecules produced per single active site per unit time, representing the speed with which a catalytic site generates oxygen per unit time, a higher value indicates a higher catalytic activity. [5]

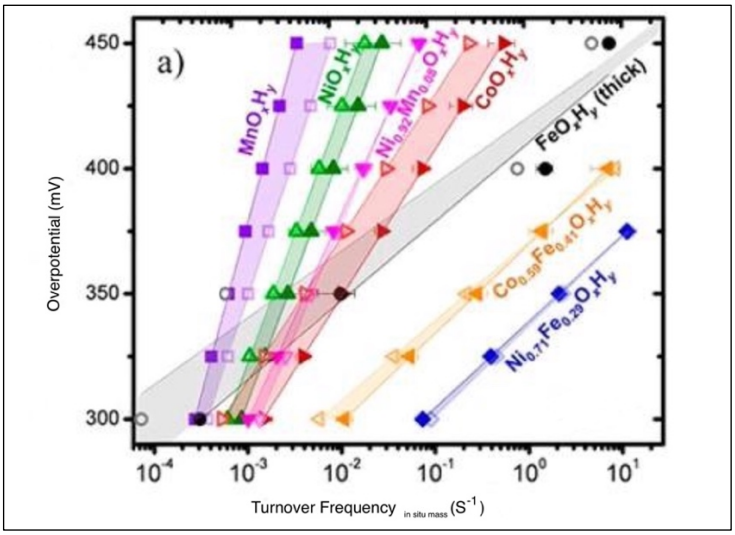

***Figure 12**: Plot that relates turnover frequency (TOF) with overpotential values (η) of different (oxy)hydroxide based electrocatalysts. Adapted from reference [5].*

It results that, when its poor electrical conductivity is mitigated, iron can show promising OER catalytic activity. In particular, the incorporation of iron into nickel- or cobalt-based electrocatalysts has been reported to enhance performance. [23] Indeed, iron containing catalysts show lower overpotential values and higher TOF values, compared to single-metal oxides, with $Ni_{0,71}Fe_{0,29}O_xH_y$ demonstrating the best performance, followed by $Co_{0,59}Fe_{0,41}O_xH_y$. [5,25]

One of the challenges related to noble metal free catalyst is the optimization of chemical compositions, activity and stability of the metal. These catalysts usually present lower conductivity respect to noble metals, which results in lower mass specific activity, that often necessitates a higher catalyst loading, which in turn can increase potential losses associated to ohmic resistance. [16]

Electrocatalysts containing two or more metal oxides were developed to increase OER activity:

- Perovskite oxides have a cubic crystal symmetry and a composition of ABO_3, in which the tetrahedral site is occupied by a rare earth element or an alkali earth metal (A), while a transition metal occupies the octahedral site (B). They have a unique 3d electronic structure and a tuneable composition, that allows to change the structure and the electronic states to enhance the activity and durability. However, they have yet to been implemented into real AEMWE systems. [13]

- Spinel structures have a composition of AB_2O_4, in which A is the transition metal in a divalent oxidation state occupying the tetrahedral site, B is the transition metal in a trivalent oxidation state occupying the octahedral site. These structures were developed because of their high electrocatalytic activity, charge transfer performance and stability in alkaline environments. Enhancement in OER activity can be achieved by changing the electronic states through selecting different metals, varying the A and B combinations, and modifying the oxygen content at the sites. [13,27]

Nickel-based and cobalt-based catalysts will be discussed, as they were analysed in this thesis.

2.8.1. Nickel based electrocatalysts

Nickel is an abundant and non-noble metal-based material already used in traditional alkaline water electrolysis as OER and HER catalysts, these conditions make it an unexpensive and easily available candidate to replace noble-metal based electrocatalysts. [5]

Pourbaix diagrams can provide insights on the stability of the material as function of pH and voltage. However, they are only based on thermodynamic considerations, without taking into account the kinetics, the particle sizes and the morphologies of the catalyst. For these reasons, experimental testing in a real electrochemical cell is essential to assess the actual stability of the catalyst under operative conditions. Pourbaix diagram for Nickel is presented below. [5]

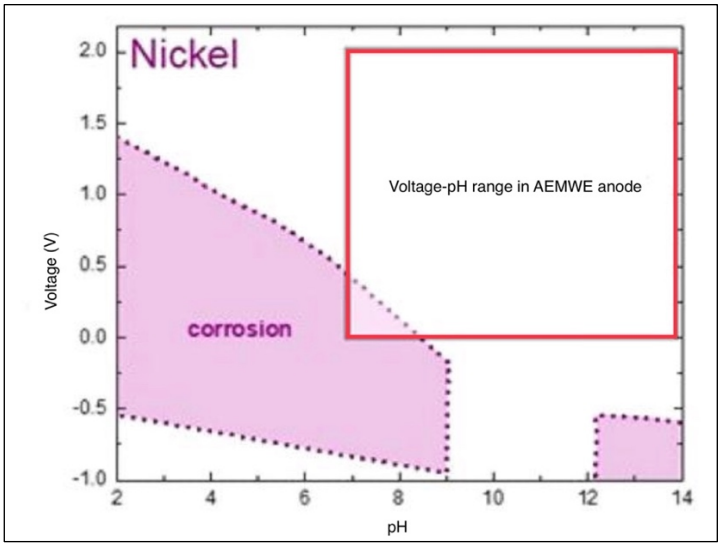

Figure 13: *Pourbaix diagram for nickel in aqueous electrolytes at ambient pressure and 25 °C. Adapted from reference [5].*

The coloured portion of the graph is the pH and voltage range in which the material is corroded, while the white rectangular box represents the typical operating conditions for water electrolysis. In particular, the pH range for AEMWE, which includes diluted KOH or NaOH electrolyte, is between 9 and 12. [5]

Nickel based oxide/(oxy)hydroxide have been widely used as OER electrocatalysts. Indeed, NiO, with a simple and symmetric ionic structure, is known to show long-term stability under alkaline pH and high-voltage conditions. [5,28]

Since nickel-based catalysts on their own typically demonstrate low catalytic activity for the evolution of oxygen, iron-nickel based electrocatalysts were developed. Iron was incorporated

in the nickel oxide lattice, easily replacing some nickel atoms in the oxide/(oxy)hydroxide lattice, due to the similarity of the two elements, presenting an atomic number of 28 for Fe and 26 for Ni. The resulting $NiFe_2O_4$ catalyst has a spinel crystal structure, in which oxygen ions form a face-centred cubic lattice, and the cations, Ni^{2+} and Fe^{3+}, occupy tetrahedral and octahedral interstitial sites. [5,16] Previous studies reported that iron-nickel oxides demonstrate elevated performances compared to the monometallic nickel or iron oxides, due to the synergy between the two elements, [25] with the presence of iron significantly increasing OER activity and facilitating the formation of high surface area structures. Because iron is present in trivalent form, while nickel in divalent configuration, the substitution creates a change in overall charge, compensated by anions and water molecules intercalation, with the creation of a layered high-surface area structures, facilitating ions transport. [5,16]

However, Emily K. Volk et al. (2023) reported overpotential values of $NiFe_2O_4$ similar to those of NiO, at comparable exchanged current densities, contradicting previous studies. Notably, their study utilized an iron concentration higher than the commonly referenced value. [25] Indeed, it has been previously reported that in NiO_xH_y catalysts, the optimal OER activity is achieved when the iron atomic concentration is between 5% and 10%, and it remains stable up to 30-50%. Beyond this range, Fe forms Fe_2O_3, that transitions to the unstable FeOOH form, reducing the effectiveness of iron incorporation. [5] The graph below presents Emily K. Volk et al. (2023) results, comparing the performance of different OER electrocatalysts, showing overpotential (mV) on the Y-axis and current density (mA/cm^2) on the X-axis. [25]

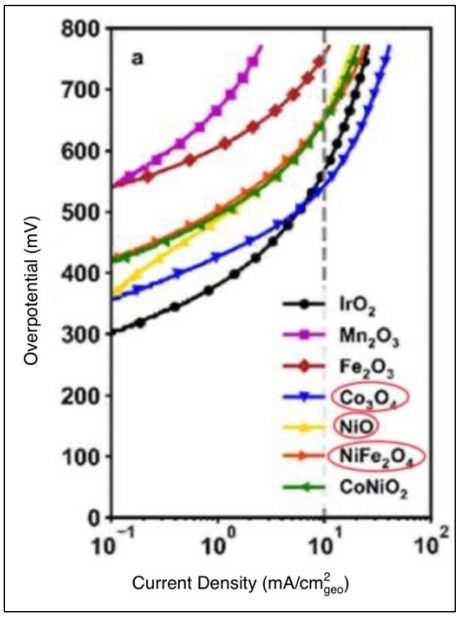

Figure 14: *Tafel plots of different electrocatalysts. Current densities normalized by geometric surface area. Adapted from reference [25].*

Notably, NiO and $NiFe_2O_4$ demonstrated similar overpotential values, suggesting that incorporation of higher concentration of iron to nickel oxide did not increase the catalytic activity. Moreover, as expected based on previous analysis, Mn_2O_3, Fe_2O_3 showed the highest overpotentials value, higher than 500mV, already at relatively low current densities. This outcome highlights their limited application as OER electrocatalysts, consistent with previous studies. [25]

Beside Ni_xFe_y alloys, also Ni-based alloys containing aluminium and molybdenum have been developed, however in alkaline and high potential conditions, there are stability issues. [5]

2.8.2. Cobalt based electrocatalysts

Cobalt containing electrocatalysts have been reported to have high performance towards oxygen evolution reaction, mostly attributed to high electrical conductivity, high mobile oxygen vacancies, and multiple oxidation states in the spinel structure. [25]

Cobalt Oxide (Co_3O_4) is a spinel-structured oxide, with the cobalt occupying both the tetrahedral and octahedral site: A-sites are typically occupied by divalent cobalt (Co^{2+}) and B-sites by trivalent cobalt (Co^{3+}). [13]

Cobalt demonstrates stability in alkaline environments and in the operative voltage of water electrolysis, as showed by the Pourbaix diagram below.

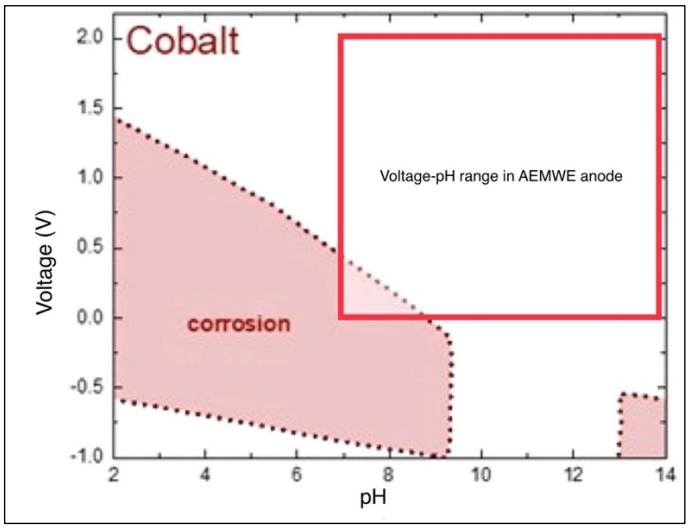

Figure 15: *Pourbaix diagram for cobalt, in aqueous electrolytes at ambient pressure and 25 °C. Adapted from reference [5].*

The coloured portion of the graph is the pH and voltage range in which the material is corroded, while the white rectangular box represents the typical operating conditions for water electrolysis. In particular, the pH range for AEMWE, which includes diluted KOH or NaOH electrolyte, is between 9 and 12. [5]

However, challenges related to long-term stability under operative conditions, have been reported. A study performed by Emily K. Volk et al. (2023) highlighted that Co_3O_4 shows a significant decrease in activity during operation conditions, with deactivation percentages ranging from 45% to 71%. When the measured current was normalized by the double-layer capacitance, which is a measure of the electrochemical surface area, the deactivation percentages range between 29% and 54%, suggesting that part of the deactivation is likely due to a loss of active surface area. The loss in active surface can be due to the catalyst detachment from the substrate, which reduces the number of active sites; the dissolution of cobalt ions in the electrolyte; the formation of additional oxide layer on the catalyst's surface, that can potentially passivate the active site and lead to particles agglomerations. [25]

These findings indicates that also in this case, the stability of cobalt-containing catalysts must be assessed experimentally under practical operative conditions, in order to include kinetics and morphological factors.

The spinel's catalytic activity can be further improved by substituting some elements (such as Ni, Mn, Fe, Cu, and Li) in the sites. [13] Indeed, similarly to the nickel-based catalyst, iron, at atomic concentrations ranging from 40% to 60%, can be incorporated into the cobalt lattice, increasing OER activity. However, the incorporation occurs at a slower rate compared to nickel-based alloys. Additionally, adding high concentrations of iron can reduce the electronic conductivity, due to the formation of less conductive iron oxides. [5]

2.9. Materials and Components of an AEMWE

The figure below illustrates a schematic representation of a single-cell configuration of an AEM water electrolyzer.

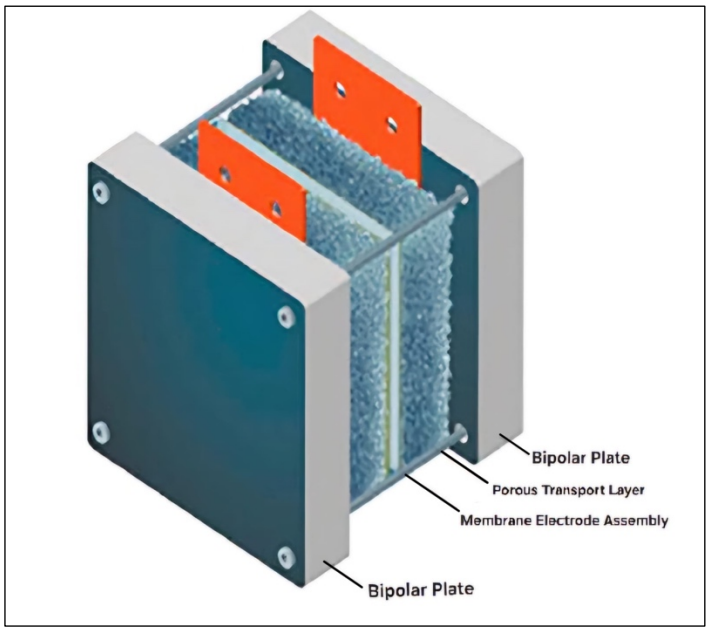

***Figure 16**: Schematic representation of single-cell configuration. Adapted from reference [5].*

In industrial scale electrolyzers, multiple such units are stacked and electrically connected in series to form an electrolyzer stack. The total voltage is the sum of the individual cell voltages, while the current density is constant across all cells.

This configuration relies on several key components, each with a specific role in the electrolysis reaction:

- Frames facilitate the diffusion of products and the supply of reactants to the electrodes, ensuring a uniform distribution.

- Bipolar plates are flat separators that ensure electrical contact between adjacent cells in the stack, connecting the anode of one cell to the cathode of the adjacent one. They are used to match the power supply voltage by stacking multiple electrolysis cell units in series.

- Porous transport layer (PTL) or gas diffusion layer (GDL): serves to the transfer of the electrolyte to the reaction site and the release of generated gases from the reaction zone. Additionally, the PTL provides mechanical support to the membrane [13].

- Anodic and cathodic electrocatalysts are where the reduction and oxidation reactions occur, respectively.

- Anion Exchange Membrane (AEM) allows anion exchange and separates anode from cathode.

The combination of porous transport layer, catalysts layer and anion exchange membrane compose the Membrane Electrode Assembly (MEA), which is the core of the electrolyzer. [29]

The alkaline conditions of AEMWE allow to use less expensive materials for stack components, respect to titanium or platinum employed in PEMWE systems. In particular, bipolar plates are commonly composed of stainless steel, graphite, or nickel, while porous transport layers are made of porous nickel, porous stainless steel, or porous graphite. [16]

2.9.1. Anion Exchange Membrane (AEM)

The membrane is responsible for anions exchange, allowing the passage of OH^- required for the reactions. This role is supported by the electrolyte, that provides the anions. Moreover, the membrane allows the separation between anode and cathode. [13]

Similarly to PEMWE, also in AEMWE, a dense polymeric membrane is used, namely an anion exchange membrane. [17] However, unlike PEM, this membrane allows the passage of hydroxyl ions (OH^-), rather than protons (H^+), transporting them from cathode to anode. Moreover, it avoids the passage of electrons and gasses produced by water electrolysis. [6]

AEM are composed by anion exchange polymers: a polymeric backbone with cationic headgroups anchored to it. [5]

Both components determine the chemical stability of the membrane, while the polymeric backbone, generally composed by polysulfone (PSF) or polystyrene crosslinked with divinylbenzene, is responsible for mechanical and thermal stability [6]

Cationic headgroups, attached to the polymeric chain, are accountable for ionic transport properties, such as ion exchange capacity, ionic conductivity, and transport number. [5,6] These

groups serve as exchange sites for hydroxide anions (OH^-) and many of them contain nitrogen-based functional units. [5]

Notable groups include:

- Quaternary ammonium functional groups [5]
- Imidazolium cation [5,17]
- Benzimidazolium cation [5,17]
- Guanidinium [5]
- Pyridinium [5]
- Tertiary diamines [5]
- Sterically shielded phosphonium and sulphonium head-groups [5]
- Ligand metal complexes [5]

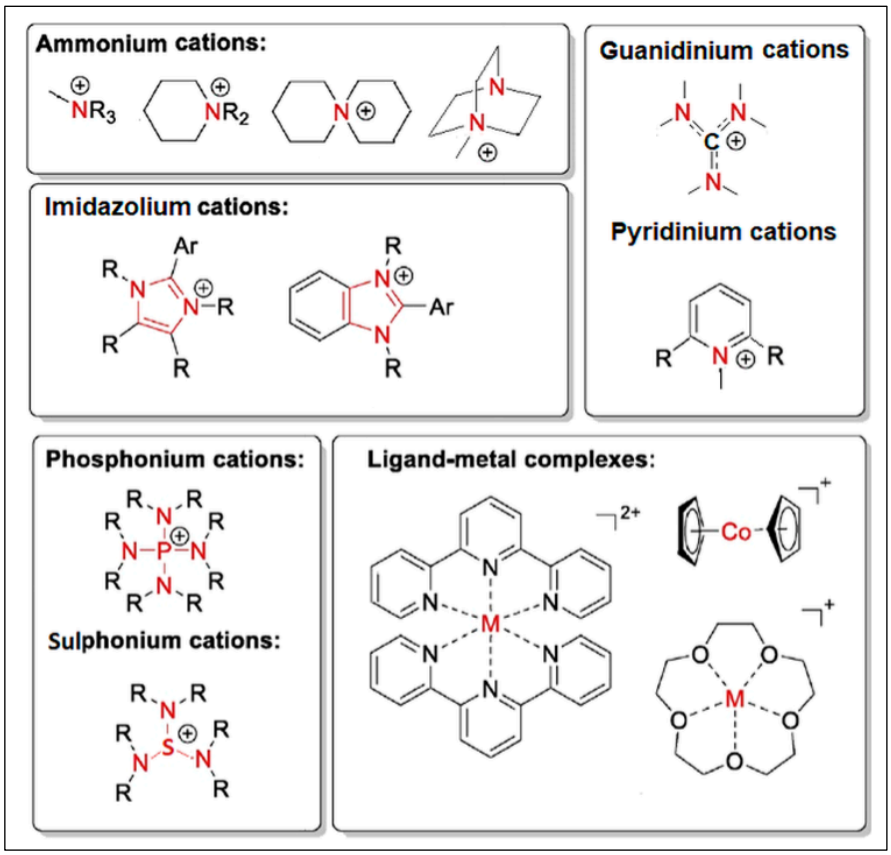

***Figure 17**: Structures of different types of cations used in anion exchange membranes.[5]*

One of the main challenges of AEM electrolyzers is to synthesize an anion exchange membrane with mechanical stability and ionic conductivity both high. [6]

The conductivity of the membrane is a crucial parameter, since it affects the efficiency and voltage required to sustain the desired current density. [6] An increase of ion exchange groups could increase conductivity, since more groups allows more ions to move through the membrane. However, this also increases water uptake and consequently compromise mechanical strength. [6] Moreover, to minimize the internal cell resistance, membrane's thin structure is essential. [23]

The stability of the membrane is a critical parameter in determining its suitability for use AEMWE: if the membrane is not sufficiently stable, it may degrade over time, leading to an increased gas crossover between the anode and the cathode, that will determine a decrease in the purity of H_2 produced and a reduced efficient of the whole system. The membrane's stability can be assessed by monitoring voltage while maintaining constant current density, an increased voltage suggests instability, possibly due to polymer or ion exchange group degradation. [6]

Currently, the stability of the polymeric chain and cationic functional groups limits the long-term application of anion exchange electrolyzers. [17] In particular, many anion exchange membranes break down at moderate temperature, such as 60°C. [5]

Previous studies identified various degradation mechanisms, listed below: [5]

1. Nucleophilic substitution (SN2) benzyl substitution,
2. Nucleophilic substitution (SN2) methyl substitution,
3. β-elimination substitution,
4. Ylide intermediated rearrangements,
5. SN2 Ar aryl ether cleavage in the polymeric backbone,
6. Ring opening of imidazolium,
7. SN2 methyl substitution in imidazolium,
8. Heterocycle deprotonation of imidazolium,
9. SN2 and ring opening of piperidinium, pyrrolidinium, and morpholinium,

10. Ring opening of N-spirocyclic ammonium,
11. Dehydrofluorination of the polymer backbone,
12. Nucleophilic addition and displacement in pyridinium,
13. Nucleophilic degradation of guanidinium.

Quaternary amines and imidazolium groups are particularly susceptible to degradation in alkaline environment. The most common degradation mechanisms include Hofmann degradation, SN2, or ring-opening reaction. High temperatures accelerate the rate of degradation. [5]

2.9.2. Catalyst Deposition in Membrane Electrode Assembly (MEA) Production

Anodic and cathodic electrodes are where the electrochemical reactions occur. In particular, the formation of oxygen takes place at anode during Oxygen Evolution Reaction (OER), while hydrogen is produced at cathode through Hydrogen Evolution Reaction (HER). To enhance the efficiency of the reactions and reduce overpotentials, catalyst layers are employed on electrodes or on membrane. [13]

To develop a MEA, the catalysts required to drive the reactions, can be applied either on the membrane or on a support. [20]

The Catalyst Coated Membrane (CCM) manufacturing foresees the application of the catalytic layer on the membrane. The preparation of the CCM-MEA mainly foresees the spray coating of a catalytic ink on the membrane. Another technique, addressed as doctor blade method, can be implemented, which foresees the application of catalytic ink with a blade positioned at a specific distance from the substrate, where the distance determines the thickness of the deposited layer. However, typically better results are achieved with the spray coating technique, which results in a precise control of the loading and a low resistivity. The main advantage of CCM is that the catalyst is in close proximity with the membrane, this improves ionic conductivity, enabling a lower catalyst loading. Despite this, electrical contact between current collectors is less effective. [16]

In the Catalyst Coated Substrate (CCS) fabrication, the catalyst is deposited on a support, specifically the PTL. [20] The substrate coating process mainly involves a wet route, where the

catalytic ink is deposited on the PTL through spraying or painting. To reduce the large use of solvents associated with these techniques, thin-film deposition methods are being explored, including chemical vapor deposition, atomic layer deposition, ion beam sputtering deposition, magnetron sputtering. [5,16] The supporting substrate, despite providing mechanical support to the catalyst, resulting in a stable catalytic layer, also enables electron transfer and guarantees the efficient removal of produced gasses. [16]

Several materials could potentially be used as substrate: Ti paper, platinized Ti plates, stainless steel felt, Ni felt, Ni foam, carbon paper, carbon cloth. However, titanium is excluded since it is expensive and more affordable materials can be used in alkaline conditions, while carbon materials do not have long-term stability under alkaline conditions. Moreover, stainless steel passivates at anodic potential in alkaline conditions, this ensures stability but reduces electrical conductivity at the interface between the electrolyte and the electrode. The standard material used for the PTL in AEMWE is nickel, which can be in form of nickel felt or nickel foam. [16]

In this thesis, nickel felts have been utilized as both the anode and cathode material, with catalysts deposited on its surface following the CCS methodology. Further details are provided in paragraph 3.2.

The figure below presents a representation of the catalyst coated substrate setup.

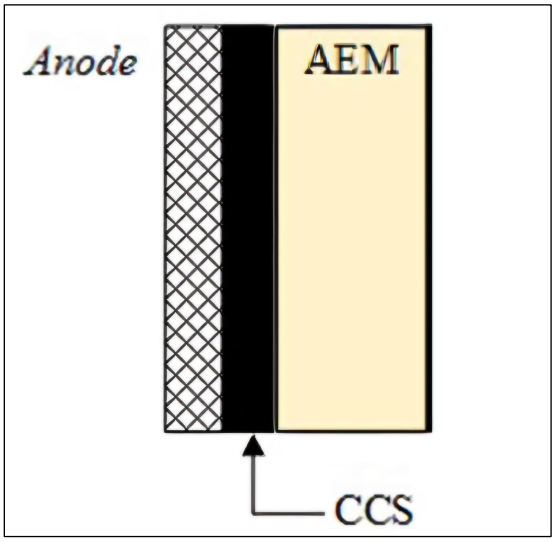

Figure 18: *Representation of CCS. Adapted from reference [20].*

3. Experimental

During this research, MEA design included the use of commercially available materials, which have been processed through steps such as: membrane treatment, catalysts ink formulation and deposition on nickel felt PTL and electrodes thermal treatment.

The anodic catalysts selected for this thesis were Nickel Oxide (NiO), Nickel Iron Oxide ($NiFe_2O_4$) and Cobalt Oxide (Co_3O_4). The average particle's sizes of the commercially available powders, declared from the suppliers, are showed in table below.

Co_3O_4	15nm
NiO	18nm
$NiFe_2O_4$	20nm

Table 4: *Average particle's sizes of commercially available catalytic powders.*

The cathodic catalyst employed, necessary to complete the MEA and enable tests in the electrochemical cell, was Platinum on Carbon (Pt/C).

3.1. Formulation of Catalytic Inks

A crucial step in the preparation of electrocatalysts is the formulation of catalytic inks, which employs commercially available catalytic powders. The typical catalytic ink preparation process for AEMWE foresees a wet route, in which the nanostructured catalytic powder is mixed with appropriate concentrations of solvents and ionomer. [5] However, the specific formulation of the catalytic ink used in this study will not be specified to protect the company's confidentiality.

The small particles size of the catalyst is crucial to achieve a homogeneous distribution in the solvent, since smaller particles with higher surface area disperse better. A homogeneous mixing of the catalytic inks positively influences the quality of the deposition on the nickel felt support, generating a uniform catalytic layer, important for maximizing the electrochemical performance. Moreover, smaller particle sizes positively influence catalytic activity due to the higher surface/volume ratio, which results in more atoms exposed to the surface and consequently more active sites available for the reaction.

Solvents are of extreme importance since they ensure the solubilization of the ionomer and a proper dispersion of catalyst powders, to avoid particles agglomeration which would cause a non-homogeneous catalyst deposition. During the catalytic ink deposition, the solvents evaporate, promoting the catalyst particles adhesion to the support and facilitating the formation of pores. The porosity is essential to minimize mass transport limitations and ensure efficient diffusion of reactants and products, moreover, a porous structure provides a higher surface area with more exposed active sites, enhancing the catalytic activity. Commonly used solvents include deionized water, isopropyl alcohol, ethanol, acetone. Often, these solvents are used in combination to balance their chemical properties. [5]

The Anion Exchange Ionomer (AEI) acts as a binder, providing mechanical stability to the catalytic layer. It has been reported that the ideal ionomer loading ranges between 5% and 20% by weight, however the exact value must be determined experimentally. The ionomer is typically chemically similar to the membrane, which results in a reduced interfacial resistance and a comparable swelling ratio, that helps prevent the catalyst detachment. [5] In this study, the ionomer was selected based on its compatibility with the chosen membrane, the specific composition of both the AEM and the AEI are not specified to protect the company's confidentiality. The figure below shows the ionomeric solution, consisting of ionomer dispersed in solvents, the specific quantities are not specified to preserve corporate confidentiality.

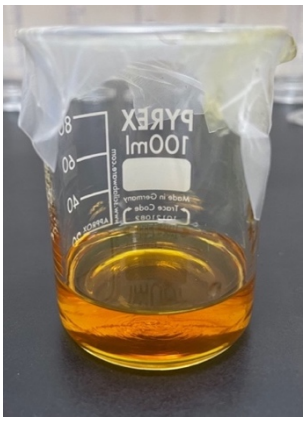

Figure 19: *Ionomeric solution.*

The ionomeric solution is combined with the catalyst powder and additional amounts of solvents, then mixed using mechanical stirrers to produce the inks.

The catalytic inks are stabilized through a sonicator, a technology that employ high-frequency ultrasonic waves to break eventual agglomerates. In this way, a uniform dispersion of the catalyst particles within the solution can be achieved.

The following images illustrate the catalytic inks of the anodic catalysts $NiFe_2O_4$, Co_3O_4, NiO.

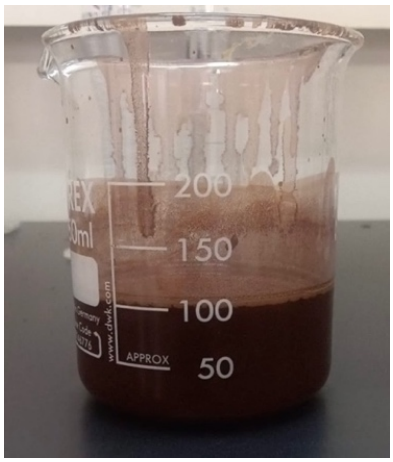

***Figure 20**: $NiFe_2O_4$ catalyst ink.*

***Figure 21**: Co_3O_4 catalytic ink.*

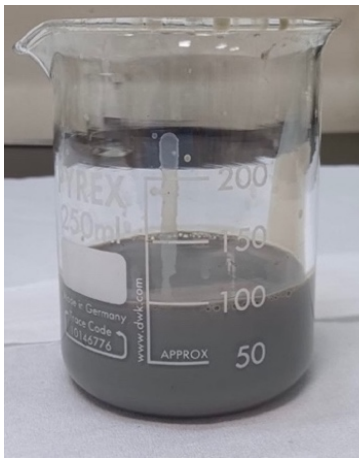

***Figure 22**: NiO catalytic ink.*

3.2. Inks Deposition

The stabilized catalytic inks have been deposited on circular nickel felts, using the CCS methodology and following a specific deposition pattern in line with the industrial practices of Arco Technologies S.r.l. The catalyst loading for each CCS electrode was determined in collaboration with the company, based on an analysis of the literature, and will not be specified to protect the company's confidentiality. The heated plate is set to 90°C to promote solvents evaporation.

The image below shows the prepared deposition plan, with the supporting nickel felt on top, onto which the catalytic inks have been deposited.

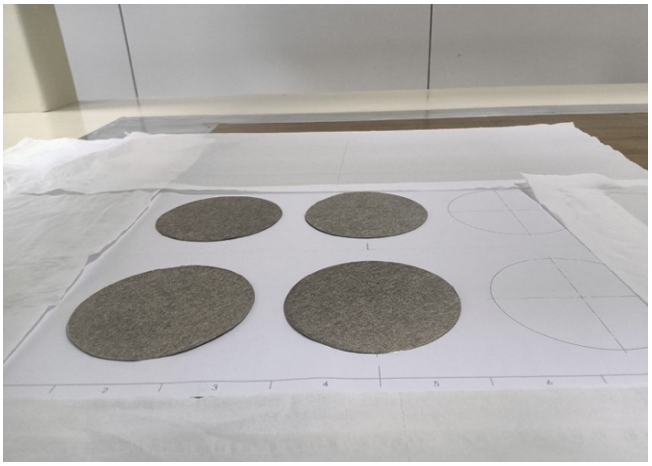

***Figure 23**: Deposition pattern of electrodes with Ni felt above.*

The figure below illustrates the nickel felts with the anodic catalytic inks deposited on the surfaces.

***Figure 24**: $NiFe_2O_4$ electrode.*

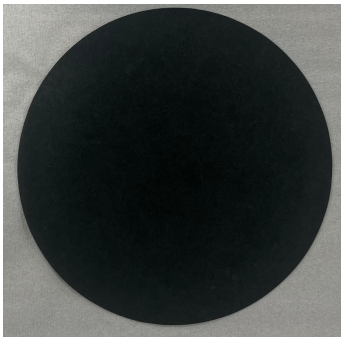

***Figure 25**: Co_3O_4 electrode.*

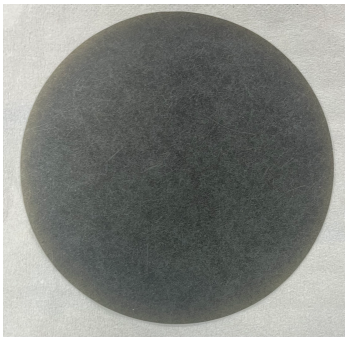

***Figure 26**: NiO electrode.*

3.3. Anion Exchange Membrane (AEM) Pretreatments

The commercially available anion exchange membrane is supplied from the producer in the dry chloride/iodide form, a stable form for transport and storage, but it is not the operative form. Hence, the membrane has been subjected to pretreatments, necessary to substitute iodide ions, since the initial quantity of iodine can negatively influence its efficiency and durability. Initially, the membrane, in its dry state, was placed in an excess salt solution of NaCl (3M) for 4 hours at a temperature of 50°C to facilitate the substitution of iodide anions with chloride anions and to hydrate the membrane gradually. Subsequently, the membrane was immersed in a 1M KOH solution for 24 hours to convert it into its hydroxide form, the operative form for alkaline water electrolysis.

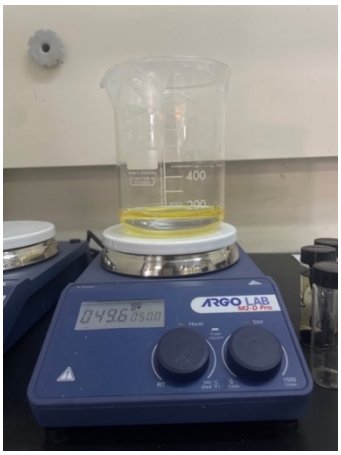

***Figure 27**: AEM in 3M NaCl solution at 50°C.*

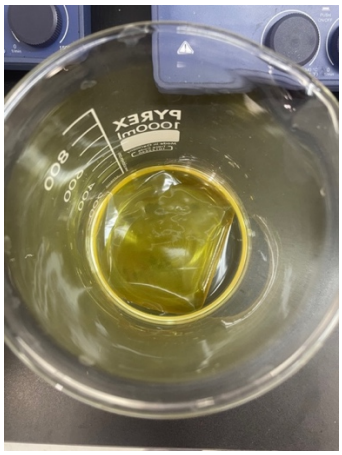

***Figure 28:** AEM in 1M KOH solution.*

3.4. Electrodes Treatments

Heat treatments are of extreme importance during the synthesis of electrocatalysts: the temperature has an influence on the morphology of the catalyst's surface, particles size, active centre. Indeed, it is reported that thermal treatments enhance both the catalytic activity and the stability of electrocatalysts: treated electrodes showed improved performance, including increase in current densities and improved charge transfer. These improvements are associated to a reduction in catalyst particle sizes and enhanced morphology resulting from the temperature increase. Moreover, the heat treatment makes evaporate any contamination of previous preparation steps and ensures a uniform dispersion of the catalyst on the support. [30]

Different methods are available to perform the treatment, including stove heating, which is the most widely applied technology, but there are also more advanced techniques, such as microwave heat treatment, plasma heat treatment, ultrasonic spray pyrolysis. [30]

Despite the approach of thermally treating catalyst powders during synthesis is well-explored and applied to improve catalytic properties, research on thermal treatments on CCS deposited electrodes remains limited. One problem is the mechanical stability associated with the ionomer, that decreases when high temperatures are applied. However, it could be mitigated through the insertion of PTFE thin films, which improve the mechanical strength and stability of the ionomer. [31]

During this thesis, heat treatments have been performed directly on the CCS electrodes. The anodic electrocatalysts, specifically $NiFe_2O_4$, NiO, Co_3O_4, along with the cathodic Pt/C, have been subjected thermal treatments of 2 hours in an oven. In particular, a $NiFe_2O_4$ sample has been heated for 2 hours at high temperatures of 350°C circa. Then, another $NiFe_2O_4$ sample has been processed for 2 hours at lower temperatures, specifically 120°C. The sample treated at 350°C was analysed through SEM/EDS, XRD and electrochemically tested, results were compared with those treated at 120°C. Based on considerations from the SEM analysis discussed in paragraph 4.1.5, NiO and Co_3O_4 were subjected exclusively to the lower temperature treatment at 120°C.

The figure below shows an example of the thermal treatment of the electrodes conducted in an oven.

Figure 29: *Electrodes' thermal treatment.*

3.5. Electrochemical Characterizations in AEMWE Test Station

The CCS-deposited MEA have been tested using a single-cell configuration in an electrochemical AEMWE test station, under the following operative conditions:

Cathodic electrocatalyst	Pt/C
Anodic electrocatalysts	$NiFe_2O_4$ NiO Co_3O_4
Electrode active area	64 cm^2
Electrolyte	1M KOH
Pressure	Atmospheric
Temperature	60°C
Operative current density	0,6 A/cm^2

Table 5: *Parameters for tests in electrochemical cell.*

The constant current density applied to the system was selected based on the hydrogen production requirements of the company.

The electrolyte is introduced at the anode side, where OH^- ions are consumed in the electrochemical reaction. By supplying the electrolyte directly to the anode, a sufficient concentration of OH^- ions is ensured, which is essential to sustain the reaction efficiently.

The MEA is assembled by pressing together the previously prepared components, directly in the cell hardware. The hot-press assembly, commonly used in PEMWE configurations, cannot be used in AEMWE systems, since the nickel felts would damage the membrane in those conditions of temperatures and pressures. [16]

The image below shows an assembled electrochemical cell. The port labelled "in" is the entry point of the electrolyte, while the one labelled "out" is where the electrolyte exits, along with oxygen. Hydrogen exits through the separate, unlabelled port. Tubes are connected to allow the entering of the electrolyte and collect the exiting substances.

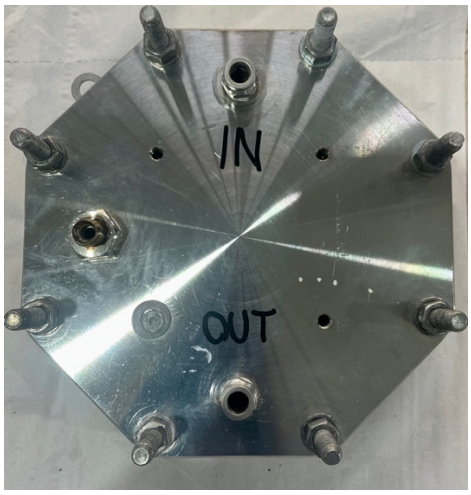

***Figure 30**: Assembled cell.*

4. Results and Discussion

This thesis focused on the development and investigation of different CCS anodic electrodes for AEMWE based on different catalytic compositions: $NiFe_2O_4$, NiO, Co_3O_4. The process involved the preparation of catalyst inks, their deposition on nickel felt substrates, thermal treatments on electrodes and subsequent characterizations. Morphological and structural properties were investigated using SEM/EDS and XRD analyses. Moreover, all the anodic electrocatalysts were subjected to individual electrochemical testing in a single-cell configuration, with a Pt/C cathode, to evaluate and compare their catalytic performances and stability.

4.1. Scanning Electron Microscopy (SEM) Analysis

Scanning electron microscopy (SEM) is an effective tool to analyse organic and inorganic solid samples on a nanometre to micrometre scale. It is often coupled with energy dispersive X-ray spectroscopy (EDS) that provides qualitative and semi-quantitative analysis on elements present in the sample. The working principle of SEM analysis relies on a high energy electrons beam, generated by a heat source, interacting with the atoms of the sample to provide information about the surface and the composition of the specimen. Electromagnetic lenses are then employed to reduce the spot size, which would otherwise be too large to produce a well-defined image. The movement of the scan coil directs the electrons beam to different areas of the sample; in this way an image is formed point by point. Then, specific detectors will record the electrons emitted by the sample. [32]

Based on the voltage of the electrons beam, the resulting image is different. To obtain surface information, low accelerating voltage of less than 5kV are used. However, higher accelerating voltage ranging between 15 and 30kV are employed to penetrate deeper into the structure of the sample, which is relevant to this study. [32]

Whitin this research, scanning electron microscopy/energy dispersive spectroscopy (SEM/EDS) analyses were carried out using an E-SEM Zeiss EVO 50 Series Instrument (Carl Zeiss s.p.a. Milan, Italy) equipped with an INCA Energy 350 EDS micro analysis system (Oxford Instruments Analytical, Abingdon, UK). The accelerating voltage was 20 kV and the spectra collection time 60 s.

The catalyst analysed through Scanning Electron Microscopy was the $NiFe_2O_4$, with a focus on evaluating the potential of thermal treatments to modify its catalytic properties. The analysis was performed on both $NiFe_2O_4$-coated and uncoated side of the electrodes, which were subjected to 350°C, 120°C, and no thermal treatment. The analytical objective was to verify the uniformity of the surface of the unheated samples, checking whether the deposition of the catalysts is homogeneous, and compare the results with the thermal treated samples to highlight any morphological changes on electrodes and evaluate the effects of the thermal treatments.

Elemental mapping was carried out through Energy Dispersive Spectroscopy (EDS) on the same samples to have an estimated measure of the elements present in the samples, compare their compositions and evaluate the effects of the thermal treatments, such as materials degradation or impurities removal.

4.1.1. Untreated Nickel Felt

The untreated nickel felt support has been analysed with SEM technology on the side where no catalyst was deposited, in order to characterize its surface morphology and compare it with the $NiFe_2O_4$ coated side and heat-treated samples. SEM images are showed below.

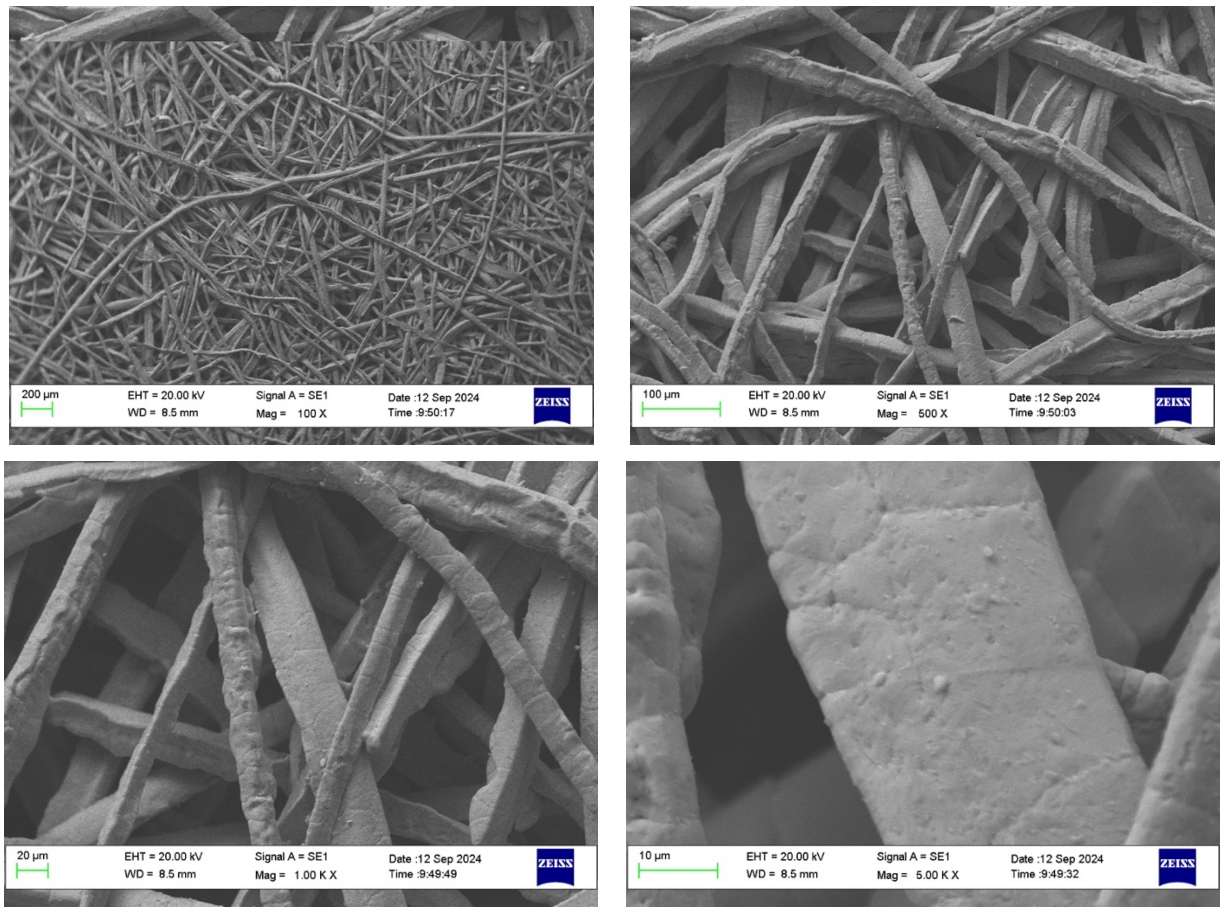

***Figure 31**: SEM image of untreated nickel felt, captured at 100X, 500X, 1,00 KX, 5,00KX magnification.*

The analysis of SEM images of the untreated nickel felt reveals a visible fibrous structure, with a random distribution of fibres characterized by a rough surface. The randomness of the fibres creates a network-like structure that increases the porosity, enhancing the surface area available for the deposition of the catalyst, while the irregular surface can improve the catalyst adhesion to the support.

The combination of the randomness of the fibres and the rough texture promotes a homogeneous catalyst deposition on the nickel felt support, crucial for the performance of the electrode.

The following plot presents the EDS spectrum of the untreated nickel felt sample, and the subsequent table provides the percentages of its elemental composition.

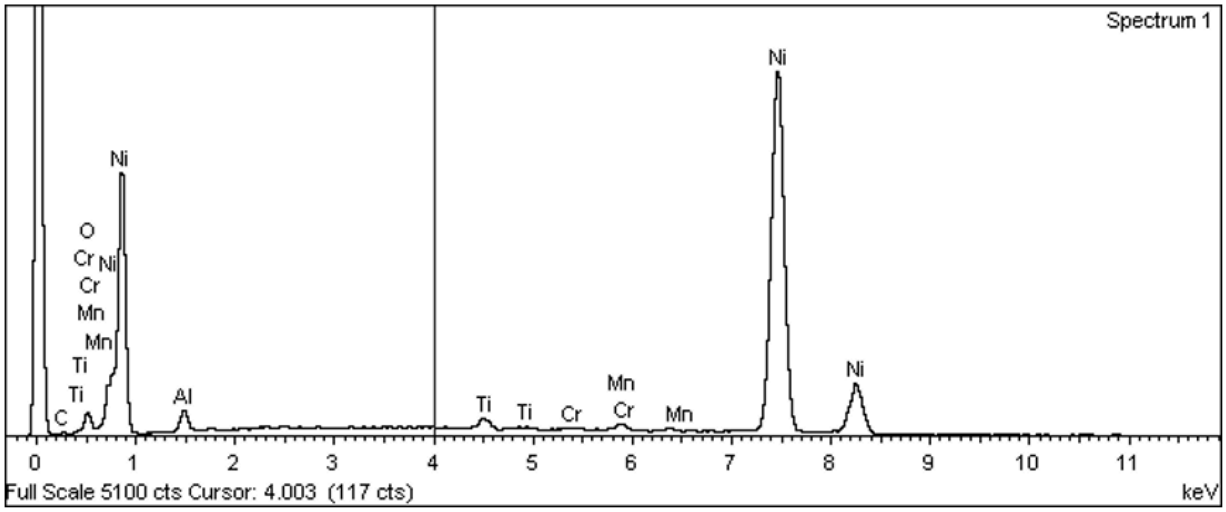

***Figure 32**: EDS spectrum of untreated nickel felt.*

Element	Weight%	Weight% Sigma	Atomic%
C K	1.96	0.47	8.11
O K	3.09	0.28	9.56
Al K	1.92	0.13	3.53
Ti K	0.98	0.10	1.01
Cr K	0.19	0.10	0.19
Mn K	0.70	0.11	0.64
Ni K	91.15	0.56	76.97
Totals	100.00		

***Table 6:** EDS results of untreated Ni felt.*

The analysis of the elemental composition of the untreated nickel felt support confirms that the material is mainly composed by metallic nickel: it appears as the most prominent peak in the spectrum, with an atomic percentage value of 76.97%.

In addition to nickel, also carbon and oxygen are present, in minor quantities. Oxygen, at 9.56% atomic, can be attributed to surface oxidation, while the carbon, at 8.11% atomic, is likely due to organic contaminations.

Traces amounts of other elements, including as Al, Ti, Cr and Mn, were also detected, probably deriving from the manufacturing process of the nickel felt.

4.1.2. 350°C Thermally Treated Nickel Felt

The nickel felt support, a porous grey material, exhibits a noticeable change in appearance after the 350°C thermal treatment, as can be seen from the images below. These differences suggest modifications in the surface composition, probably attributed to a surface oxidation. Differences between the treated and untreated sample have been further investigated with SEM technology.

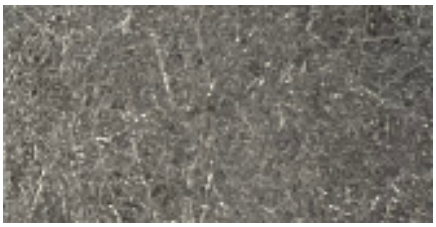

Figure 33: *Untreated Ni felt support.*

Figure 34*: 350°C-treated Ni felt support.*

Probably, during the heating step, the Nickel have reacted with O_2 from air to form a very thin Nickel oxides layer on the surface, with the thickness of the oxides layer responsible for the bluish hue. This phenomenon, addressed as “thin-film interference”, occurs when light waves reflect off both the top and the bottom of the film, interacting the one with the other and increasing the reflection of a certain wavelengths, which causes the colourful interference seen in the reflected light.

The nickel felt subjected to a temperature of 350°C has been analysed with SEM technology on the side where no catalyst was deposited, to investigate the effect of the high temperature treatment and to confirm the surface oxidation supposed by observing the bluish colour of the treated electrode. SEM images are showed below.

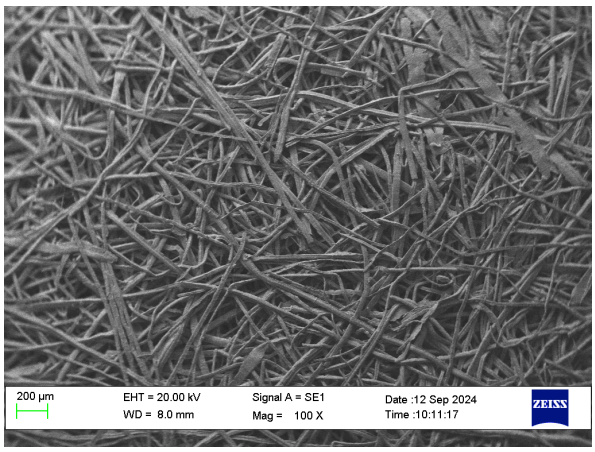

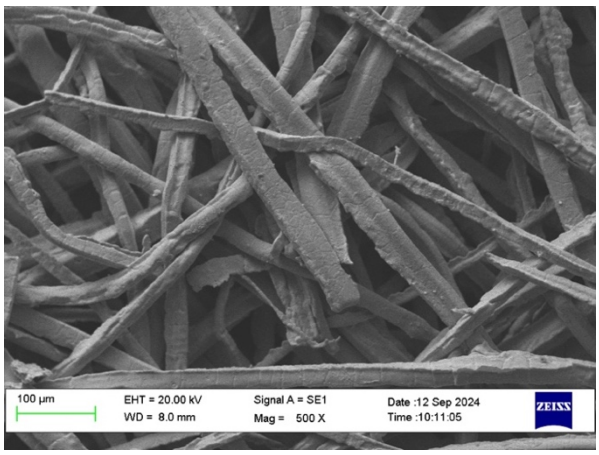

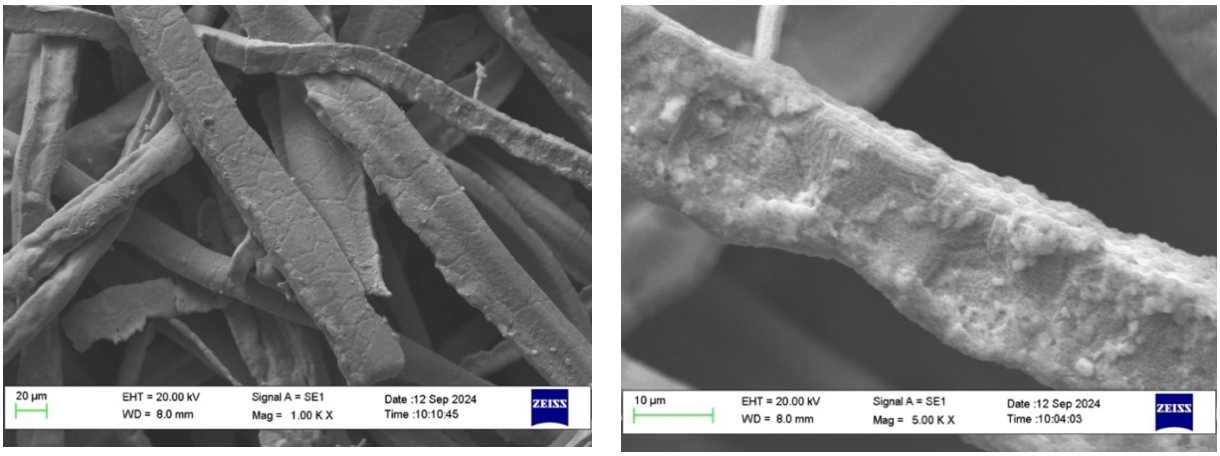

***Figure 35**: SEM image of 350°C thermally treated nickel felt, captured at 100X, 500X, 1,00 KX, 5,00KX magnification.*

The nickel felt support treated at 350°C presents a rough surface with noticeable bumps: the support has probably undergone oxidation. The modification of the surface may reduce the uniformity of adhesion of the catalyst, that can lead to increased risk of detachment and reduced overall efficiency of the electrochemical system. However, this hypothesis needs to be verified through the analysis of $NiFe_2O_4$-coated side of the electrode and by conducting electrochemical tests.

The underlying chart shows the EDS spectrum of the high temperature thermally treated nickel felt, while the following table offers a comprehensive overview of its elemental composition.

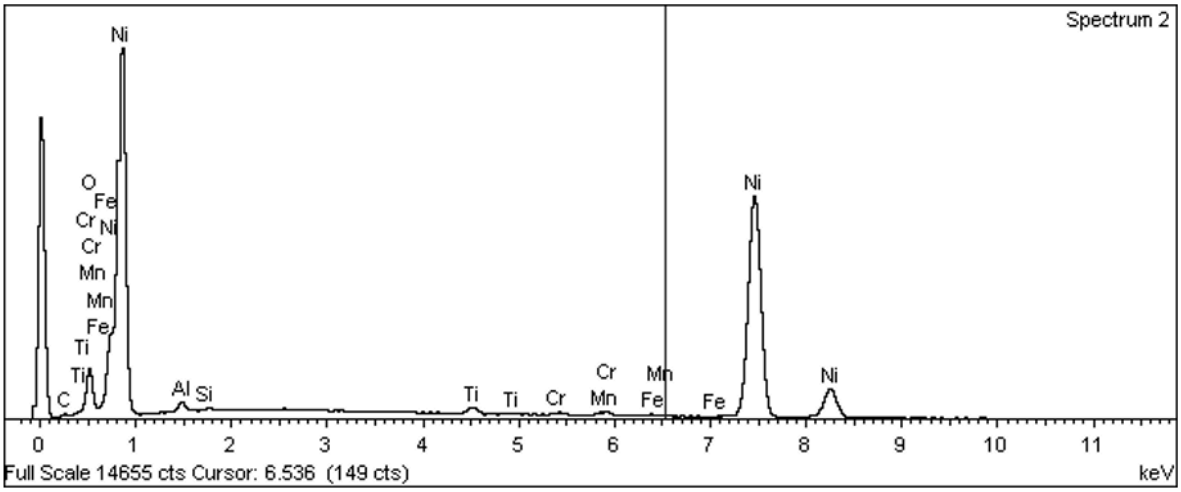

***Figure 36**: EDS spectrum of 350°C thermally treated nickel felt.*

Element	Weight%	Weight% Sigma	Atomic%
C K	2.23	0.31	7.30
O K	14.84	0.28	36.51
Al K	0.35	0.07	0.51
Cr K	0.71	0.08	0.54
Mn K	0.65	0.08	0.47
Fe K	6.19	0.13	4.36
Ni K	75.03	0.38	50.32
Totals	100.00		

***Table** 7: EDS results of 350°C thermally treated nickel felt.*

The higher degree of oxidation, suggested by the SEM images, is confirmed by the EDS analysis, showing a significantly higher oxygen content (36.51% atomic) compared to the untreated nickel felt (9.56% atomic).

4.1.3. 120°C Thermally Treated Nickel felt

The nickel felt treated at a temperature of 120°C has been analysed through SEM microscopy on the side where no catalyst was deposited, to investigate the effect of the lower-temperature treatment. SEM images are showed below.

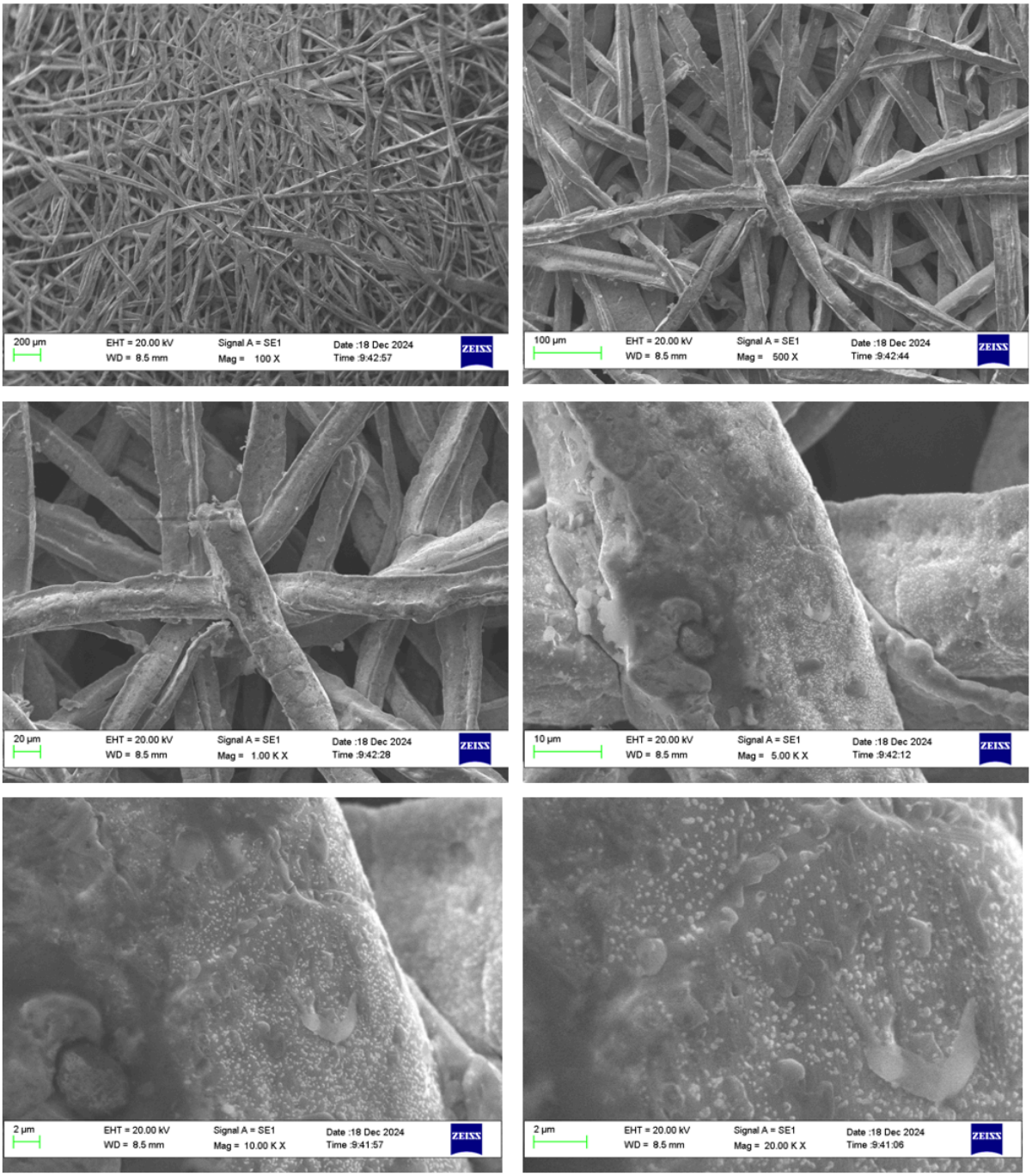

Figure 37: *SEM image of 120°C thermally treated nickel felt, captured at 100X, 500X, 1,00 KX, 5,00KX, 10,00 KX 20,00KX, magnification.*

The underlying chart shows the EDS spectrum of the low temperature thermally treated nickel felt, while the following table offers a breakdown of its elemental composition.

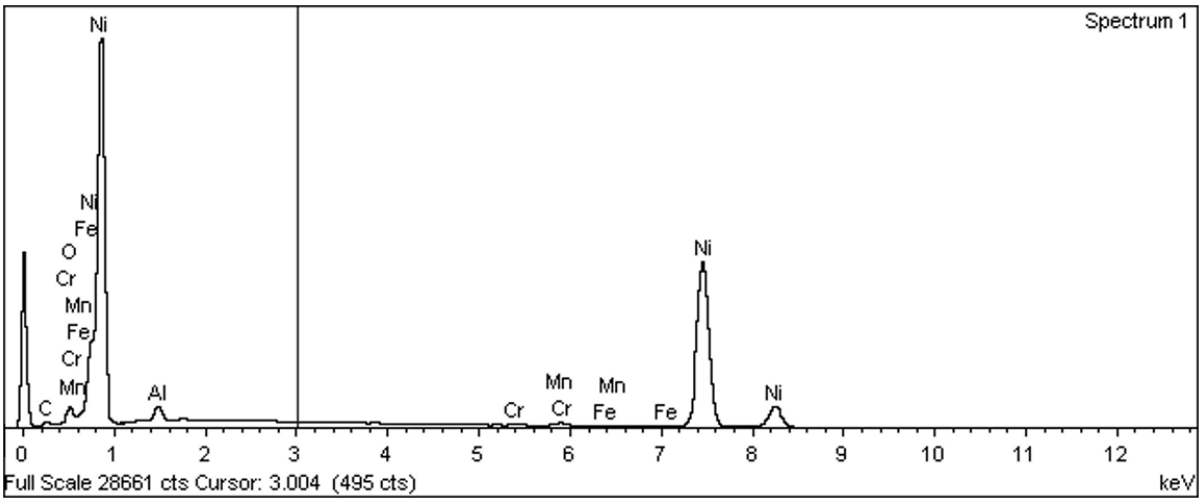

***Figure 38**: EDS spectrum of 120°C thermally treated nickel felt.*

Element	Weight%	Weight% Sigma	Atomic%
C K	5.41	0.47	19.37
O K	4.62	0.25	12.40
Al K	2.68	0.11	4.27
Cr K	0.34	0.06	0.29
Mn K	0.69	0.07	0.54
Fe K	0.24	0.06	0.19
Ni K	86.01	0.51	62.96
Totals	100.00		

***Table 8**: EDS results of 120°C thermally treated nickel felt.*

Similarly to the 350°C-treated nickel felt, also the sample treated at lower temperature presents a rough surface with visible bumps (figure 37), probably derived from an oxidation. However, the atomic percentage of oxygen in the 120°C-treated sample (12.40%) is not significantly higher compared to the untreated one (9.56%).

The elementals compositions of the uncoated nickel felts support in its untreated, 350°C-treated and 120°C-treated form have been compared to highlight any differences induced by the thermal treatment. Data are showed below.

Element atomic %	**Untreated Ni felt**	**350°C-treated Ni felt**	**120°C-treated Ni felt**
Carbon (C)	8.11%	7.30%	19.37%
Oxygen (O)	9.56%	36.51%	12.40%
Iron (Fe)	Not detected	4.36%	0.19%
Aluminium (Al)	3.53%	0.51%	4.27%
Titanium (Ti)	1.01%	Not detected	Not detected
Chromium (Cr)	0.19%	0.54%	0.29%
Manganese (Mn)	0.64%	0.47%	0.54%
Nickel (Ni)	76.97%	50.32%	62.96%

Table 9*: Comparison of atomic percentages of elements of the untreated, 120°C and 350°C-treated nickel felts.*

Nickel is the most abundant element in all the samples in terms of atomic percentage, however it decreases in both thermally treated samples, due to an increased percentage of other elements, particularly oxygen. The treated samples are more oxidized respect to the untreated one. In particular, the sample treated at 350°C shows a notable higher degree of oxidation: this result confirms the surface oxidation of the material following the heat treatment in air, as assumed by observing the change in colour of the high temperature treated sample (figure 33 and 34) and SEM images. However, to investigate whether the oxidation is extended to the bulk of the material or limited to the surface, XRD analysis are be performed and presented in paragraph 4.2.2.

Iron presence in the 350°C-treated nickel felt is likely deriving from the $NiFe_2O_4$ catalytic layer deposited on the other side of the electrode, due to its diffusion trough the porous nickel felt, a process that is enhanced by elevated temperature.

Carbon detected in all the samples is probably deriving from nickel felt manufacturing process or residues of solvents. Its increase in the 120°C-treated sample can derive from the incomplete removal of organic contaminants derived from manufacturing process, that are instead eliminated at higher temperatures due to the thermal decomposition and oxidation processes.

4.1.4. Untreated $NiFe_2O_4$-Coated Side of the Electrode

The untreated $NiFe_2O_4$-coated side of the electrode has been characterized through SEM imaging in order to evaluate the morphology of the catalyst and its distribution on the nickel felt support. SEM images are showed below.

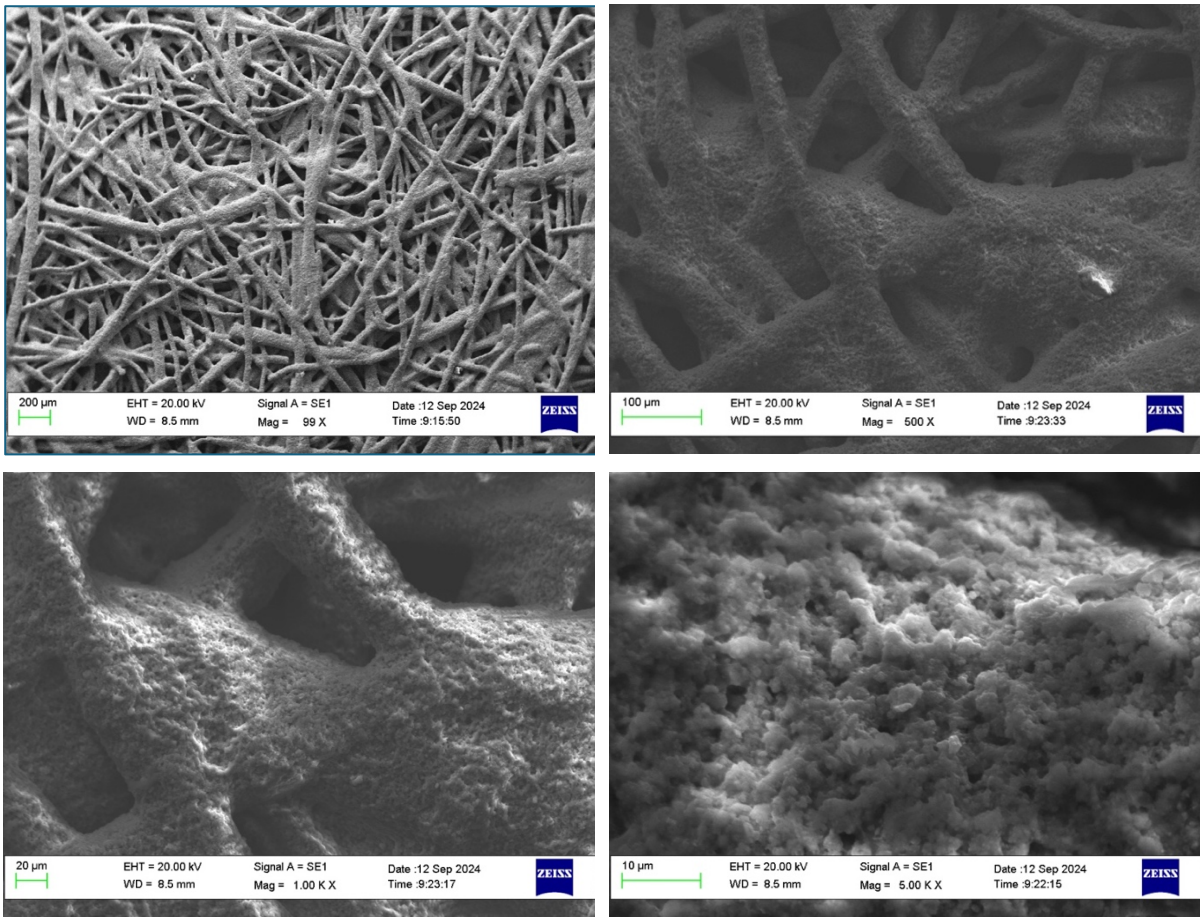

***Figure 39**: SEM image of untreated $NiFe_2O_4$-coated side of the electrode, captured at 100X, 500X, 1,00 KX, 5,00KX magnification.*

The analysis of the SEM images reveals that the shape of the underlying nickel felt fibres is still visible, with $NiFe_2O_4$ catalytic layer deposited on top, covering all the Ni surface. The deposition appears to be homogeneous on the surface and does not obstruct the pores of the Ni felt, which remain clearly visible. The preserved porosity is essential to ensure an efficient diffusion of reactants and product during the electrochemical reactions.

These results confirm that the deposition process has been properly performed.

The plot below presents the EDS spectrum of the untreated $NiFe_2O_4$ coated side of the electrode, and the following table provides a breakdown of its elemental composition.

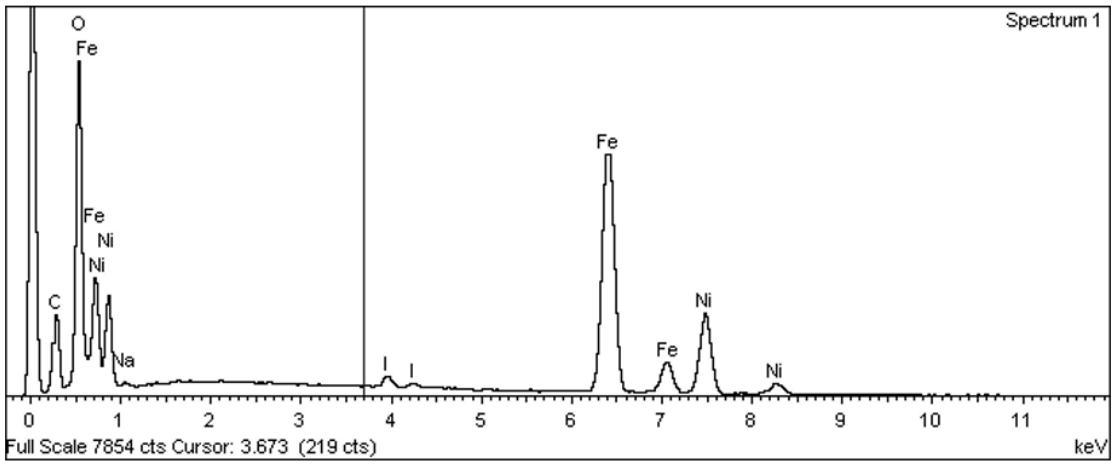

***Figure 40**: EDS spectrum of untreated $NiFe_2O_4$-coated side of the electrode.*

Element	Weight%	Weight% Sigma	Atomic%
C K	18.90	0.39	34.65
O K	34.42	0.33	47.36
Na K	0.43	0.10	0.41
Fe K	29.38	0.26	11.58
Ni K	15.22	0.22	5.71
I L	1.66	0.11	0.29
Totals	100.00		

***Table 10**: EDS results of untreated $NiFe_2O_4$-coated side of the electrode.*

The EDS analysis of the $NiFe_2O_4$ coated side of the electrode shows a reduced nickel presence (5.71% atomic) respect to the uncoated side (76.97% atomic), suggesting that this side of the surface is largely covered by the catalyst and the underlying felt layer is less exposed.

It is evident also a significantly higher O_2 content (47.36% atomic) respect to the felt side (9.56%): this increase in oxygen is consistent with the catalyst being an oxide, confirming its successfully deposition. In addition, also the presence of iron (11.58% atomic) is coherent with the composition of the $NiFe_2O_4$ catalyst.

Finally, carbon (34.65% atomic) and iodine (0.29% atomic) presence can be attributed to residue of reagents used during the preparation of the catalytic ink, such as solvents and ionomer (which has iodine and carbon in its structure).

The differing composition of the spectra between the nickel felt side and the side where $NiFe_2O_4$ was deposited confirms the successful formation of the $NiFe_2O_4$ layer.

4.1.5. 350°C Thermally Treated $NiFe_2O_4$-Coated Side of the Electrode

The SEM analysis of the $NiFe_2O_4$-coated side of the electrode after the treatment at 350°C is crucial to understand the effect of the thermal treatment. SEM images are showed below.

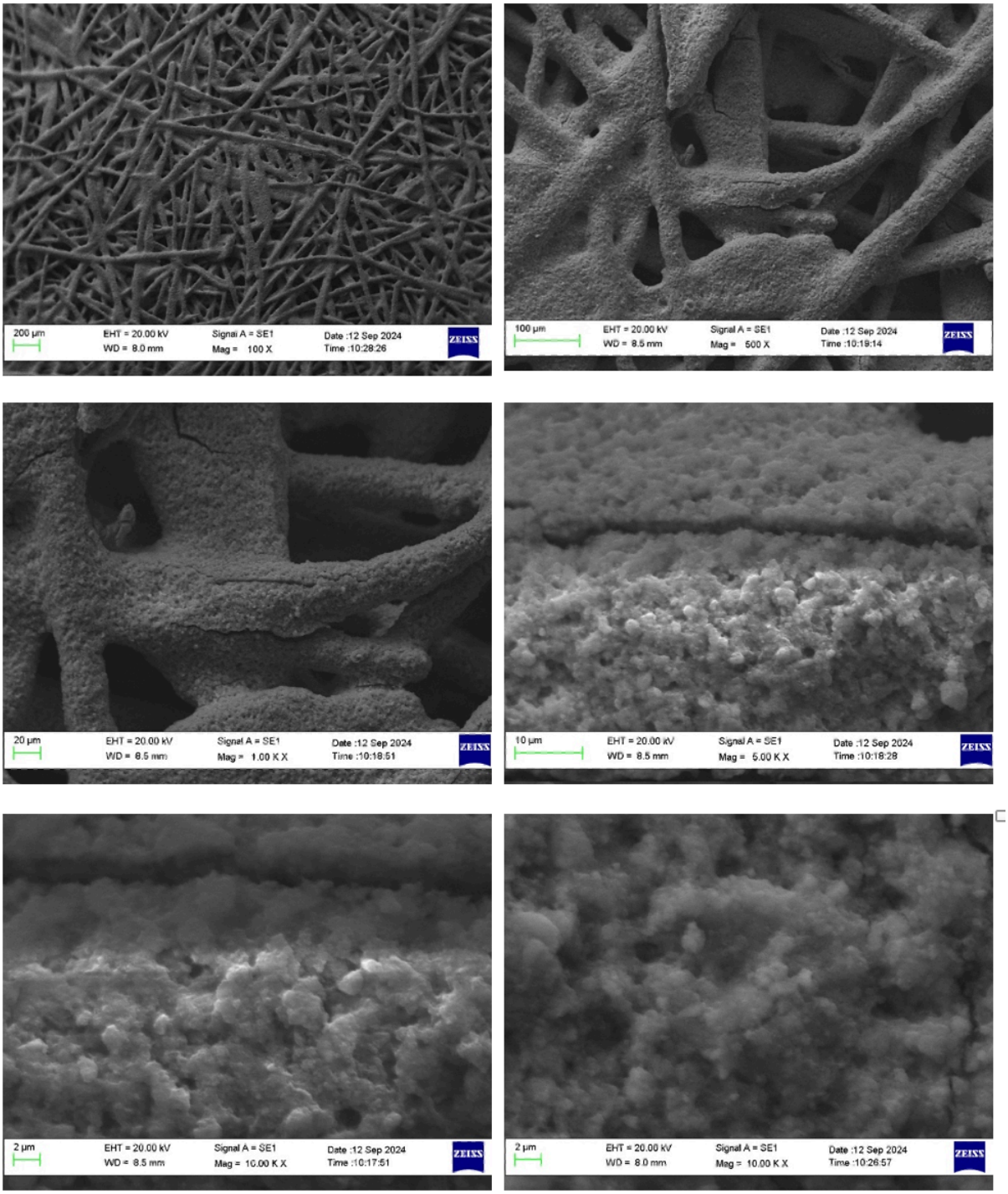

Figure 41: *SEM image of 350°C thermally treated $NiFe_2O_4$-coated side of the electrode, captured at 100X, 500X, 1,00 KX, 5,00KX, 10,00 KX, magnification.*

SEM images indicates that the $NiFe_2O_4$ catalytic layer remains overall adhered to the support after the heat treatment, indeed there are no areas where the underlying fibres are exposed, or the catalyst has detached. This indicates that the heat treatment has not compromised the immediate adhesion of the catalytic layer. However, some cracks are visible, that suggest potential stress point that could evolve over time and cause catalyst detachment from support, resulting in a non-uniform distribution of the catalyst, which reduces its efficiency.

The stability of the electrode will be assessed through performance tests conducted in the electrochemical cell using an electrochemical workstation. These tests will determine whether the material integrity is maintained over time and evaluate how the catalyst and the support behave under operational conditions. The results, including polarization curves, are presented and discussed in paragraph 5.

The underlying chart shows the EDS spectrum of the 350°C thermally treated $NiFe_2O_4$-coated side of the electrode, while the following table offers a comprehensive overview of its elemental composition.

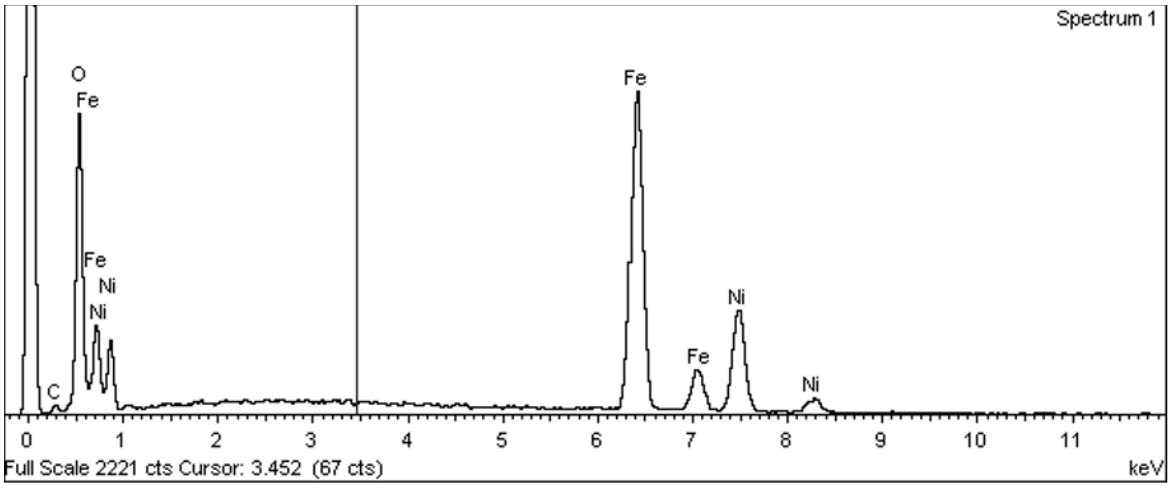

***Figure 42**: EDS spectrum of 350°C thermally treated $NiFe_2O_4$-coated side of the electrode.*

Element	Weight%	Weight% Sigma	Atomic%
C K	3.47	0.57	8.84
O K	28.43	0.55	54.43
Fe K	44.85	0.58	24.60
Ni K	23.26	0.52	12.13
Totals	100.00		

***Table 11**: EDS results of 350°C thermally treated $NiFe_2O_4$-coated side of the electrode.*

The decline in iodine and carbon following the treatment at 350°C can explain the morphological changes observed in SEM images, such as cracks formation.

In particular, EDS analyses show that the untreated catalyst contains 0.29 atomic percentage of iodine, whereas the thermally treated catalyst shows no detectable iodine, indicating a complete depletion. Since iodide is part of the ionomer, its depletion can be attributed to the breakdown of the ionomer structure and such degradation can weaken the binding between the catalyst particles and the support, making the material less flexible and prone to cracking under mechanical and thermal stress. Additionally, the degradation of the ionomer can also impact the overall performance, as it is essential to ensure ionic conductivity.

Also, a significant reduction in carbon content is observed, decreasing from 34.65% atomic in the untreated sample to 8.84% atomic in the 350°C-treated sample. While some of this reduction can be attributed to the degradation of the ionomer, it is important to note that carbon is present also in solvents and contaminants from the manufacturing process, which probably have been removed by the high temperature.

The treated electrode shows a higher degree of oxidation (54.43% of O by atom) respect to the untreated one (47.36% atomic). This suggests that the catalyst undergo modification during the heat treatment.

The comparison between untreated and 350°C thermally treated electrodes on both the coated and uncoated sides highlight that, although the high temperatures remove some impurities, the structural integrity of the electrode is partially compromised. The structural changes observed could be related to a reduction in performance, hypothesis which has to be verified by polarization curves in paragraph 5.1.

4.1.6. 120° C Thermally Treated $NiFe_2O_4$-Coated Side of the Electrode

The SEM analysis of the $NiFe_2O_4$-coated side of the electrode treated at 120°C has been performed to evaluate any morphological changes induced by the lower temperature thermal treatment. SEM images are showed below.

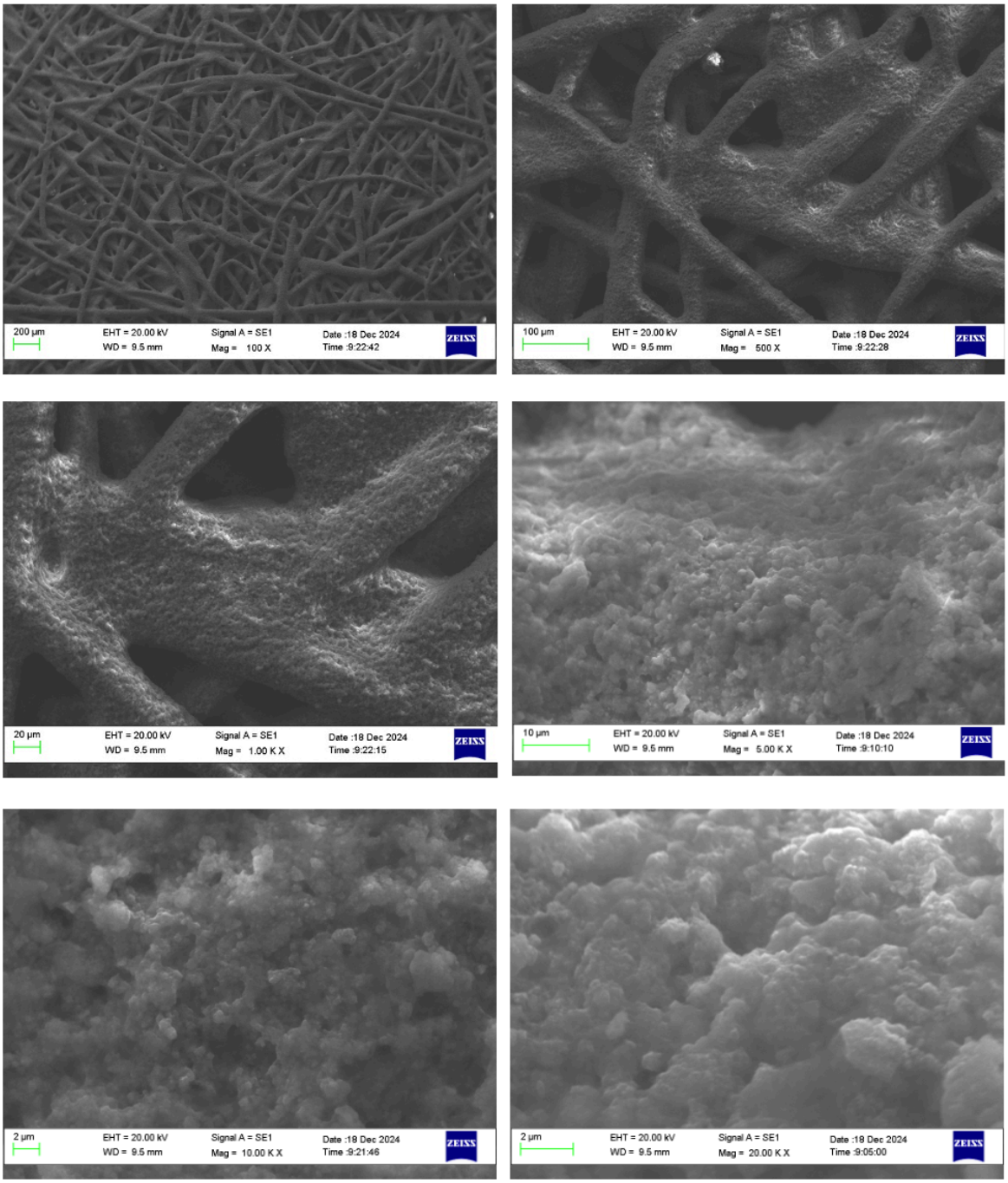

Figure 43: *SEM image of 120°C thermally treated $NiFe_2O_4$-coated side of the electrode, captured at 100X, 500X, 1,00 KX, 5,00KX, 10,00 KX, 10,00 KX magnification.*

Comparing the untreated electrode and the one treated at 120°C, no significant morphological differences have been observed, which indicates that the lower-temperature thermal treatment did not significantly alter the surface of the electrode. Furthermore, the treatment did not negatively affect the uniformity of the surface, and no visible cracks were detected. However, it is important to note that the untreated sample is already subjected to a temperature of 90°C during the deposition process, which is not substantially lower than the treatment temperature.

The underlying plot shows the EDS spectrum of the low temperature thermally treated $NiFe_2O_4$ coated side of the electrode, while the following table offers a comprehensive overview of its elemental composition.

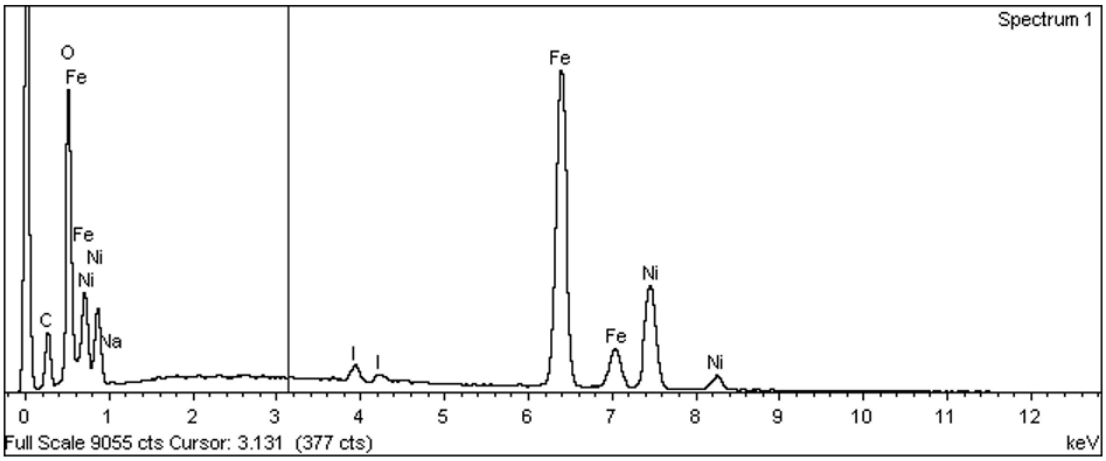

***Figure 44**: EDS spectrum of 120°C thermally treated $NiFe_2O_4$-coated side of the electrode.*

Element	Weight%	Weight% Sigma	Atomic%
C K	14.91	0.34	31.07
O K	28.23	0.27	44.16
Na K	0.34	0.09	0.37
Fe K	35.97	0.26	16.12
Ni K	18.43	0.21	7.86
I L	2.13	0.11	0.42
Totals	100.00		

***Table 12:** EDS results of 120°C thermally treated NiFe2O4-coated side of the electrode.*

The presence of the iodide and carbon in the electrode treated at 120°C, as demonstrated by EDS analysis, confirms the integrity of the ionomer that ensures the adhesion of the catalyst on the support.

These results confirm that the 120°C thermal treatment preserves the structural integrity of the electrode.

4.2. X-ray Diffraction (XRD) Analysis

X-ray diffraction (XRD) is a non-disruptive analytical technique, useful to understand the structure and the phase purity of the sample.

An electromagnetic radiation can be diffracted by atomic planes only if its wavelength is on the same scale as twice the interatomic distance (d), or smaller. X-rays are used because their wavelength, in the nanometre range, is short enough to match the interatomic distances found in crystals.

X-rays are produced in a cathode ray tube by heating a filament to generate electrons. A voltage is then applied to accelerate the electrons toward a target material. When a sample is exposed to X-ray irradiation, several physical interactions occur, such as photon absorption through photoelectric effect, heat generation, fluorescence emission, electron production, and scattering. Scattering can be classified into two types:

- Inelastic scattering: the scattered photons lose energy.
- Elastic scattering: when X-rays pass through a crystal structure, the photons are scattered by the electrons in the atoms and retain their original wavelength. Each atomic plane contributing to the scattering. This scattering gives rise to the phenomenon of X-ray diffraction. The interaction of X-rays with the atomic planes in a crystal produces diffraction patterns, revealing structural information.

When the X-rays hit the sample, part of the radiation is reflected by one atomic plane, while another part is reflected by an adjacent one. The X-rays travel different paths, since the planes are not in the same position, this difference depends on the distance between the two atomic planes and the angle θ at which the X-rays hit the crystal. To produce constructive interferences, the path difference must be an integer multiple of the X-ray wavelength, satisfying Bragg's law:

$$\text{path difference} = 2d\sin\theta = n\lambda$$

Where:

- d is the interplanar distance: the spacing between adjacent atomic planes in a crystal lattice;
- λ is the wavelength of X rays;

- n is the order of diffraction;
- 2θ is the angle of diffraction: the angle at which the X-rays are diffracted off the planes of atoms in the crystal, it is measured between the incident beam and the plane of reflection.

When the waves from adjacent planes interfere constructively, it is produced a diffracted beam, which forms a unique pattern that depends on the crystal's structure, the interplanar spacing (d), and the wavelength of the X-rays (λ).

From the X-ray diffraction analysis, a diffractogram is obtained: a graph representing the intensity of the diffracted rays as a function of the diffraction angle (2θ). This plot is valuable for identifying the crystalline structure of a material: the peaks observed in the plot are characteristic of the phases present within the sample. The appearance of a peak indicates the presence of a crystalline phase, the position and pattern of the peaks indicate specific phases. A "search and match" analysis is performed, allowing the identification of the phases present in the sample by comparing the observed peaks with known phases from a database.

Moreover, the XRD analysis provides insights on the crystallite dimensions, that can be estimated from the width of the peaks using the Sheerer equation, which allows the determination of the average crystallite size "D": [33]

$$D = \frac{K\lambda}{\beta \cos\theta}$$

Where:

- K is the shape factor or Scherrer constant, typically between 0.89 and 1, its value depends on the shape of the crystallites;
- λ is the wavelength of the X-ray radiation used, in this case Cu;
- β is the full width at half maximum (FWHM) of the diffraction peak, in radiant;
- θ is the Bragg angle, half of the 2θ value at which the diffraction peak occurs.

As stated by the equation, the average crystal size is inversely proportional to the width of the diffraction peak, with broader peaks indicating smaller crystal sizes.

The dimension of crystallites is a critical parameter that significantly influences catalytic activity: smaller crystallites guarantee a higher surface area, resulting in an increased number

of active sites available for reactions. Moreover, a nanometric size of the catalytic powder ensures a homogeneous dispersion in the solvents, that determines a proper deposition of the catalytic ink on the support.

Finally, the peak intensity of the diffractogram depends on the number of atoms that are capable of scattering X-ray. Since crystalline portions interacts more effectively with X-rays respect to amorphous regions, high intensities typically indicate a higher crystalline fraction in the sample or a greater number of scattering atoms. Crystallinity is an important parameter that affects both the catalytic activity and the chemical stability of a material. High crystallinity typically enhances chemical stability, due to the ordered and robust structure. On the other hand, materials with lower crystallinity often exhibit more catalytic sites due to the presence of structural defects and amorphous regions, which behave as active centres for catalysis.

During this research, the samples were characterized using X-ray diffraction (XRD) with a Philips X'Pert X'Celerator system. The analysis was conducted using Cu-Kα radiation over a 2θ range of 5–80°, with a step size of 0.1° to ensure high-resolution data collection.

XRD analysis have been conducted on $NiFe_2O_4$ powder, as well as on electrodes, including untreated samples and those treated at 350°C and 120°C. The analytical purpose of these analysis was to identify the predominant crystal phases in the samples, checking whether the ink deposition has been successful; and to evaluate the effects of the thermal treatments on the crystalline structure, as well as on particle dimensions, which have been estimated using Sheerer equation.

Subsequently, XRD analysis have been conducted on NiO and Co_3O_4 electrodes threated at 120°C, in order to identify the crystal phases and to estimate particle dimensions and compare the results with the 120°C $NiFe_2O_4$ sample.

4.2.1. Untreated Nickel Felt

The XRD analysis of the nickel felt was performed to identify its predominant crystalline phases. This analysis is crucial for subsequent comparisons with the $NiFe_2O_4$-coated side of the electrode, allowing an accurate characterization by distinguishing and eliminating the peaks originating from the support from those of the catalytic layer.

The resulting diffractogram is presented below. The X-axis represents the diffraction angle 2θ in degrees, while the Y-axis indicates the intensity in counts per second (cps).

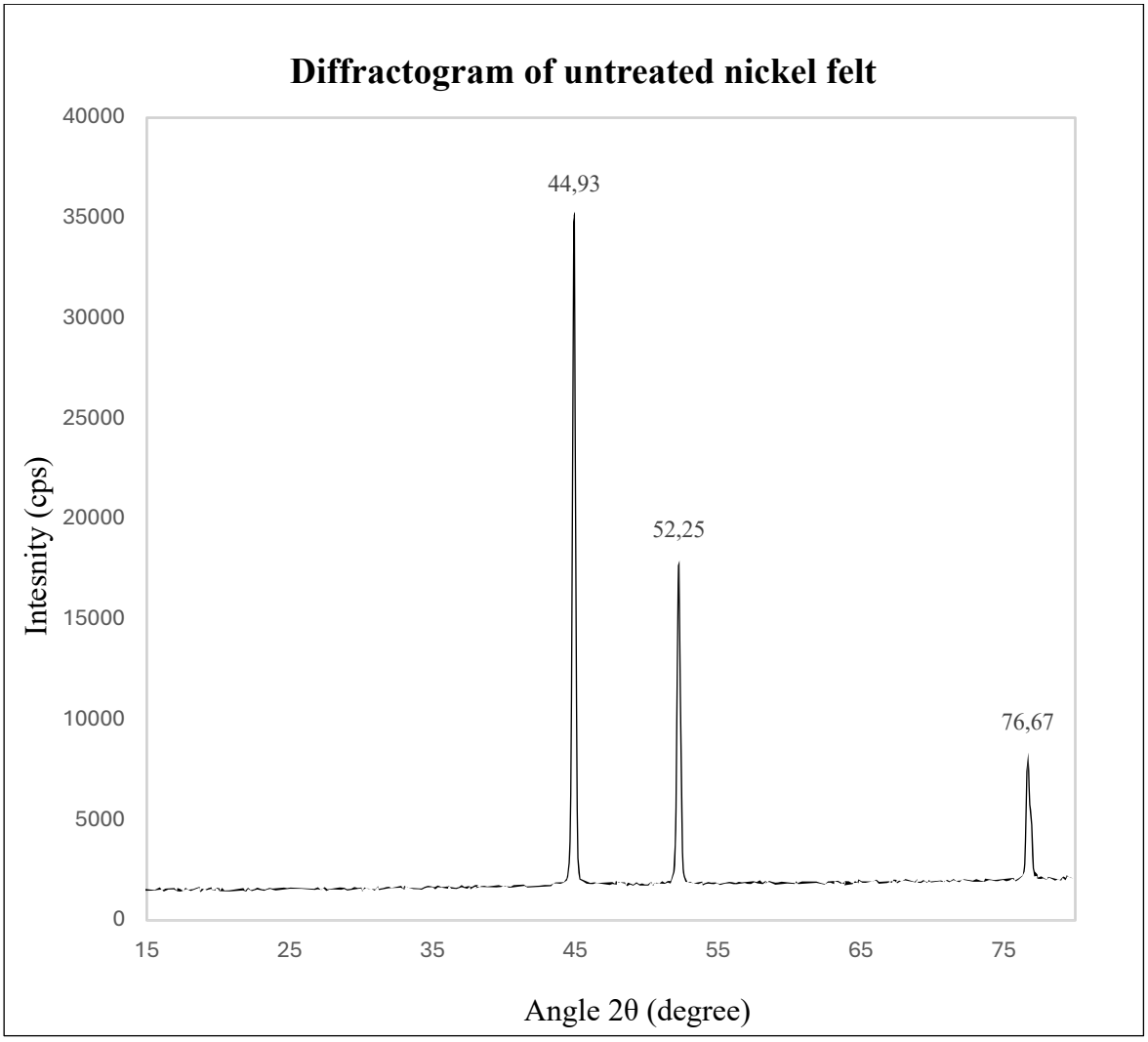

***Figure 45**: Diffractogram of untreated nickel felt.*

Below is a comparison between the peaks list of the sample and the reference standard for Ni:

Untreated Ni felt support		**Ni reference** 00-001-1260
Intensity	Angle 2θ	Angle 2θ
35148 cps	**44.93°**	44.60°
17937 cps	52.25°	51.91°
8362 cps	76.67°	76.81°

***Table 13**: Predominant peaks of the Ni felt support sample compared with the reference standard for Ni.*

As expected, the peaks observed in the diffractogram of the nickel felt correspond to the standard metallic nickel (Ni) reference, confirming the crystalline structure of the support. This result indicates that the support is predominantly composed of nickel, without evident impurities or secondary phases.

4.2.2. 350°C Thermally Treated Nickel Felt

Based on the SEM analysis (paragraph 4.1.2.) and the observed bluish colour after the 350°C heat treatment (figures 33 and 34), which suggested possible oxidation, XRD analysis was conducted on the 350°C thermally treated nickel felt support. The purpose of the analysis was to determine whether the observed oxidation was limited to the surface or extended into the bulk of the material.

The resulting diffractogram is showed below. The X-axis represents the diffraction angle 2θ in degrees, while the Y-axis indicates the intensity in counts per second (cps).

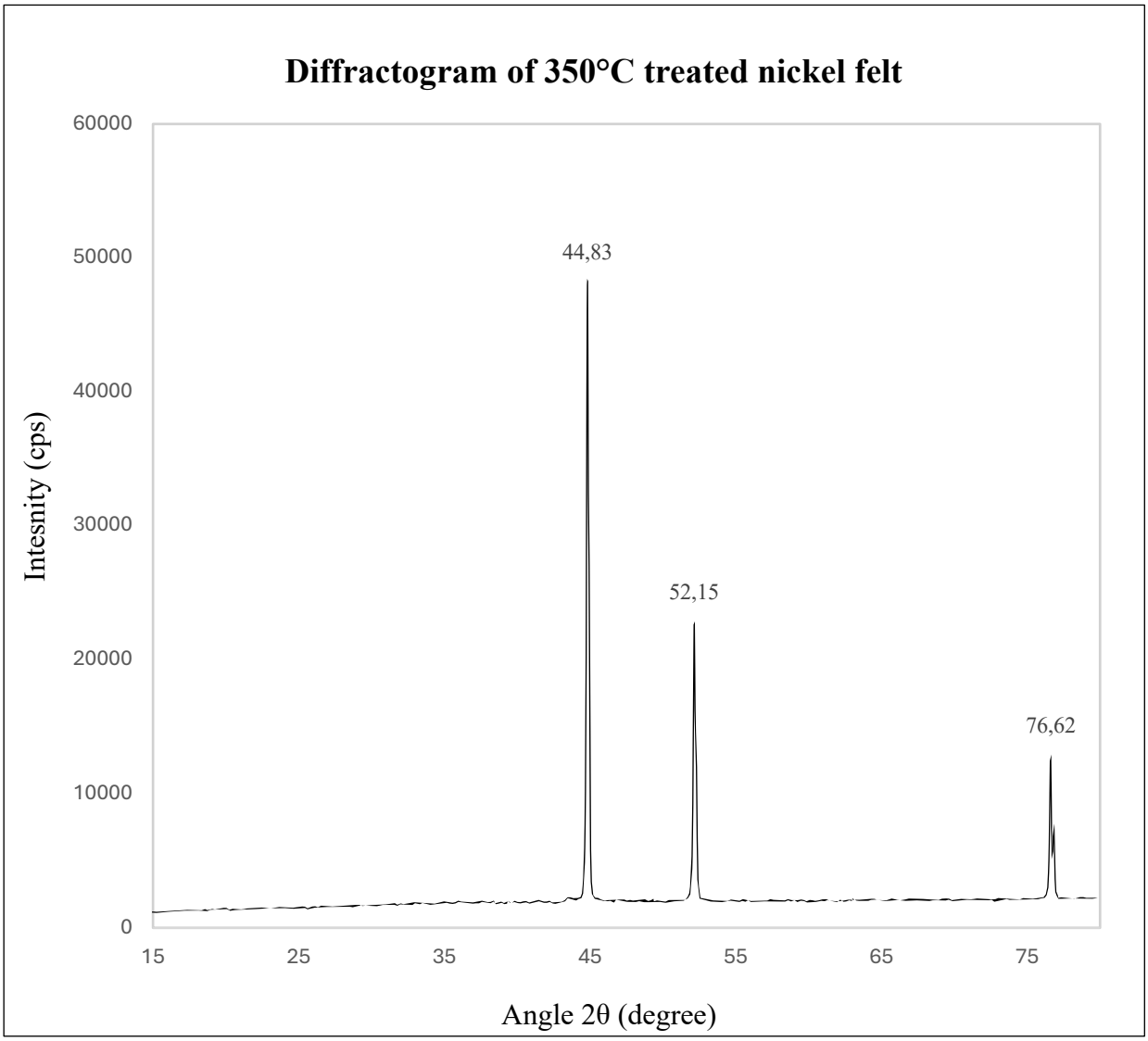

Figure 46: *Diffractogram of 350°C thermally treated nickel felt.*

Below the peaks list of 350°C thermally treated nickel felt sample is compared with the untreated sample and the reference standard for Ni:

Untreated Ni felt support		**350°C-treated Ni felt support**		**Ni reference** 00-001-1260
Intensity	Angle 2θ	Intensity	Angle 2θ	Angle 2θ
35148 cps	**44.93°**	**48258 cps**	**44.83°**	44.60°
17937 cps	52.25°	22870 cps	52.15°	51.91°
8362 cps	76.67°	12938 cps	76.62°	76.81°

Table 14: *Predominant peaks of the treated and untreated Ni felt support sample compared with the reference standard for Ni.*

Analysing the peaks, it appears that the crystal structure of the nickel felt support is not significantly changed after the heat treatment: the felt is still predominantly composed of metallic nickel.

The characteristic peaks of nickel oxide, listed below, are absent in the sample, indicating that no significant oxidation occurred.

NiO reference 01-071-1179
Angle 2θ
37.24°
43.27°
62.85°
75.37°
79.36°

Table 15: *Reference standard peaks for NiO.*

These results indicates that the oxidation of the nickel felt support after the 350°C thermal treatment was limited to the surface, as XRD, being a bulk-sensitive technique, has not highlighted evidence of oxidation in the bulk.

4.2.3. $NiFe_2O_4$ Powder

The XRD analysis of the commercially available $NiFe_2O_4$ powder was performed to understand its crystal structure and use it as a benchmark to evaluate the structure of the $NiFe_2O_4$ catalyst deposited on the electrode. This comparison is crucial to confirm the retention of the crystalline phase after the deposition or to assess any structural modifications.

Moreover, the characterization of the powder allows the estimation of particle dimensions, discussed in paragraph 4.3.

The image below presents the diffractogram of $NiFe_2O_4$ powder. The X-axis represents the diffraction angle 2θ in degrees, while the Y-axis indicates the intensity in counts per second (cps).

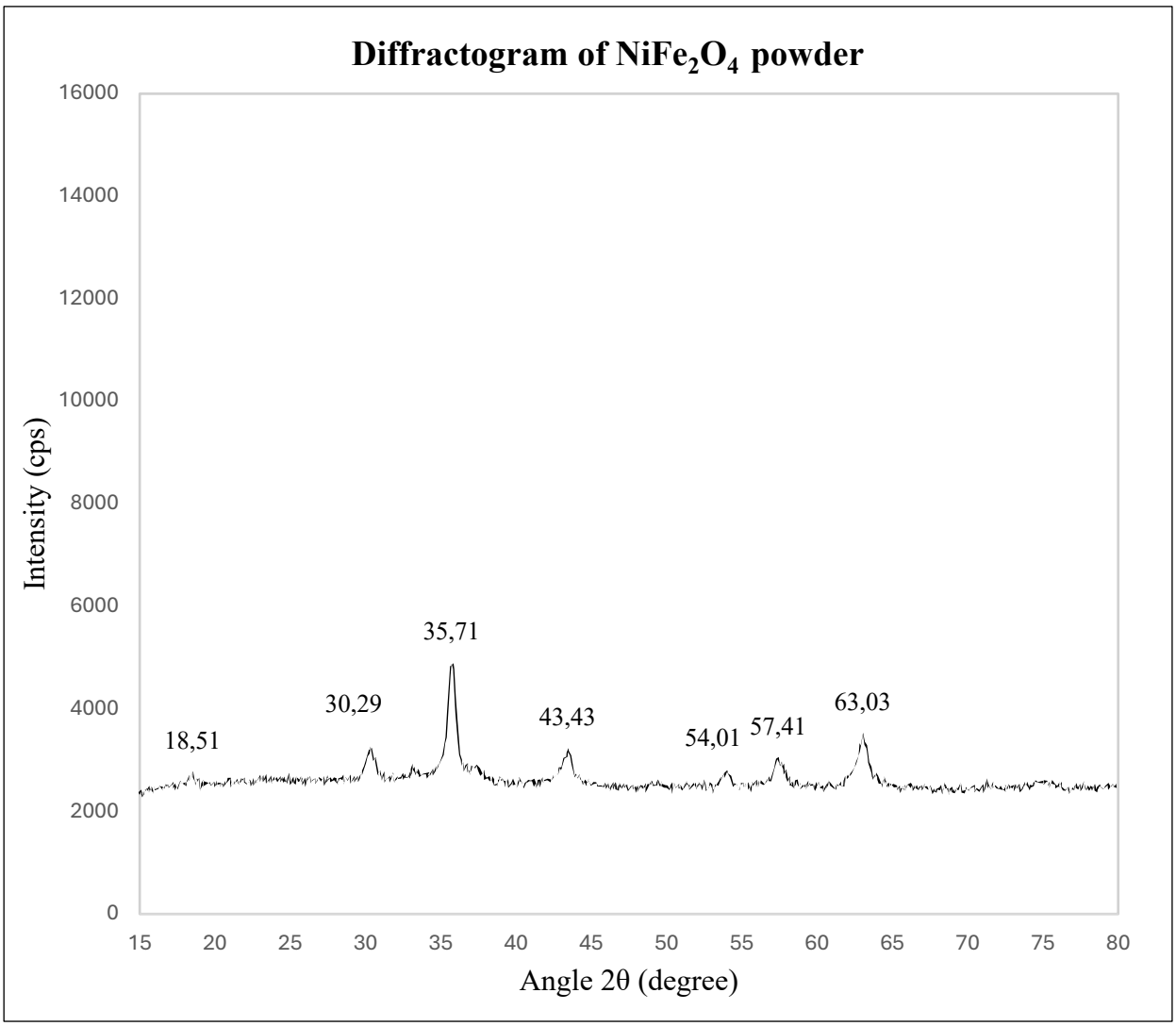

***Figure 47**: Diffractogram of $NiFe_2O_4$ powder.*

Below there is a comparison between the peaks list of the sample and the reference standard for $NiFe_2O_4$:

$NiFe_2O_4$ powder		**$NiFe_2O_4$ reference** 00-054-0964
Intensity	Angle 2θ	Angle 2θ
2778	18.51°	18.43°
3273	30.29°	30.31°
4908	**35.71°**	**35.70°**
3238	43.43°	43.38°
2796	54.01°	53.82°
3056	57.41°	57.40°
3526	63.03°	63.02°

***Table 16**: Predominant peaks of the $NiFe_2O_4$ powder sample compared with the reference standard for $NiFe_2O_4$.*

The peaks of $NiFe_2O_4$ powder align with the reference pattern for $NiFe_2O_4$, confirming that the powder consists primary of spinel-structured nickel ferrite. The absence of other peaks highlights the material's single-phase structure and indicates a high level of purity without significant contaminations.

4.2.4. Untreated $NiFe_2O_4$-Coated Side of the Electrode

Additional XRD analysis were carried out on the CCS-electrodes to characterize the structural properties of the $NiFe_2O_4$ catalytic layer, before and after the temperature treatments.

Below is showed the diffractogram of the $NiFe_2O_4$-coated side of the electrode in its untreated form. The X-axis represents the diffraction angle 2θ in degrees, while the Y-axis indicates the intensity in counts per second (cps).

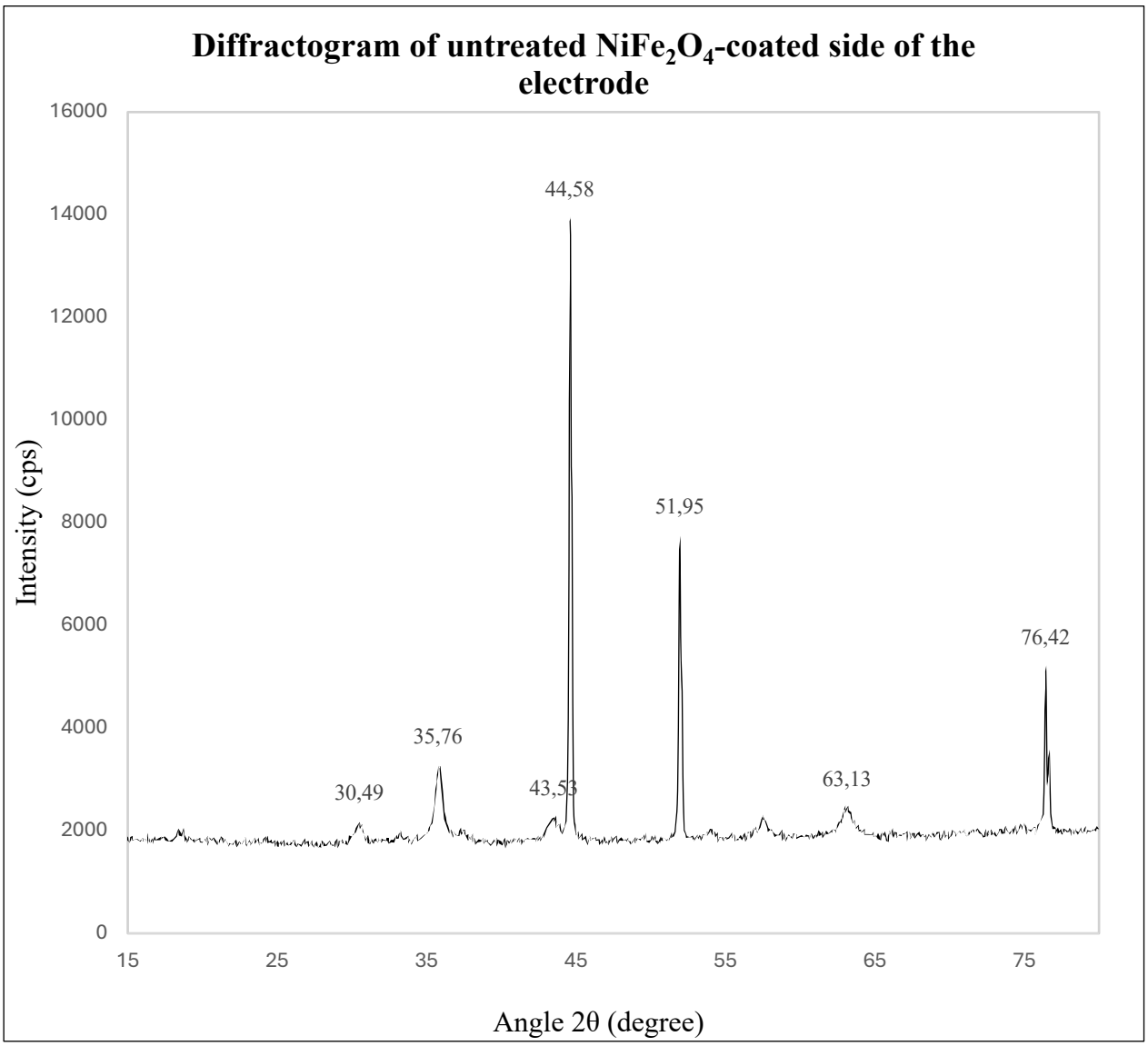

***Figure 48**: Diffractogram of untreated $NiFe_2O_4$-coated side of the electrode.*

Below there is a comparison between the peaks list of the sample and the reference standards for $NiFe_2O_4$ and metallic Ni.

Untreated $NiFe_2O_4$ electrode		**$NiFe_2O_4$ reference** 00-054-0964	**Ni reference** 00-001-1260
Intensity	Angle 2θ	Angle 2θ	Angle 2θ
2163	30.49°	30.31°	/
3264	35.76°	35.70°	/
2258	43.53°	43.38°	/
13930	**44.58°**	**/**	**44.60°**
7745	51.95°	/	51.91°
2439	63.13°	63.02°	/
5208	76.42°	/	76.81°

Table 17: *Predominant peaks of the untreated $NiFe_2O_4$-coated side of the electrode, compared with the reference pattern for $NiFe_2O_4$ and Ni.*

The diffractogram of the $NiFe_2O_4$-coated side of the electrode reveals that while some peaks align with the characteristic reference pattern of $NiFe_2O_4$ powder, others do not correspond to the expected structure, indicating the presence of additional phases in the material.

In particular, the most intense peak, observed at 44.58°, along with several others, aligns with characteristic peaks of metallic nickel, which can be attributed to the underlying nickel felt. The high intensity of these peaks can indicate the noticeable presence of nickel in the diffractogram.

The chart below provides a comparison of the diffractogram for the $NiFe_2O_4$ catalytic powder and the one for the $NiFe_2O_4$-coated side of the electrode in its untreated form.

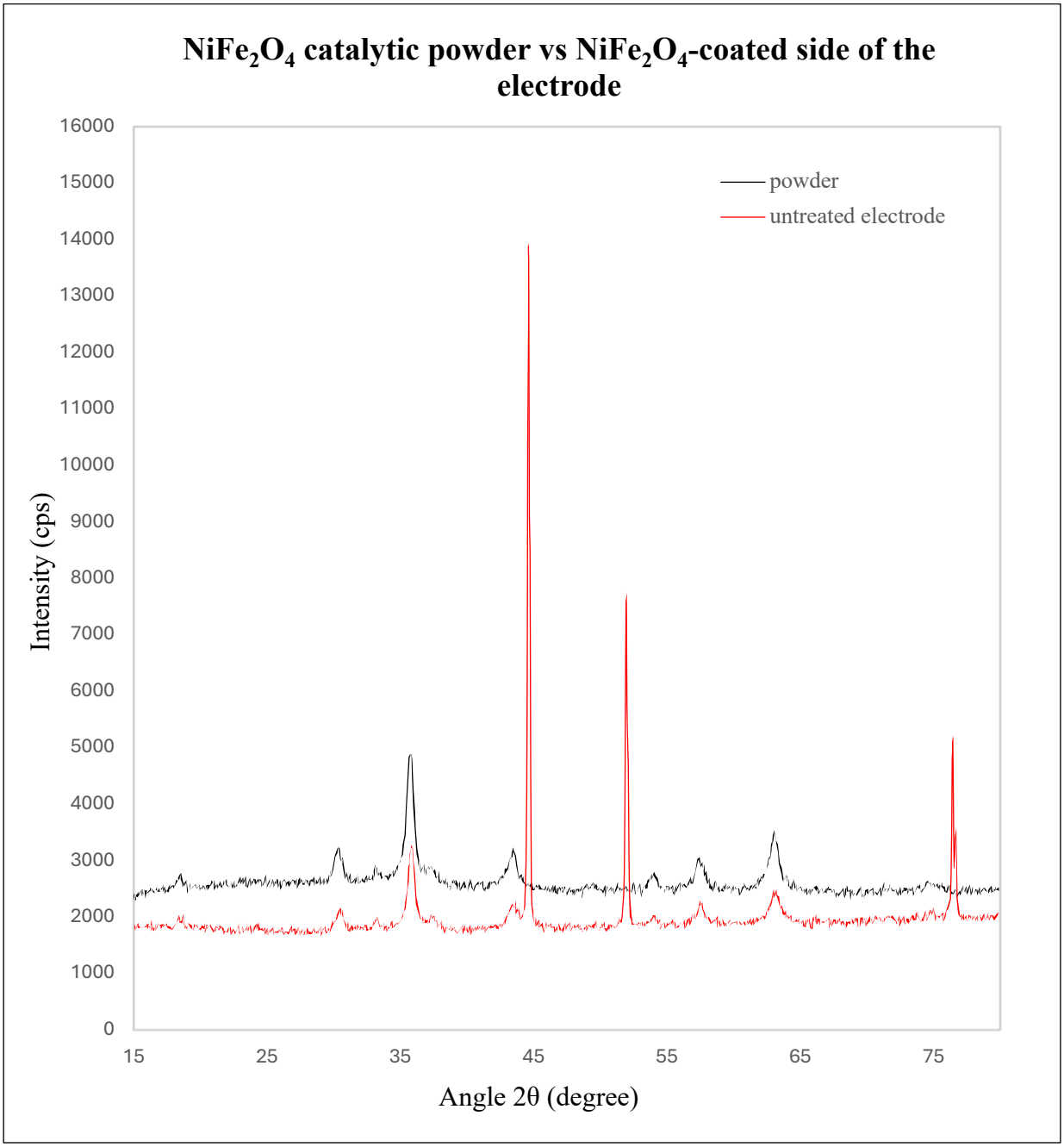

Figure 49: *Comparison of the diffractograms of the $NiFe_2O_4$ powder and the untreated $NiFe_2O_4$-coated side of the electrode.*

Both the diffractogram of the $NiFe_2O_4$ catalytic powder and the one of the $NiFe_2O_4$-coated side of the electrode show peaks that correspond to the characteristic peaks of the $NiFe_2O_4$ structure, confirming the successful deposition process and indicating that the catalytic ink was properly deposited and adhered to the electrode. The crystalline phase of the $NiFe_2O_4$ has been preserved

also after the deposition process, demonstrating that the method applied do not generates unwanted transformations.

However, as expected from the previous comparison between the $NiFe_2O_4$-coated side of the electrode and the reference patterns, certain peaks of the $NiFe_2O_4$-coated side of the electrode differ from those of the $NiFe_2O_4$ powder. These peaks are attributable to metallic nickel from the underlying nickel felt support; their high intensity indicates a significant presence of nickel atoms that can confirm the strong interaction between the catalytic layer and the support.

Arise from the peaks associated either to $NiFe_2O_4$ or metallic nickel, no other peaks have been detected, highlighting the absence of other phases contamination and confirming that the deposition process does not introduces impurities.

The slight shift of the two diffractograms likely derives from an instrumental limitation caused by the physical difference between the samples: the sample of the electrode is 3D, unlike the powder, which may have resulted in slight differences in sample height during the analysis.

These observations confirm the reliability of the deposition process, indicating that the catalytic ink was properly deposited and adhered to the electrode.

4.2.5. 350°C Thermally Treated $NiFe_2O_4$-Coated Side of the Electrode

The $NiFe_2O_4$-coated side of the electrode treated at 350°C was further analysed using XRD to investigate any structural changes induced by the thermal treatment.

The resulting diffractogram is showed below. The X-axis represents the diffraction angle 2θ in degrees, while the Y-axis indicates the intensity in counts per second (cps).

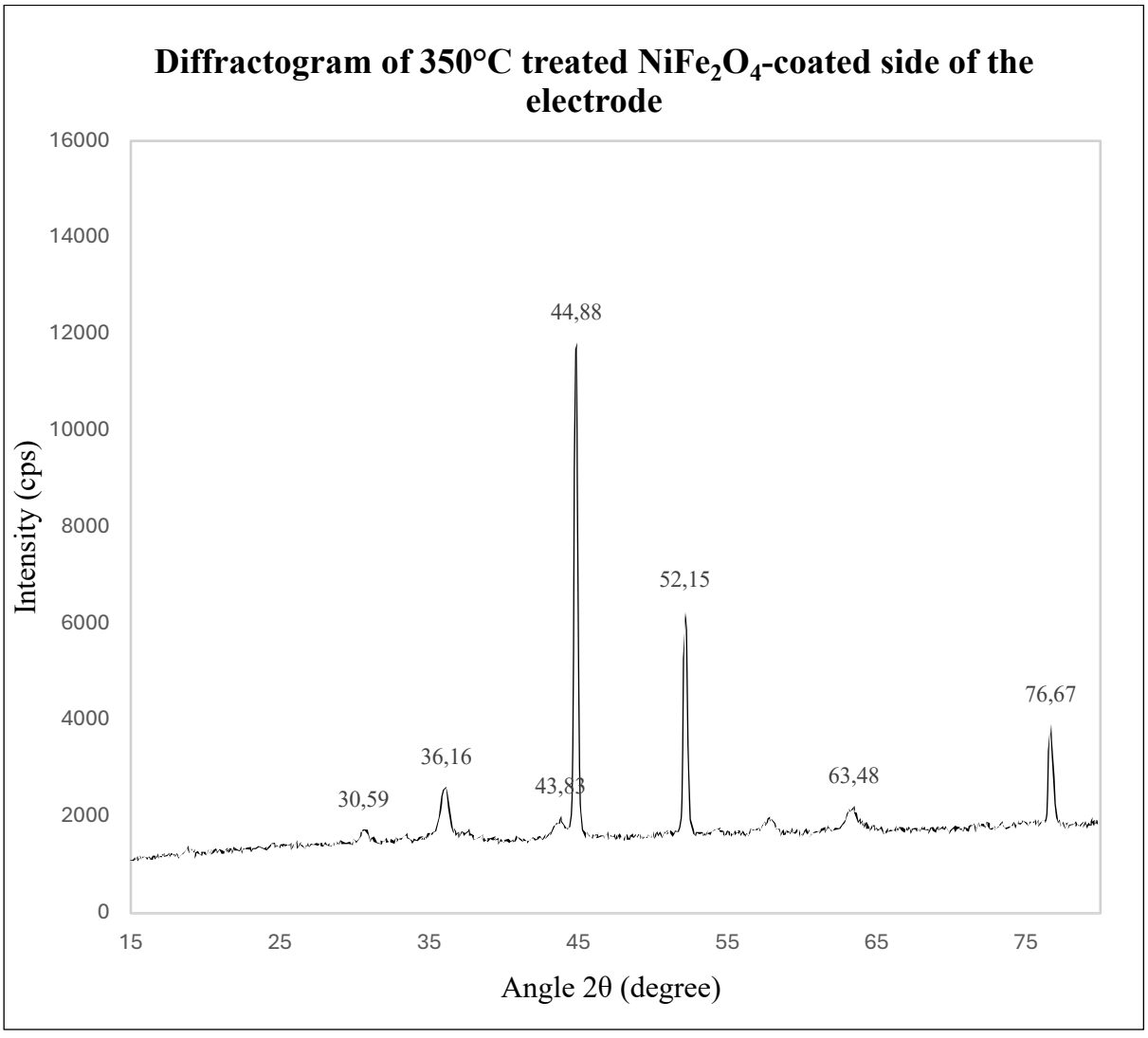

Figure 50: *Diffractogram of 350°C thermally treated $NiFe_2O_4$-coated side of the electrode.*

Below there is a comparison between the peaks list of the sample and the reference standards for $NiFe_2O_4$ and metallic Ni.

350°C-treated $NiFe_2O_4$ electrode		**$NiFe_2O_4$ reference** 00-054-0964	**Ni reference** 00-001-1260
Intensity	Angle 2θ	Angle 2θ	Angle 2θ
1734	30.59°	30.31°	/
2612	36.16°	35.70°	/
2014	43.83°	43.38°	/
11822	**44.88°**	/	**44.60°**
6287	52.15°	/	51.91°
2220	63.48°	63.02°	/
3910	76.67°	/	76.81°

Table 18: *Predominant peaks of 350°C thermally treated $NiFe_2O_4$-coated site of the electrode, compared with the reference pattern for $NiFe_2O_4$ and Ni.*

The peaks present in the 350°C thermally treated $NiFe_2O_4$-coated side of the electrode correspond to the reference patterns for $NiFe_2O_4$ and metallic Ni and are consistent with the peaks of the untreated electrode.

This result indicates that the thermal treatment has not influenced the phase composition.

Below is showed a comparison of the diffractograms of the of $NiFe_2O_4$-coated side of the electrode, untreated and treated at 350°C.

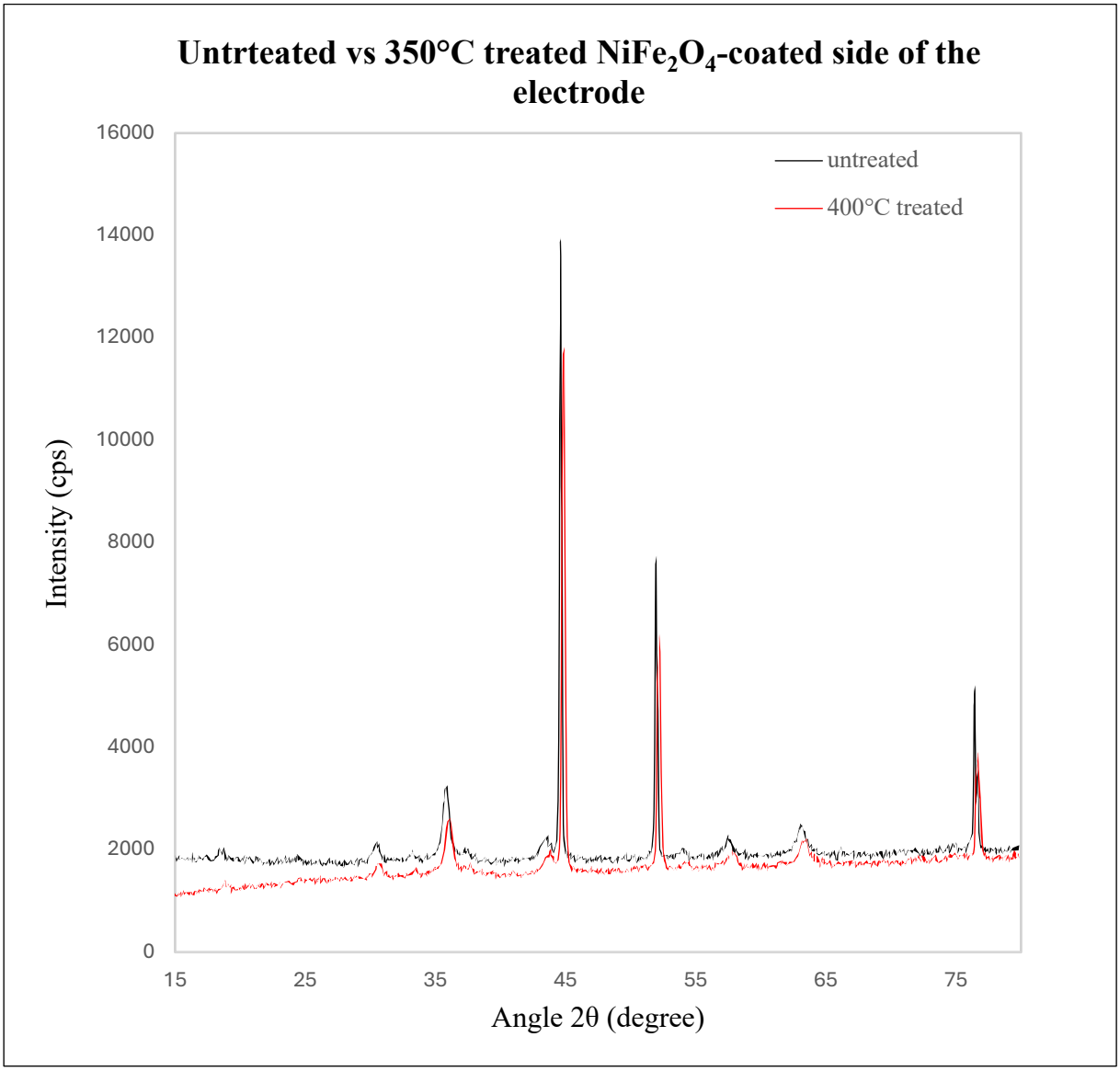

***Figure 51**: Comparison of the diffractograms of the untreated and 350°C-treated $NiFe_2O_4$-coated side of the electrode.*

The comparison between the diffractograms of the untreated and 350°C-treated $NiFe_2O_4$-coated side of the electrode reveals peaks in similar position: the crystalline phases present prior the heat treatment are preserved. The lack of other peaks indicates that the high temperature treatment does not introduce any undesirable phases.

A slight lateral shift in peak position is observed, which probably derives from an instrumental limitation: the three-dimensional nature of the samples may have resulted in slight variations in sample orientation during the analysis.

4.2.6. 120°C thermally treated $NiFe_2O_4$-Coated Side of the Electrode

The 120°C thermally treated $NiFe_2O_4$-coated side of the electrode was analysed with XRD to highlight any structural changes induced by the thermal treatment.

The resulting diffractogram is presented below. The X-axis represents the diffraction angle 2θ in degrees, while the Y-axis indicates the intensity in counts per second (cps).

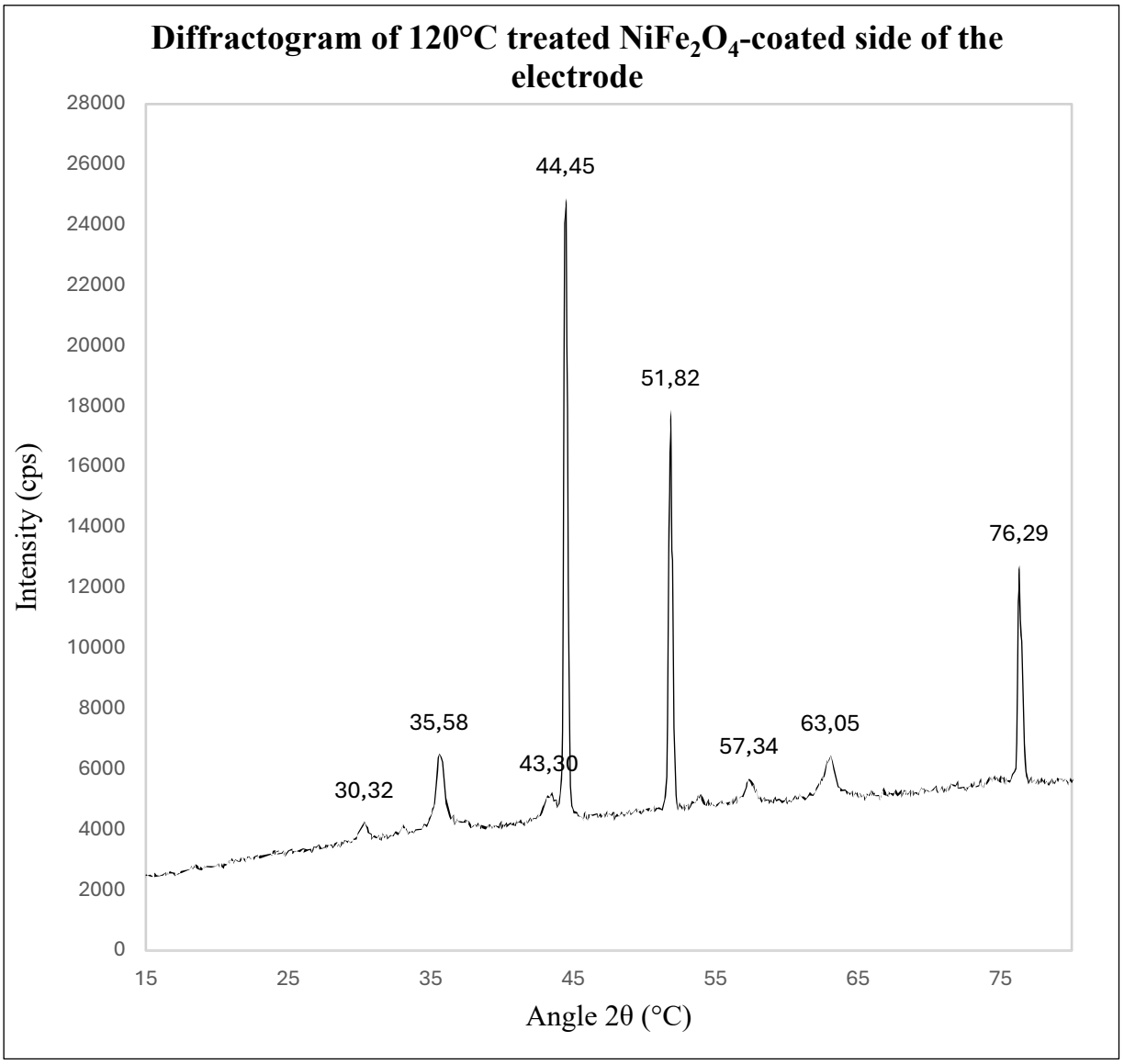

Figure 52: *Diffractogram of 120°C thermally treated $NiFe_2O_4$-coated side of the electrode.*

Below there is a comparison between the peaks list of the sample and the reference standards for $NiFe_2O_4$ and metallic Ni.

120°C-treated $NiFe_2O_4$ electrode		**$NiFe_2O_4$ reference** 00-054-0964	**Ni reference** 00-001-1260
Intensity	Angle 2θ	Angle 2θ	Angle 2θ
4266	30.32°	30.31°	/
6506	35.58°	35.70°	/
5143	43.30°	43.38°	/
24912	**44.45°**	/	**44.60°**
17901	51.82°	/	51.91°
5706	57.34°	57.40°	/
6459	63.05°	63.02°	/
12755	76.29°	/	76.81°

***Table 19**: Predominant peaks 120° treated $NiFe_2O_4$-coated side of the electrode, compared with the reference pattern for $NiFe_2O_4$ and Ni.*

The peaks positions of the 120°C thermally treated $NiFe_2O_4$-coated side of the electrode correspond to the reference patterns for $NiFe_2O_4$ and metallic Ni and are consistent with the peaks of the untreated electrode.

This result indicates that the thermal treatment has not influenced the phase composition.

Below is showed a comparison of the diffractograms of the of $NiFe_2O_4$-coated side of the electrode, in its untreated and treated at 120°C form.

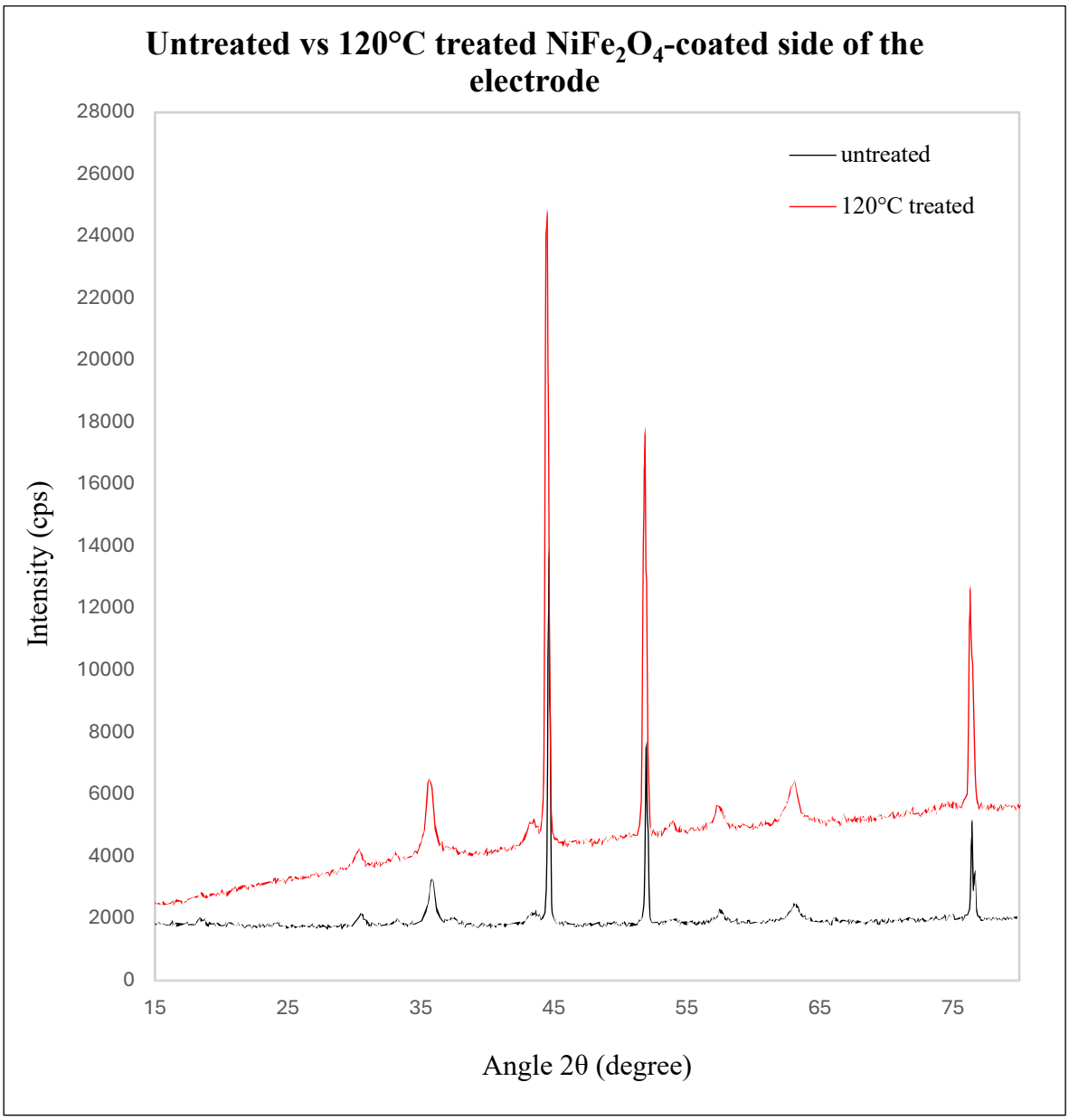

Figure 53: *Comparison of the diffractograms of the untreated and 120°C-treated $NiFe_2O_4$-coated side of the electrode.*

The comparison of the diffractograms of the untreated and 120°C thermally treated $NiFe_2O_4$-coated side of the electrode reveals that the peaks appear in similar positions: the phases present in the sample prior to the heat treatment are preserved after the thermal treatment.

Performance tests in an electrochemical cell are essential to evaluate the electrochemical behaviour and stability of the electrocatalyst under operative conditions. The results, including polarization curves, are presented in paragraph 5.1.

4.2.7. NiO-Coated Side of the Electrode

The 120°C thermally treated NiO-coated side of the electrode was analysed with XRD.

The resulting diffractogram is presented below. The X-axis represents the diffraction angle 2θ in degrees, while the Y-axis indicates the intensity in counts per second (cps).

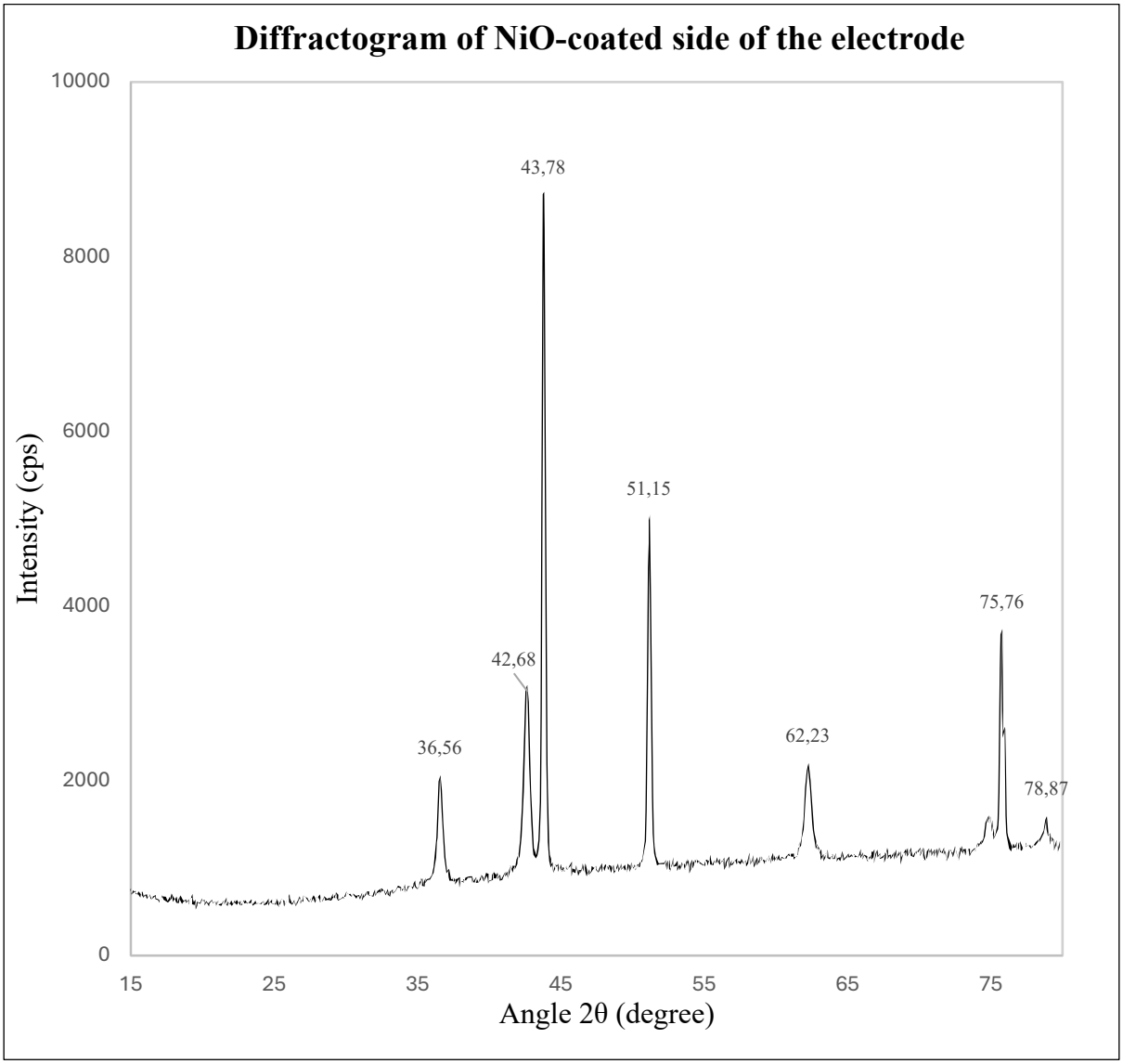

***Figure 54**: Diffractogram of NiO-coated side of the electrode.*

Below there is a comparison between the peaks list of the sample and the reference standards for NiO, $NiFe_2O_4$ and metallic Ni.

120°C-treated NiO electrode		**NiO reference** 01-071-1179	**$NiFe_2O_4$ reference** 00-054-0964	**Ni reference** 00-001-1260
Intensity	Angle 2θ	Angle 2θ	Angle 2θ	Angle 2θ
2063	36.56°	37.25°	/	/
3022	42.68°	43.28°	/	/
8714	**43.78°**	**/**	**/**	**44.60°**
5030	51.15°	/	**/**	51.91°
2204	62.23°	62.84°	/	/
3739	75.76°	/	75.79°	/
1593	78.87°	79.37°	/	/

***Table 20**: Predominant peaks 120° treated NiO-coated side of the electrode, compared with the reference pattern for NiO, $NiFe_2O_4$, Ni.*

The detected peaks are shifted by approximately one degree compared to the reference patterns, which is likely due to instrumental limitations caused by a non-ideal orientation of the sample, as the NiO layer is a three-dimensional structure rather than a powdered sample.

The analysis of the diffractogram of the NiO-coated side of the electrode indicates peaks that corresponds to a crystalline NiO structure.

However, the comparison with standard references highlights the presence of additional phases, suggesting multiple phases or potential contamination.

In particular, the predominant peak at 43.78° and another at 51.15° align with the reference standard for metallic nickel, attributable to the underlying nickel felt.

Furthermore, the peak at 75.76° corresponds to $NiFe_2O_4$, and could be attributed to residual contamination from $NiFe_2O_4$-coated electrode, as the NiO electrode was produced using the same plotter previously employed for the $NiFe_2O_4$ electrode.

4.2.8. Co_3O_4-Coated Side of the Electrode

The 120°C thermally treated Co_3O_4-coated side of the electrode was analysed with XRD.

The resulting diffractogram is presented below. The X-axis represents the diffraction angle 2θ in degrees, while the Y-axis indicates the intensity in counts per second (cps).

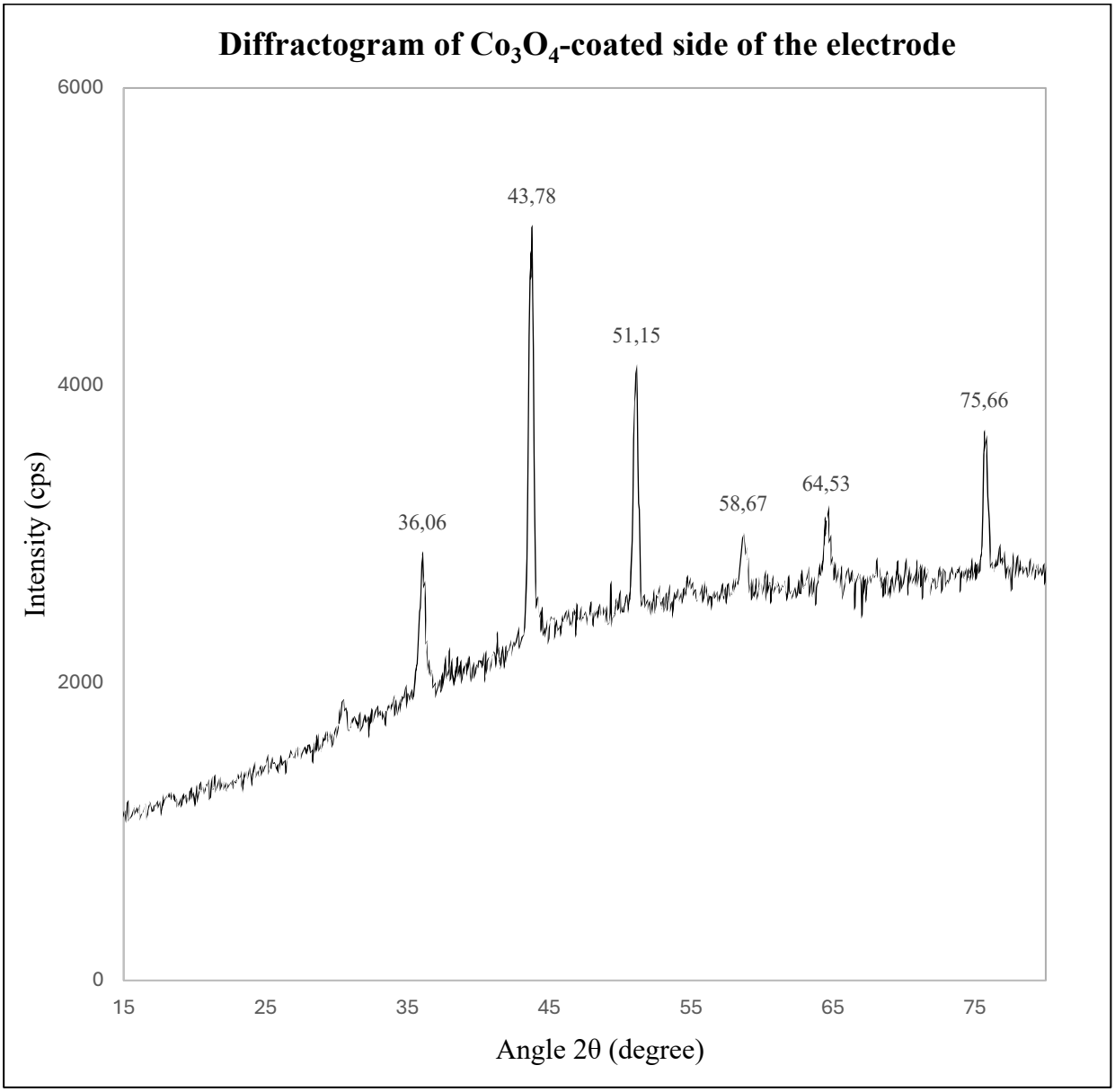

Figure 55: *Diffractogram of Co_3O_4-coated side of the electrode.*

Below there is a comparison between the peaks list of the sample and the reference standards for Co_3O_4, NiO, $NiFe_2O_4$ and metallic Ni.

120°C-treated Co_3O_4 electrode		**Co_3O_4 reference** 42-1467	**NiO reference** 01-071-1179	**$NiFe_2O_4$ reference** 00-054-0964	**Ni reference** 00-001-1260
Intensity	Angle 2θ	Angle 2θ	Angle 2θ	Angle 2θ	Angle 2θ
2887	36.06°	36.81°	/	/	/
5081	**43.78°**	**44.78°**	**/**	/	**44.60°**
4144	51.15°	**/**	**/**	**/**	51.91°
3013	58.67°	59.32°	**/**	**/**	/
3149	64.53°	65.23°	/	/	/
3704	75.66°	/	/	75.79°	/

***Table 21**: Predominant peaks 120° treated Co_3O_4-coated side of the electrode, compared with the reference pattern for Co_3O_4, $NiFe_2O_4$, NiO, Ni.*

Similarly to the NiO spectrum, most of the detected peaks are shifted by approximately one degree compared to the reference patterns, which is probably caused by a non-ideal orientation of the three-dimensional sample.

The analysis of the peaks in the diffractogram of the Co_3O_4-coated side of the electrode confirms the crystalline structure of Co_3O_4. It appears also a peak (51.15°) attributable to the underlying nickel felt. The peak at 43.78° could be attributed either to Co_3O_4 or to metallic nickel.

Additionally, there are insights of possible contamination from $NiFe_2O_4$ (75.66°), which may be caused by traces of this material as the deposition of Co_3O_4 has been performed using the same plotter, subsequently to the deposition of the other two catalysts.

4.3. Particles Size Calculations

Average particle dimensions were calculated for the $NiFe_2O_4$ powder and for the $NiFe_2O_4$-coated electrode in its untreated form, as well as after treatments at 350°C and 120°C, to assess the effect of thermal treatments on the average crystallite size.

Subsequently, the average crystallite dimensions of 120°C-treated NiO and Co_3O_4 electrodes were estimated and compared with 120°C-treated $NiFe_2O_4$ sample, to identify the catalyst with the smallest particle size and correlate the results with the electrochemical performances, discussed in paragraph 5.

The estimation of the average size of the crystallites has been performed using the Scherrer equation: [33]

$$D = \frac{K\lambda}{\beta \cos\theta}$$

Where:

- K is the shape factor or Scherrer constant, typically between 0.89 and 1, its value depends on the shape of the crystallites;
- λ is the wavelength of the X-ray radiation used, in this case Cu;
- β is the full width at half maximum (FWHM) of the diffraction peak, in radian;
- θ is the Bragg angle, half of the 2θ value at which the diffraction peak occurs.

The calculations were performed using Excel. The parameters listed below are common to all the calculations performed and are based on the specific characteristics of the XRD instrument utilized.

K	0.9
λ	1.541874
β instrument (°)	0.0869°

***Table 22**: Parameters used for calculations of average crystallite size.*

Below are presented the results of the calculations of the average particle size of the $NiFe_2O_4$ powder, as well as for the untreated and thermally treated electrodes.

	Powder	**Untreated electrode**	**350°C-treated electrode**	**120°C-treated electrode**
β (°)	1.62°	0.27°	0.50°	0.42°
2θ (°)	35.81°	44.58°	44.88°	44.45°
D (nm)	5.14 nm	32.05 nm	17.22 nm	20.69 nm

***Table 23**: Average crystallite size $NiFe_2O_4$ powder, untreated electrode, 120°C and 350°C treated electrode and parameters used for the calculations.*

As expected, the wider peaks observed in the diffractogram of $NiFe_2O_4$ powder, which indicate smaller particle dimensions compared to those of the electrodes, are consistent with calculations using the Scherrer equation, that confirm that the catalytic powder has the smallest average crystallite size.

Comparing the untreated and 350°C-treated $NiFe_2O_4$ electrode, the latter shows smaller crystallite dimensions, suggesting that the high temperature treatment promotes a better redistribution of particles, preventing the formation of large aggregates. This could be beneficial for the catalytic activity, as smaller particles determine a higher surface area, providing more active sites available for the reactions. However, SEM analysis (paragraph 4.1.5.) revealed cracks in the 350°C-treated electrode, that can compromise its mechanical integrity, potentially leading to catalyst detachment during the reactions.

Considering the lower temperature treatment (120°C), the particle sizes are reduced compared to the untreated electrode, but the crystallites remain slightly larger respect to those of the electrode treated at higher temperatures. Nonetheless, SEM analysis of the electrode treated at 120°C has not revealed signs of mechanical stress (paragraph 4.1.6.) differently from the 350°C threated electrode. Therefore, the lower temperature treatment can represent a compromise between reducing particle sizes and maintaining structural integrity.

To fully assess the impact of these treatments, it is crucial to evaluate the behaviour of the electrocatalysts under real operational conditions in the electrochemical cell. Polarization curves derived from experimental data are provided in paragraph 5.1., allowing a comprehensive interpretation that includes structural properties, electrochemical efficiency and durability.

Subsequently, crystallite dimensions of NiO and Co_3O_4 120°C-treated electrodes have been estimated, using X-ray diffraction and the Scherrer equation, and compared with $NiFe_2O_4$ 120°C-treated sample, in order to identify the catalyst with the smallest particle size, which could potentially exhibit the highest catalytic activity.

	$NiFe_2O_4$	**NiO**	**Co_3O_4**
β (°)	0.26808558°	0.49957798°	0.41508341°
2θ (°)	44.58063833°	43.77849746°	43.77849746°
D (nm)	20.69 nm	21.33 nm	10.03 nm

Table 24: *Average crystallite size for NiO, Co_3O_4, $NiFe_2O_4$ and parameters used for the calculations.*

These results indicate Co_3O_4 as the catalyst with the smallest crystallite size, which could potentially lead to the highest catalytic activity due to the greater availability of active sites.

However, evaluations in operative conditions have to be performed in order to assess the effective electrochemical behaviour, including stability over time. Polarization curves derived from experimental data are presented in paragraph 5.2.

5. Polarization Curves

Electrochemical tests have been performed using a single-cell configuration in an electrochemical AEMWE test station to evaluate and compare the performance of the anodic electrocatalysts.

Each anodic catalyst was tested individually, with each system including a Pt/C cathode. The tests were performed under controlled conditions, maintaining a constant current density of 0.6 A/cm^2 and a constant operating temperature of 60°C.

The cell was run continuously at 0.6 A/cm^2 for 40 hours, after which a polarization curve was recorded by increasing the potential and measuring the current, to assess the catalytic activity of the MEAs. Following this, the cell continued to operate under the same conditions and at 65 hours, another polarization curve was recorded to evaluate the stability and the performance over time.

5.1. Thermal Treatments Effect on $NiFe_2O_4$

By comparing the polarization curves of the $NiFe_2O_4$ catalyst treated at 350°C and l20°C after 40 and 65 hours of operation, it is possible to determine how the thermal treatments influence the performances.

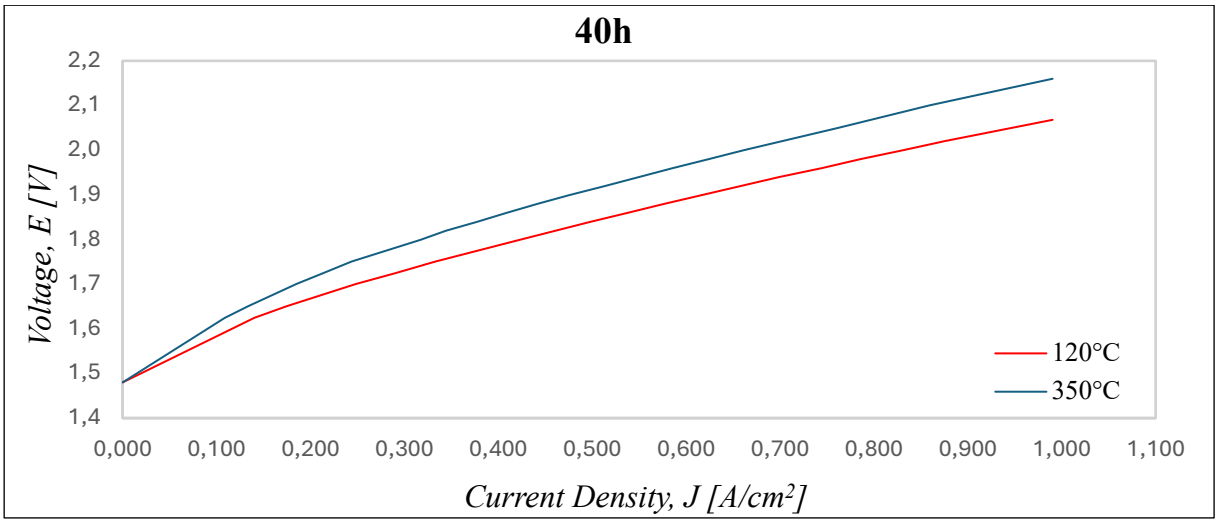

Figure 56: *Polarization curves of $NiFe_2O_4$-based MEA at 40h.*

Analysing the polarization curve recorded after 40 hours of operation, it appears that the catalyst treated at 350°C exhibits higher voltage values respect to the 120°C-treated sample, across the

entire range of current densities, suggesting that the higher temperature thermal treatment affects negatively the electrochemical efficiency. In fact, the possibility to obtain the same current density at lower voltages is an enhancement for electrolyzers operations and thus in these graphs the lower is the curve, the better are the performances.

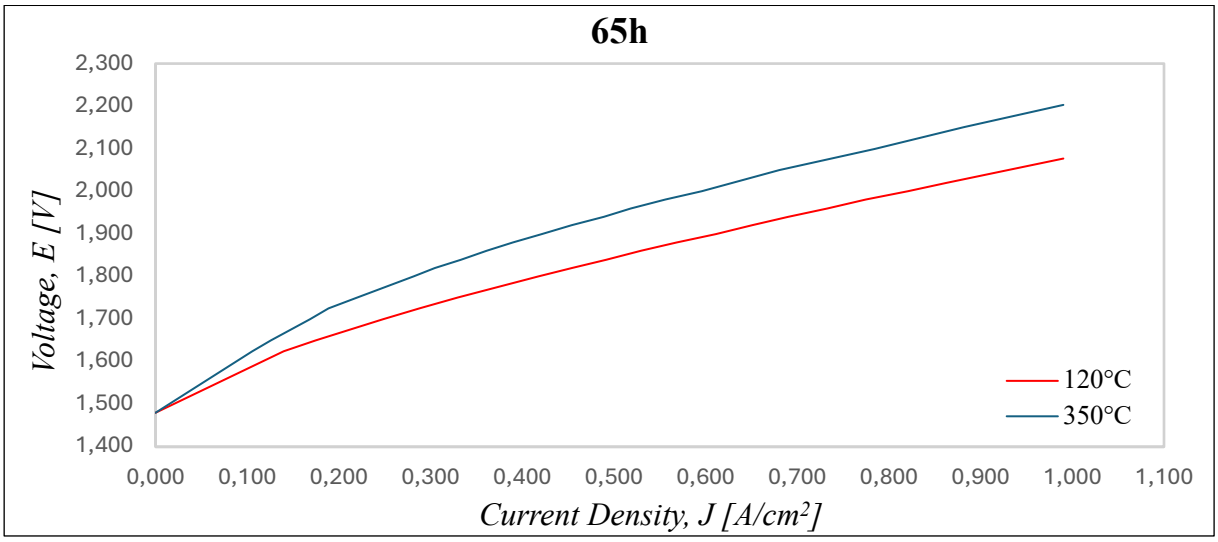

Figure 57: *Polarization curves of $NiFe_2O_4$-based MEA at 65h.*

After 65 hours, the difference between the two samples becomes even more pronounced. The decline in performance, already evident after a short period, highlights the reduced stability of the catalyst treated at higher temperatures.

By comparing the individual polarization curves of the $NiFe_2O_4$ treated at 120°C and 350°C after 40 and 65 hours of operation, the impact of thermal treatment on performances becomes even more evident.

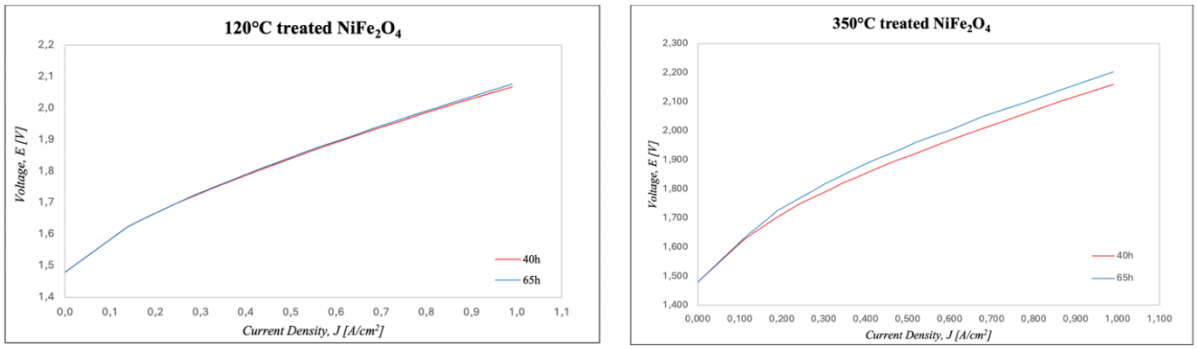

Figure 58*: Polarization curves for single for $NiFe_2O_4$ treated at 120°C after 40 and 65 hours of operation.*

The MEA that includes the catalyst treated at 120°C shows minimal variation between the curve registered at 40 and 65 hours, indicating high stability in time.

In contrast, the same MEA but with $NiFe_2O_4$ treated at 350°C, shows a noticeable shift between the two curves, especially at high current densities, further confirming its reduced stability.

The observed decline in performance and stability of the catalyst treated at 350°C could be associated with structural degradation including cracks formation, as previously suggested by observation of SEM analysis discussed in paragraph 4.1.5. These cracks may have caused detachment of the catalyst from the support during operating conditions, reducing the effective active surface area. Moreover, the electrical contact between the catalyst layer and the underlying nickel felt can be compromised by the fractures, resulting in an increase resistance.

These findings indicate the unsuitability of the 350°C thermal treatment to ensure appropriate performance and durability of the catalyst.

5.2. Comparison of Electrocatalysts Performance

The polarization curves of $NiFe_2O_4$, NiO and Co_3O_4 after 40 hours of operation have been compared and presented below.

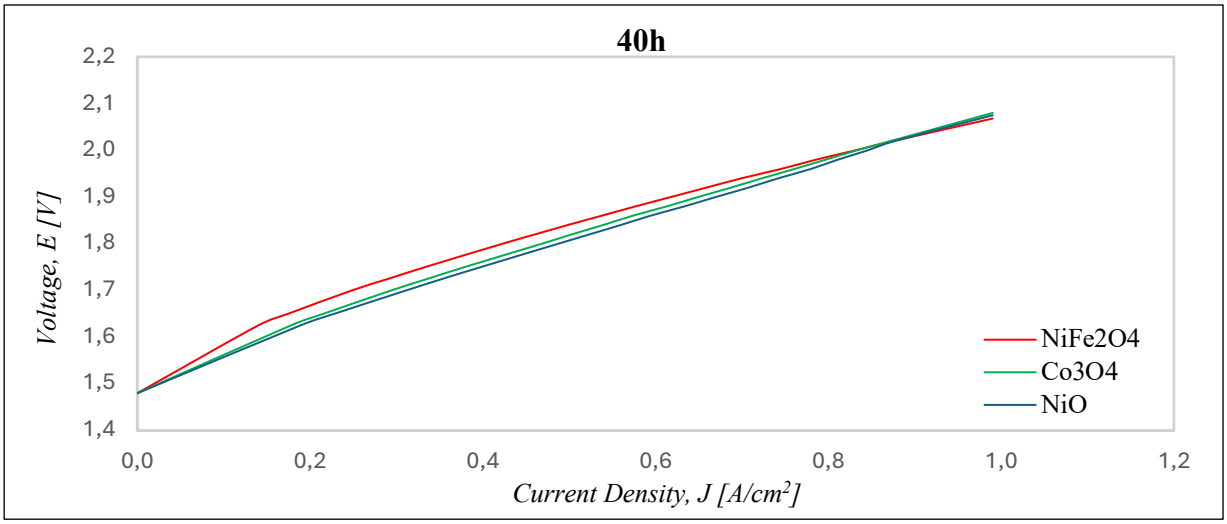

***Figure 59**: Polarization curves of $NiFe_2O_4$, Co_3O_4, NiO-based MEA at 40h.*

Comparing the polarization curves after 40 hours, NiO and Co_3O_4 show better performance, with lower potential values, compared to $NiFe_2O_4$, at low and intermediate current density ranges. In these current regions, the electrochemical behaviour is predominantly governed by the kinetics of the electrode reaction, followed by ohmic resistances. The specific characteristics of NiO and Co_3O_4 probably guarantee some advantages in these zones.

In the case of NiO, its simple structure may facilitate efficient charge transfers, contributing to its superior performance: indeed, it exhibits the lowest potential values at low and intermediate current densities.

Considering Co_3O_4, the coexistence of Co^{3+} and Co^{2+} ions can enhance electronic conductivity and facilitate electron transfer processes. Additionally, its smaller average particle size of 10.03 nm compared to the 20.69 nm of $NiFe_2O_4$ and 21.33 nm for NiO, can ensure a higher number of active sites, which results from an increased surface area, and guarantee high catalytic activity.

At high current densities, $NiFe_2O_4$ exhibits a better performance compared to NiO and Co_3O_4. In these current ranges, where kinetics mechanisms become more complicated, the synergy between Ni and Fe in $NiFe_2O_4$ catalyst becomes crucial and can increase the availability of catalytic sites.

The polarization curves of $NiFe_2O_4$, NiO and Co_3O_4 after 65 hours of operation have been compared and presented below.

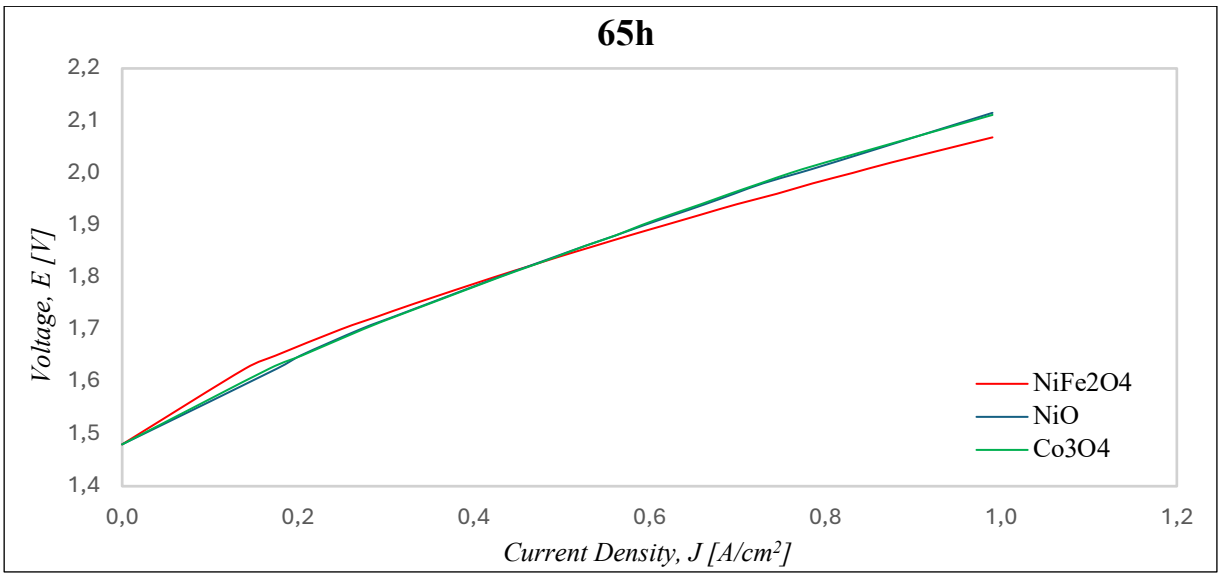

***Figure 60**: Polarization curves of $NiFe_2O_4$, Co_3O_4, NiO-based MEA at 65h.*

Notably, after only 65 hours, an interval that is not particularly long, the behaviour of $NiFe_2O_4$ catalyst begins to deviate further from the other two catalysts, exhibiting even greater catalytic activity at high current densities. This result indicates the superior stability of the $NiFe_2O_4$ catalyst respect to the NiO and the Co_3O_4.

5.2.1. Comparison of Electrocatalysts Stability

To evaluate the long-term durability of the catalysts and confirm the superior stability of $NiFe_2O_4$**,** the individual polarization curves of 120°C-treated $NiFe_2O_4$, NiO, Co_3O_4, after 40 and 65 hours of operations**.** Polarization curves are presented below.

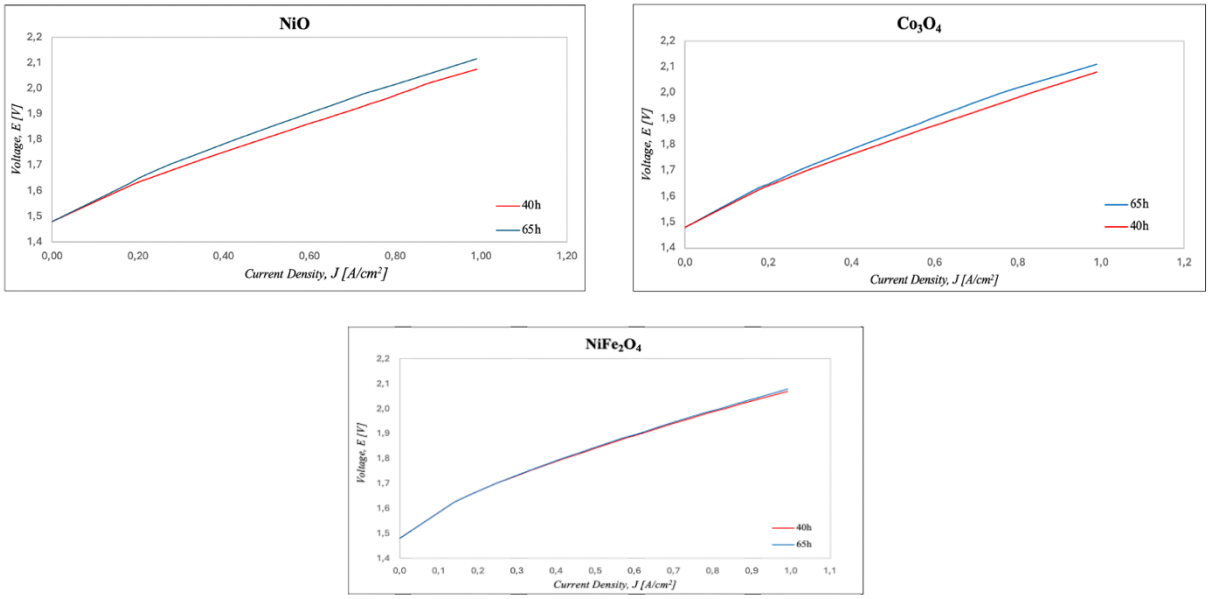

Figure 61*: Polarization curves single for catalysts treated at 120°C after 40 and 65 hours of operation.*

Considering the $NiFe_2O_4$-based MEA, curves at 40 and 65 hours overlap almost completely, indicating great stability over the testing period.

In contrast, both Co_3O_4 and NiO exhibit greater degrees of degradation over the same period, with Co_3O_4 showing a particular decline in performance at higher current densities. Despite CO_3O_4's smaller particles size (10.03 nm) guarantees higher catalytic activity, it may lead to sintering, a process that causes the aggregation of crystallites into larger structures under operating conditions, including elevated temperature and current density. The eventual formation of the aggregate can reduce the active surface area.

6. Conclusions

This thesis focused on the development and optimization of CCS anodic electrodes for Anion Exchange Membrane Electrolyzers. The main goal was to test different anodic catalysts, including NiO, Co_3O_4, and $NiFe_2O_4$, to determine which one could be the most suitable for industrial applications, identifying the catalyst that provides the best combination in terms of performance and durability.

By combining structural (XRD), morphological (SEM), and electrochemical performance analyses in single-cell tests, this study aimed to explore the relationship between material properties, catalytic activity, and stability, offering insights for enhancement of electrodes performance and durability.

Based on the results obtained from the electrochemical tests, $NiFe_2O_4$ appears to be the most suitable, particularly when considering long-term stability.

6.1. Thermal Treatments

Thermal treatments at 350°C and 120°C were performed on the $NiFe_2O_4$ electrodes to investigate the impacts of temperature on the performance and stability of the electrodes. The untreated electrode was compared with thermally treated ones, focusing on both the coated and uncoated sides.

SEM analysis, supported by EDS, indicated that the 350°C-treated electrode had a lower degree of impurities, highlighting that the high temperature treatment effectively removed some contaminations; however, it also resulted in the formation of cracks, compromising the structural integrity of the electrode. In particular, in the treated sample a depletion in iodine has been observed, attributable to ionomer decline, which can cause catalyst detachment from the substrate in operative conditions and impact the electrode's performance by reducing its ion conductivity.

In contrast, SEM analysis of the 120°C-treated electrode revealed neither visible cracks nor significant morphological changes respect to the untreated electrode. Traces of the ionomer have been indeed detected through EDS analysis. Notably, the untreated sample is already subjected to a temperature of 90°C during the deposition of the catalytic ink on the nickel felt support, which is not significantly lower compared to the 120°C treatment.

Calculations of the average particle size using the Scherrer equation revealed that the $NiFe_2O_4$ electrode treated at 350°C exhibits smaller crystallite dimensions compared to both the untreated and 120°C-treated samples, with values of 32.95 nm for the untreated sample, 17.22 nm for the 350°C-treated sample, and 20.69 nm for the 120°C-treated sample. This suggests that the higher temperature treatment promotes a better redistribution of particles, preventing the formation of large aggregates. The reduction in particle size is beneficial for the catalytic activity, since smaller particles result in a higher surface area, providing more active sites for electrochemical reactions. The lower temperature treatment (120°C) effectively reduced the particle size compared to the untreated sample but not to the extent achieved with the 350°C treatment. However, the 120°C treatment could represent a compromise between reducing particle size and maintaining structural integrity.

The structural changes in the 350°C-treated electrode were related to a reduction in performance, hypothesis which was confirmed by polarization curves, which revealed higher voltage values across all current densities compared to the 120°C-treated electrodes.

In conclusion, the lower-temperature treatment (120°C) better preserves the chemical-physical properties of the material, whereas the higher-temperature treatment (350°C), although it more effectively reduced particle size and eliminated impurities, also led to a decline in mechanical integrity, being unsuitable for applications requiring long-term durability, such as electrolyzers.

These findings highlight the importance of a proper balance of thermal treatment conditions to optimize catalytic efficiency, structural integrity and mechanical resistance.

6.2. Catalysts comparison

The comparison of the MEA including $NiFe_2O_4$, NiO, CO_3O_4 indicated difference in their catalytic activity and stability, which depend on the specific properties of the catalysts and the current density range.

Specifically, after 40 hours of operation, at low and intermediate current densities, NiO and CO_3O_4 demonstrated better performance, with low potential values. Considering CO_3O_4, its high catalytic activity could be related to its smaller particle size (10.03 nm) compared to $NiFe_2O_4$ (20.69 nm) and NiO (21.33 nm), along with the coexistence of Co^{3+} and Co^{2+} ions that could increase electronic conductivity. On the other hand, NiO's simple structure could improve charge transfer.

In contrast, at higher current densities, $NiFe_2O_4$ showed a better performance respect to the other two electrocatalysts. The synergy between Ni and Fe in the catalyst could result as an advantage in these current regions where reaction rates increase due to the higher current density, requiring a more efficient catalytic activity.

After 65 hours of operations, $NiFe_2O_4$ exhibited even greater catalytic activity at high current densities respect to the other two electrocatalysts. This result indicated the superior stability of the $NiFe_2O_4$ catalyst respect to the NiO and the Co_3O_4.

Moreover, to assess the stability and durability over time, single-catalyst polarization curves after 40 and 65 hours of operation were compared. $NiFe_2O_4$ showed better stability respect to the other two catalysts, with almost entirely overlapping curves. In contrast, both NiO and Co_3O_4 demonstrated to degrade significantly over time, with Co_3O_4 showing a noticeable reduction in performance at high current densities.

It is important to note that, while smaller particle dimension guarantee higher catalytic activity due to an increase exposure of active sites, it also results in a less stable system. Typically, smaller particles have more atoms are exposed to the surface, where they are less coordinated than those in the bulk. This makes the surface atoms possess more energy and the surface more reactive. To minimize this surface energy and achieve a more stable state, small particles tend to undergo sintering, a process in which crystallites aggregate into larger structures. Sintering could occur under operating conditions, such as elevated temperature and high current density, reducing the active surface area and the catalytic activity. These considerations could explain the performance decline observed for Co_3O_4. Furthermore, these investigations on the dimensions of crystallites highlights the importance to optimize their size to ensure both high catalytic activity and stability.

In summary, while NiO and Co_3O_4 initial performance is strong, especially at low current densities, suggesting higher intrinsic catalytic activity, their long-term stability is limited compared to $NiFe_2O_4$. The initial worst performance of $NiFe_2O_4$ catalyst at low current densities attributed to slow activation kinetics, can be due to the necessity of a pre-activation process of the complex structure, which involves chemical and structural reorganization of the surface, in which the active sites achieve an optimal configuration, enabling the catalyst to perform with its fully electrocatalytic potential for the oxygen evolution reaction. Hence, $NiFe_2O_4$ electrocatalyst combines good catalytic activity and excellent stability, being the most

promising PGM-free electrocatalyst among the analysed ones for long-term electrochemical applications.

References

[1] A. Raveendran, M. Chandran, and R. Dhanusuraman, “A comprehensive review on the electrochemical parameters and recent material development of electrochemical water splitting electrocatalysts,” Jan. 26, 2023, *Royal Society of Chemistry*. doi: 10.1039/d2ra07642j.

[2] European Parlament, “Emissioni di gas serra nell’UE per paese e settore: Infografica.”

[3] S. D. Ebbesen, S. H. Jensen, A. Hauch, and M. B. Mogensen, “High temperature electrolysis in alkaline cells, solid proton conducting cells, and solid oxide cells,” Nov. 12, 2014, *American Chemical Society*. doi: 10.1021/cr5000865.

[4] U.S. Department of Energy’s Office of Energy Efficiency and Renewable Energy (EERE), “Hydrogen Tools: Hydrogen compared with other fuels. Hydrogen: a safe and versatile fuel for today’s needs.”

[5] N. Du, C. Roy, R. Peach, M. Turnbull, S. Thiele, and C. Bock, “Anion-Exchange Membrane Water Electrolyzers,” Jul. 13, 2022, *American Chemical Society*. doi: 10.1021/acs.chemrev.1c00854.

[6] I. Vincent and D. Bessarabov, “Low cost hydrogen production by anion exchange membrane electrolysis: A review,” Jan. 01, 2018, *Elsevier Ltd*. doi: 10.1016/j.rser.2017.05.258.

[7] I. - International Energy Agency, “Global Hydrogen Review 2023,” 2023. [Online]. Available: www.iea.org

[8] M. Awad *et al.*, “A review of water electrolysis for green hydrogen generation considering PV/wind/hybrid/hydropower/geothermal/tidal and wave/biogas energy systems, economic analysis, and its application,” Jan. 01, 2024, *Elsevier B.V.* doi: 10.1016/j.aej.2023.12.032.

[9] R. Rocky Mountain Institute, “Clean Energy 101: The Colors of Hydrogen: Economics of Green, Blue, and Gray Hydrogen”.

[10] I. Vincent, E. C. Lee, and H. M. Kim, “Highly cost-effective platinum-free anion exchange membrane electrolysis for large scale energy storage and hydrogen production,” *RSC Adv*, vol. 10, no. 61, pp. 37429–37438, Oct. 2020, doi: 10.1039/d0ra07190k.

[11] M. A. Murmura, S. Cerbelli, S. Lo Conte, and M. C. Annesini, “Modelli per la simulazione e la progettazione di celle di elettrolisi a carbonati fusi operanti ad alta e media temperatura.”

[12] P. Millet, “2 Fundamentals of Water Electrolysis Thermodynamics of the Water Splitting Reaction 2.1.1 Thermodynamic Functions of State,” 2015.

[13] J. Yang *et al.*, “Non-precious electrocatalysts for oxygen evolution reaction in anion exchange membrane water electrolysis: A mini review,” Oct. 01, 2021, *Elsevier Inc.* doi: 10.1016/j.elecom.2021.107118.

[14] S. Niroula, C. Chaudhary, A. Subedi, and B. S. Thapa, “Parametric Modelling and Optimization of Alkaline Electrolyzer for the Production of Green Hydrogen,” *IOP Conf Ser Mater Sci Eng*, vol. 1279, no. 1, p. 012005, Mar. 2023, doi: 10.1088/1757-899x/1279/1/012005.

[15] E. Esposito, A. Minotti, E. Fontananova, M. Longo, J. C. Jansen, and A. Figoli, “Green H2 Production by Water Electrolysis Using Cation Exchange Membrane: Insights on Activation and Ohmic Polarization Phenomena,” *Membranes (Basel)*, vol. 12, no. 1, Jan. 2022, doi: 10.3390/membranes12010015.

[16] H. A. Miller *et al.*, “Green hydrogen from anion exchange membrane water electrolysis: A review of recent developments in critical materials and operating conditions,” May 01, 2020, *Royal Society of Chemistry*. doi: 10.1039/c9se01240k.

[17] A. Khataee, A. Shirole, P. Jannasch, A. Krüger, and A. Cornell, “Anion exchange membrane water electrolysis using Aemion™ membranes and nickel electrodes,” *J Mater Chem A Mater*, vol. 10, no. 30, pp. 16061–16070, Jul. 2022, doi: 10.1039/d2ta03291k.
[18] L. An, T. S. Zhao, Z. H. Chai, P. Tan, and L. Zeng, “Mathematical modeling of an anion-exchange membrane water electrolyzer for hydrogen production,” *Int J Hydrogen Energy*, vol. 39, no. 35, pp. 19869–19876, Dec. 2014, doi: 10.1016/j.ijhydene.2014.10.025.
[19] J. Brauns and T. Turek, “Alkaline water electrolysis powered by renewable energy: A review,” Feb. 01, 2020, *MDPI AG*. doi: 10.3390/pr8020248.
[20] H. Ito *et al.*, “Investigations on electrode configurations for anion exchange membrane electrolysis,” *J Appl Electrochem*, vol. 48, no. 3, pp. 305–316, Mar. 2018, doi: 10.1007/s10800-018-1159-5.
[21] M. N. I. Salehmin, T. Husaini, J. Goh, and A. B. Sulong, “High-pressure PEM water electrolyser: A review on challenges and mitigation strategies towards green and low-cost hydrogen production,” Sep. 15, 2022, *Elsevier Ltd*. doi: 10.1016/j.enconman.2022.115985.
[22] Kevin Rouwenhorst, “Technology Status: Anion Exchange Membrane (AEM) Electrolysis.”
[23] A. W. Tricker, J. K. Lee, J. R. Shin, N. Danilovic, A. Z. Weber, and X. Peng, “Design and operating principles for high-performing anion exchange membrane water electrolyzers,” *J Power Sources*, vol. 567, May 2023, doi: 10.1016/j.jpowsour.2023.232967.
[24] S. Wang, A. Lu, and C. J. Zhong, “Hydrogen production from water electrolysis: role of catalysts,” Dec. 01, 2021, *Korea Nano Technology Research Society*. doi: 10.1186/s40580-021-00254-x.
[25] E. K. Volk, S. Kwon, and S. M. Alia, “Catalytic Activity and Stability of Non-Platinum Group Metal Oxides for the Oxygen Evolution Reaction in Anion Exchange Membrane Electrolyzers,” *J Electrochem Soc*, vol. 170, no. 6, p. 064506, Jun. 2023, doi: 10.1149/1945-7111/acd605.
[26] M. Li *et al.*, “Facile synthesis of electrospun MFe2O4 (M = Co, Ni, Cu, Mn) spinel nanofibers with excellent electrocatalytic properties for oxygen evolution and hydrogen peroxide reduction,” *Nanoscale*, vol. 7, no. 19, pp. 8920–8930, May 2015, doi: 10.1039/c4nr07243j.
[27] A. R. Paulraj, Y. Kiros, M. Göthelid, and M. B. Johansson, “NiFeOx as a bifunctional electrocatalyst for oxygen reduction (OR) and evolution (OE) reaction in alkaline media,” *Catalysts*, vol. 8, no. 8, Aug. 2018, doi: 10.3390/catal8080328.
[28] M. Bonomo, “Synthesis and characterization of NiO nanostructures: a review,” Aug. 01, 2018, *Springer Netherlands*. doi: 10.1007/s11051-018-4327-y.
[29] X. Tian, X. F. Lu, B. Y. Xia, and X. W. (David) Lou, “Advanced Electrocatalysts for the Oxygen Reduction Reaction in Energy Conversion Technologies,” Jan. 15, 2020, *Cell Press*. doi: 10.1016/j.joule.2019.12.014.
[30] X. Zhang *et al.*, “Recent advances in Pt-based electrocatalysts for PEMFCs,” Apr. 16, 2021, *Royal Society of Chemistry*. doi: 10.1039/d0ra05468b.
[31] T. B. Ferriday, P. H. Middleton, M. L. Kolhe, and J. Van Herle, “Raising the temperature on electrodes for anion exchange membrane electrolysis - activity and stability aspects,” *Chemical Engineering Journal Advances*, vol. 16, Nov. 2023, doi: 10.1016/j.ceja.2023.100525.
[32] A. Mohammed and A. Abdullah, “SCANNING ELECTRON MICROSCOPY (SEM): A REVIEW.”

[33] S. B. Gopale, G. N. Kakade, G. D. Kulkarni, V. Vinayak, S. P. Jadhav, and K. M. Jadhav, “X-ray diffraction, infrared and magnetic studies of NiFe2O4 nanoparticles,” in *Journal of Physics: Conference Series*, IOP Publishing Ltd, Oct. 2020. doi: 10.1088/1742-6596/1644/1/012010.